Spring 2021

Surveilling the Distinctive Vascular and Metabolic Features of Tumor Progression and Response to Therapy

John James Walsh
Yale University Graduate School of Arts and Sciences, jjw06d@gmail.com

Recommended Citation
Walsh, John James, "Surveilling the Distinctive Vascular and Metabolic Features of Tumor Progression and Response to Therapy" (2021). *Yale Graduate School of Arts and Sciences Dissertations*. 260.
https://elischolar.library.yale.edu/gsas_dissertations/260

Abstract

Surveilling the Distinctive Vascular and Metabolic Features of Tumor Progression and Response to Therapy

John James Walsh

2021

Glioblastoma (GBM) is the most common malignant primary brain tumor in adults. Despite maximal treatment with surgical resection, radiotherapy and temozolomide chemotherapy, prognosis is dismal with median survival around 15 months. GBMs are highly infiltrative tumors that invade into surrounding brain tissue, which makes defining the extent of tumor spread difficult and recurrence common. Radiological identification of GBMs with magnetic resonance imaging (MRI), using transvers (T_2) or longitudinal (T_1) relaxation contrasts, is a mainstay in the initial diagnosis as well as tracking therapeutic response in GBM. However, there is extreme variability in the structural appearance, size, metabolism, and genetic landscape of GBMs, making imaging characteristics highly heterogeneous and hard to define with tumor progression. Although T_2-weighted and contrast-enhanced T_1-weighted MRI provides anatomical details of the tumor architecture, these methods can be confounded by pseudoprogression and pseudoresponse in the context of therapy.

The GBM microenvironment is characterized by immature vasculature and extracellular acidification due to a metabolic shift towards aerobic glycolysis (Warburg effect). The reduced extracellular pH (pH_e) has been associated with promoting angiogenesis and invasion as well as creating an immunosuppressive environment. Given the important contribution of vascular changes and extracellular acidosis to shaping the tumor

microenvironment, advanced MRI techniques are needed to better characterize the tumor microenvironment to provide more specific readouts of tumor progression and therapeutic response.

Biosensor Imaging of Redundant Deviation in Shifts (BIRDS) is a magnetic resonance spectroscopic imaging (MRSI) technique that utilizes the temperature and pH-dependent hyperfine shifts of paramagnetic agents (e.g., $TmDOTP^{5-}$) for high resolution, three-dimensional, quantitative temperature and pH_e mapping. BIRDS has been used to demonstrate the acidic pH in preclinical models of GBM, where the intratumoral space is highly acidified ($pH<6.8$) in comparison to healthy brain tissue ($pH\sim7.2$) and acidic pH spread beyond the anatomically defined tumor core relates to the invasiveness of the tumors. However, a limitation of the BIRDS technique is the necessity of detectable (>1 mM) levels of contrast agent, which are cleared rapidly by the kidney. To obviate need for surgical intervention (e.g., renal ligation) to stop rapid agent clearance, here we demonstrate that pharmacological inhibition of renal clearance of these agents using probenecid allows for longitudinal imaging of pH_e throughout tumor progression and show that acidosis develops early in tumor progression in human-derived GBM tumors (U87 and U251).

Since other tomographic pH_e mapping methods are non-quantitative and directly altering pH_e in a specific tissue is difficult to implement, we looked to assess the ability of BIRDS-based temperature measurements to evaluate a localized cooling system that induces hypothermia in sheep brain to levels suggested to be neuroprotective in hypoxic states. Quantitative temperature mapping using BIRDS showed significantly decreased cerebral temperatures with cooling over all defined brain regions and was in agreement with thermocouple measurements.

While pH_e is a useful metric, tumor vascularity also shapes tumor metabolism and the microenvironment. BIRDS can be combined with other imaging modalities such as dynamic contrast enhanced (DCE) MRI, which allows quantification of vascular parameters (e.g., permeability) through modeling the dynamic uptake of Gd^{3+}-based contrast agents. Multiparametric characterization of the spatiotemporal changes in cellularity, vascularity and acidosis of U87 and U251 tumors throughout progression showed unique patterns that could be used to identify tumor features and differentiate between tumor types.

Finally, pH_e readouts have potential as a biomarker of therapeutic response. After finding an increase in pH_e after treatment with temozolomide in U251 tumors, we used BIRDS longitudinally to demonstrate normalization of pH_e in U87 tumors treated with sorafenib, a nonselective tyrosine kinase inhibitor. Both treatments slowed tumor progression and led to increases of pH_e which establishes a role for pH_e imaging as an early and sensitive marker of evaluating therapeutic response prior to observable changes in the tumor appearance on standard MRI.

The potential of BIRDS is vast and not limited to GBM, or cancer in general. Additional work has demonstrated that an acidic pH_e is not limited to preclinical tumor models, but is also found in patient-derived xenograft (PDX) models of metastatic melanoma in the brain. BIRDS can also be utilized in evaluating tumors in any organ, as BIRDS has also shown acidic pH_e in models of liver cancer. In summary, this work further expands BIRDS into a broadly applicable longitudinal platform for characterization of the tumor microenvironment and may aid in evaluation of many targeted therapeutic strategies.

Surveilling the Distinctive Vascular and Metabolic Features of Tumor Progression and Response to Therapy

A Dissertation
Presented to the Faculty of the Graduate School
of
Yale University
in Candidacy for the Degree of
Doctor of Philosophy

by
John James Walsh

Dissertation Director: D.S. Fahmeed Hyder

June 2021

Table of Contents

List of Figures

List of Tables

Acknowledgements

This dissertation would not have been possible without the support of many as well as the resources of Yale University and Yale School of Medicine. Thank you for taking a chance on me and offering me admission to the MD-PhD program. For that, I will always be grateful.

I would first like to especially thank my advisor and mentor, Dr. Fahmeed Hyder, who provided me with a wonderful lab experience during my time at Yale. Ever since he first gave me a tour of the Magnetic Resonance Research Center during my interview visit, I knew that this is the type of work that I wanted to pursue. After he gave me the opportunity to perform a rotation in his lab in summer 2014, I knew that his knowledge and enthusiasm would encourage and motivate me to become a better researcher. He has graciously given me so much time over the past 5 years to help me think through experimental plans and research questions, teach me about all aspects of running a lab, and encourage me to pursue my interests through collaborations. Thank you for an incredible experience.

I would also like to extend special thanks to my committee members: Dr. Daniel Coman, Dr. Douglas Rothman, Dr. Rick Bucala, and Dr. Fred Gorelick. Thank you all for your input, discussions, insights, and support throughout my graduate training. Your contributions have improved and shaped the direction of this dissertation and projects yet to come. Doug and Rick provided insightful discussions and different perspectives that could be incorporated into many aspects of my work. I would also like to thank Fred for his role in mentoring and supporting me from the perspective of the MD-PhD program and all his help in guiding me through the end of the PhD. I would also like to thank all the members of the committee for their support throughout fellowship applications, editing papers and presentations, and their guidance and direction in completing this dissertation. I would also like to especially thank Daniel for all of his valuable guidance and immeasurable help throughout all of my experiments. He was always willing to help me troubleshoot problems, talk through experimental plans, and have great discussions about science and engineering in general. He helped me set up many of the imaging sequences and provided so much assistance as we worked through many of the hardware problems that kept arising throughout my experiments. I would also like to thank him for always including me in many imaging experiments and different projects, it was this exposure that helped me learn and really helped me grow as an experimentalist.

I would like to thank the members of my lab group for all of their support and help along the way. Especially I would like to thank Yuegao (Golden) Huang and Jyotsna Rao who took me in when I first joined the lab and taught me everything I know about the animal models and lab techniques that were used throughout this dissertation. Golden introduced me to MRI/MRS experiments as well as some of the chemical synthesis. Jyotsna taught me about histology and helped guide me through some of the initial tumor treatment studies.

I am also extremely grateful for the help of Maxime Parent who guided much of the work on the DCE experiments and Adil Akif who provided much computational assistance in analyzing the data. I would also like to thank Muhammad Khan, Lucas Adam, Sandeep Mishra for all of their assistance with the animal experiments. I would also like to thank Peter Herman and Basavaraji Sanganahali for their support and insightful discussions as well as Jelena Mihailovic, ABM Zakaria, and Simon Sangaard for all your support in the lab. I really enjoyed all the time that we were able to spend together.

I would like to acknowledge many others with whom I worked at the Magnetic Resonance Research Center including Lesley Nadeau-Foti, Tara Marro, Meko Owens-Ward, Scott McIntyre, Peter Brown, Terry Nixon, Henk De Feyter, and Xiaoxian Ma. Also, a huge thank you to Bei Wang for all of her assistance with the animal surgeries.

I would also like to thank my many collaborators who got me involved in a variety of different projects, many of which are shown throughout this dissertation. You all have helped show me just how much this work can grow. The rabbit experiments were headed by Lynn Savic and Julius Chapiro, along with much help from Luzie Domel and Tabea Borde. The metastatic melanoma work was performed in collaboration with Thuy Tran and Harriett Kluger, thank you for giving us the ability to try our methods in a new model system. The hypothermia work in sheep was with John Simmons, John Elefteriades, and James Goodrich. I also had the privilege of learning some functional MRI from Jens Gottler and Stephan Kaczmarz.

I would like to acknowledge those in the Department of Biomedical Engineering including Cara Gibilisco and Richard Carson for all their help in navigating the graduate school process. I would also like to acknowledge the MD-PHD program including Barbara Kazmierczak, Jim Jamieson, Fred Gorelick, Cheryl DeFillippo, Sue Sansone, Reiko Fitzsimonds, and Alex Mauzerall. Thank you for all you do for this program, I am truly grateful. I also would like to acknowledge the funding source for the Yale MSTP (T32 GM-007205).

A special thanks to my MD-PhD classmates: Minh, Irina, Alanna, Swetha, Amanda, George, Don, William, Erin, Shivani. Thank you for your friendship and all the experiences we had together. What an amazing time it has been going through this process with you all.

To the many others who have been a part of my life in New Haven, thank you for making New Haven feel like home.

Finally, I would like to thank my family without whom I would not be where I am today. To my parents, you instilled in me the drive to chase my dreams and have supported me at every step along the way. I am so appreciative for your love and support and all that you have done for me. To my brothers, thank you for all the good times and always looking out for me. I am grateful for all the time I get to spend with you. To my partner, Edwin, thank you for sharing your life with me. I am always in awe of your knowledge and dedication to the things you love. I appreciate all the support you provide to me as well as you just being willing to listen when things were tough. I am lucky and fortunate to be able to share in all of life's experiences with you.

Chapter 1: Introduction to the Vascular and Metabolic Features of the Tumor Microenvironment in Glioblastoma

1.1 Abstract

Glioblastoma (GBM) is the most common primary malignant brain tumor in adults. GBMs exhibit unique genetic and metabolic alterations, as well as a characteristic tumor microenvironment that is shaped by the properties of surrounding brain tissue. Like other solid tumors, GBMs exhibit several of the hallmarks of cancer including altered cellular metabolism and disorganized vasculature. Hypoxia, as well as metabolic dysregulation, promotes a switch to glycolysis even in the presence of oxygen, termed aerobic glycolysis or the Warburg effect. Upregulated glycolysis results in extracellular acidosis, where the pH of the extracellular space (pH_e) becomes significantly lower than that found in normal tissues. Further, acidosis is not only linked to tumor growth, but may be regulated independently to promote more invasive and metastatic tumors. Extracellular acidosis results in remodeling of the extracellular matrix and shaping the tumor microenvironment as well as impacting both angiogenesis, the development of new vasculature in the tumor, and the tumor immune response. In this chapter, the role of metabolic and vascular changes in shaping the tumor microenvironment will be explored, with a particular focus in the context of glioblastoma (GBM).

1.2 Introduction

Cancer is the second leading cause of death in the United States. Glioblastoma (GBM) is the most common primary central nervous system (CNS) tumor in adults with approximately 10,000 new cases each year in the United States.[1] GBMs exhibit characteristic genetic and metabolic alterations and, like other solid tumors, maintain a tumor microenvironment that favors proliferation and invasion into surrounding tissue. Many connections between tumor metabolism and the microenvironment have been explored, including how genetic changes in cellular metabolism impact the local vasculature and microenvironment.

Alterations in cellular metabolism are a hallmark of cancer.[2] This dysregulation promotes a switch to glycolysis even in the presence of oxygen, termed aerobic glycolysis by Otto Warburg or otherwise known as the Warburg effect.[3] However, a clear link also exists between hypoxia and acidosis. With this switch comes an overproduction of lactate and protons that first accumulate in the intracellular compartment and are then extruded from the cell into the extracellular space, resulting in extracellular acidosis (**Figure 1.1**). To accomplish this, cells upregulate many transporters including the proton-sodium exchanger (NHE1) as well as monocarboxylate transporters (MCT4) to transport lactate out of the cell.[4] The pH of the extracellular space becomes significantly lower than that found in normal tissues. Further, acidosis may be regulated independently to promote more invasive and metastatic cancers as well as driving tumor growth.[5,6] Extracellular acidosis results in remodeling of the extracellular matrix and shaping the tumor microenvironment as well as impacting both angiogenesis, the development of new vasculature in the tumor, and the tumor immune response.[7,8] Before discussing the metabolic and vascular changes that occur in solid tumors, a brief introduction to GBM is presented along with rodent models that can be used as representative GBM models in preclinical work.

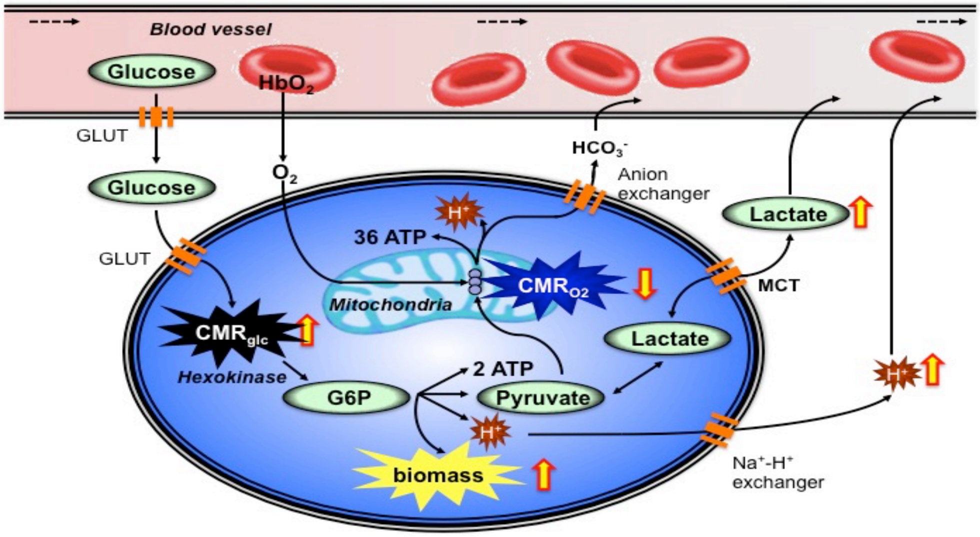

Figure 1.1. Tumor cell metabolism. Blood delivers both glucose and oxygen to the cell. Glucose is taken up by glucose transporters (GLUTs). Glucose then enters the glycolytic pathway where it is converted to pyruvate. Pyruvate is then either converted to lactate or enters the oxidative phosphorylation pathway. The ratio in the rate of glycolytic metabolism (CMR_{glc}) to the rate of oxidative phosphorylation (CMR_{O2}) is altered in tumor cells. To prevent acidification of the intracellular environment, lactate is extruded from the cell through monocarboxylate transporters (MCT) and protons through the sodium-proton exchanger (Na^+-H^+ exchanger). Adapted with permission.[9]

1.3 Glioblastoma

Glioblastomas are the most prevalent malignant CNS tumors in adults and carry a poor prognosis.[10,11] Gliomas are solid tumors that form in the brain parenchyma and are composed of glial cells and astrocytes. Gliomas as a more general class of tumors are divided into four grades, with grade 4 being glioblastoma. There is no clear association with risk factors for developing CNS tumors; however, the general characteristics of the patient population tend to skew older with a higher incidence in men.[12] Tumor classification schemes have been developed by the World Health Organization (WHO) and are primarily based on histological characteristics with the prognosis and survival becoming shorter with increasing tumor grade.[12] Lower grade gliomas can progress into the more malignant GBMs. Another common feature of gliomas is that they tend to recur even after maximal treatment and recurrence nearly always occurs at the initial primary site. The overall survival without therapy is less than one year.

Glioblastomas are initially diagnosed with imaging modalities, such as computed tomography (CT) and magnetic resonance imaging (MRI).[13] However, due to the infrequency of the tumors, screening is not usually performed. Therefore, diagnosis is either incidental, or much more frequently only after the onset of symptoms. This lack of early detection means that the tumors are large enough (or affecting more critical brain structures) before diagnosis is made; tumors are often greater than 1 cm in size. As tumors grow, they increase intracranial pressure often resulting in compression of brain tissue that can lead to neurologic symptoms. Official diagnosis still requires histology, either from biopsy, or more commonly at the time of surgical resection.[14] Further, glioblastomas are highly aggressive and infiltrative tumors and tumor growth usually progresses rapidly. Gliomas do not metastasize to other parts of the body, and rarely even metastasize to a secondary location within the CNS.

Treatment for glioblastoma includes surgery, radiotherapy, and adjuvant chemotherapy. Despite maximal medical and surgical interventions, the prognosis for glioblastoma only improves to 15 months. The five-year survival for glioblastoma is less than 5%, however younger patients on average tend to have slightly higher 5-year survival rates. The poor prognosis for glioblastoma can be attributed to many factors. One key feature of glioblastoma is its ability to invade into surrounding brain tissue, making complete surgical resection exceptionally difficult. Further, these regions of invading tumor cells are located behind an intact blood brain barrier, which limits the delivery of therapeutic agents. However, the blood brain barrier within the solid tumor is highly disrupted. Further, gliomas are often characterized by extensive edema surrounding the primary tumor site.

In the treatment course, the first and most important step is surgical resection with a goal of removing as much tumor burden as possible while maintaining as much neurological function as possible.[15] Surgical resection is often palliative as recurrence is common due to the inability to remove infiltrating tumor cells. A critical goal of presurgical planning is to be able to clearly delineate tumor margins which is again challenging.[16] Nearly all recurrence is at the initial primary tumor site or in the surrounding surgical resection cavity. Another goal of surgery is for decompression, removing pressure on critical brain structures that may be driving neurological symptoms. Thus, determination of tumor margins as well as regions of infiltrating tumor cells is currently an unmet diagnostic imaging need. Following surgical resection of the tumor, secondary treatments include radiotherapy.[17] Radiotherapy can either be focal or whole brain. Finally, a course of adjuvant temozolomide, an alkylating agent, completes the standard treatment course for newly diagnosed GBM.[18,19]

1.4 Rodent Models of GBM

Although many studies have been conducted on characterizing human GBM samples, manipulation of the tumor microenvironment, testing different chemotherapy strategies, and directly probing the acidity and hypoxia that develops in tumors requires the use of preclinical animal models of GBM. From patient samples, it has been appreciated that many tumors have different driving mutations, morphology, and metabolic profiles, making predicting therapeutic efficacy and forming a cohesive representation of the tumor microenvironment difficult. Therefore, preclinical models of GBM that recapitulate human GBM are needed.

Preclinical models of GBM have focused on a few key rodent cell lines as well as patient-derived cell lines, which are used in immunosuppressed rodents. Rat glioma models include the C6, 9L, RG2, and CNS-1 gliomas [20] and in mice, the GL-261 glioma model. There are several models of GBM in rats (RG2, U87, U251) that have been used for *in vitro* characterization and *in vivo* tumor monitoring. These tumor models reproduce histopathological and imaging characteristics found in human GBM and are useful for tumor characterization and development of imaging modalities. However, the use of stable glioma cell lines has limitations (similar to other tumor models) in that no disease model involving the direct injection of cells fully recapitulates exactly the human condition.

Syngeneic models of GBM in rats include the RG2 cell line, which allows for the tumors to grow in immunocompetent animals. The RG2 tumor was initially generated by the administration of ethylnitrosurea to a pregnant Fisher rat, which resulted in tumor development in offspring that could be collected and maintained *in vitro*.[21] RG2 tumors exhibit invasive growth patterns and are non-immunogenic in Fisher rats. In terms of genetics, RG2 has wild-type p53 and has increased expression of several genes including Ras, cyclin D2, PDGFß, IGF-1, and Erb3/HER3.[22] RG2 cells develop reproducible solid tumors when injected *in vivo* and develop minor necrotic regions independent of tumor size.[5] Minimal signs of inflammation or gliosis outside of the tumor can be identified. RG2 tumors induce disruption of the blood brain barrier and produce edema surrounding the tumor.[21] There is a role of pericytes in RG2 tumors for promoting angiogenesis and leading to increased permeability of the tumor vasculature.[23] Many metabolic studies were performed on C6 cells. The C6 model has been widely used because it has similar genetic changes to those seen in human gliomas; however, it is immunogenic and cannot be used in immunocompetent rats or used to test immunotherapy. It forms pleomorphic cells with variable nuclear sizes and it does invade into surrounding brain. The 9L gliosarcoma is another model used in Fisher rats and is the most widely used glioma model. The 9L tumor is immunogenic and in some cases can be completely eliminated by robust anti-tumor immune responses. However, the tumors formed are well circumscribed and do not demonstrate invasion into surrounding tissue and are not representation of this property of human GBMs. Conversely, the RG2 glioma has a highly infiltrative pattern of growth; however, it is not immunogenic when used in Fischer rats and therefore cannot be used to study immune response or immunotherapy. Human GBMs are generally considered to be weakly immunogenic and this must, to an extent, be replicated in rodents for more representative tumor models. The F98 glioma model is very similar to RG2 except it is weakly immunogenic making it useful for studying immunotherapy. The F98 tumor is also highly invasive and tumor cells are found beyond the tumor core. Finally, the CNS-1 glioma is also highly infiltrative and develops pseudopalisading pattern, a characteristic of human GBM. Further, the tumor becomes infiltrated with macrophages and T cells, as it is highly immunogenic. Similarly, in mice the GL261 tumor can be used for its invasive features and immunogenic response.

Xenograft models include the U251 and U87 cells implanted in athymic/nude rats. Both the U251 and U87 cell lines were derived from patients with pleomorphic gliomas.[24] However, because of the immunosuppressed nature of the animals in these models, they do not allow for studying anti-tumor immune responses or immunotherapies. However, they can be useful for studying tumor characteristics such as invasion, angiogenesis, or the therapeutic response to non-immune mediated therapies. Both U251 and U87 are hypercellular, induce inflammation, and exhibit nuclear atypia.[2] U251 tumors are more invasive than U87 tumors and tumor cells infiltrate to a greater extent and a farther distance from the primary tumor.[25] U251 exhibits greater necrosis and greater expression of hypoxia inducible factor (HIF-1α), suggestive of hypoxia, and greater expression of Ki67, suggestive of higher rates of cellular proliferation.[26] U251 tumors are positive for GFAP and vimentin. They develop pseudopalisading necrosis and exhibit neovascularization and angiogenesis. U87 tumors are positive for vimentin and do not develop necrosis; however, they do exhibit significant angiogenesis. Neither U87 or U251 exhibit endothelial proliferation, a common hallmark of human GBM.[25]

Together, these glioma models have attempted to replicate the genetic changes and morphology of human GBM and recapitulate the tumor microenvironment. Further, in immunogenic models, the anti-tumor immune responses have also been able to be studied and have demonstrated a response to a variety of different therapies as well as characteristics of the tumor microenvironment. However, for eventual translation to clinical care, noninvasive methods to examine the tumor microenvironment need to be developed, which has led to the realm of different translational imaging technologies. Of usefulness in imaging research is the faster translatability of preclinical animal imaging to human studies.

1.5 Tumor Microenvironment

The tumor microenvironment is composed of both tumor cells, the extracellular matrix or stroma, blood vessels and a variety of host cells.[27] The tumor microenvironment is also composed of immune and inflammatory cell,[28] and is understood in the context of a state of chronic inflammation. There also exist direct links between tumor metabolism and the tumor microenvironment.[29] This can be understood because of regions of hypoxia, edema, angiogenesis, and tissue remodeling develop throughout the tumor. The tumor microenvironment in gliomas in the brain has many unique features.[27,30] The extracellular matrix found in the brain, and in gliomas, includes many glycoproteins and proteoglycans.[31] Glioma cells have migratory capacity, suggesting an even more pronounced role of the tumor microenvironment in promoting tumor progression. Specifically, some key features including the presence of tenascin-C, fibronectin, laminin, and collagen lead to tumor cell invasion into surrounding tissue.[32] There also may be a role of cancer stem cells in promoting tumorigenesis as well as tumor progression.[33] The unique composition of the microenvironment makes gliomas more difficult to treat.[34] Additionally, features of the microenvironment are useful for characterizing tumors using imaging methods.[35]

1.6 Angiogenesis

All cells and tissues rely on the vascular system for the delivery of both oxygen and nutrients for cellular metabolism. Capillaries are where gas exchange and nutrient delivery occurs. Additionally, the vasculature is responsible for clearing waste products. In tumors, cells proliferate at a high rate without an initial change in the vasculature, resulting in tumor cells becoming located farther away from the vasculature. This results in regions of the tumor becoming hypoxic. However, tumor cells adapt to this changing landscape by upregulating key molecules resulting in angiogenesis, or the production of new blood vessels. The newly formed vessels are immature, tortuous, and leaky and this characteristic vascular architecture is typically found within tumors.[36] Angiogenesis primarily relies on the production of new blood vessels from existing vessels. Angiogenesis is tightly regulated by both pro- and anti-angiogenic factors; however, of primary importance is vascular endothelial growth factor (VEGF). VEGF induces both angiogenesis and increases the vascular permeability, resulting in leaky vasculature. Without angiogenesis, tumors cannot grow beyond a critical size from which these hypoxic regions develop that will ultimately lead to necrosis.[37] Therefore, angiogenic processes are necessary for sustained tumor growth. Given that the vasculature is present outside of the tumor and this is where angiogenesis occurs, blood vessels tend to be located near the tumor periphery, rather than in the tumor core, which is also why necrosis tends to develop in deeper regions of tumors.

From a therapeutic standpoint, the disrupted vasculature is also critical for understanding the delivery of therapeutic agents to tumors. In GBMs there is an additional consideration that the brain is located behind the BBB, which makes delivery of these agents even more difficult. The BBB is composed of endothelial cells connected by tight junctions, which provide a barrier to nearly all non-selective transport, including both endogenous molecules and exogenous agents.[21] The endothelial cells are associated with astrocytes and together provide for selective transport of glucose and other nutrients as well as allow oxygen diffusion.

The highly abnormal and non-uniform nature of the vasculature results in vessels of varying sizes due to differences in the thickness of the capillary walls and endothelial layer. This abnormal vasculature results in an increase blood volume, but blood flow may be reduced because of the tortuous network. Even regions of tumors that exhibit high vascularity may show a reduction in perfusion with perfusion rates in some tumors being greatly decreased. However, there is a corresponding increase in the permeability of the vasculature such that the driving force for delivery may be reduced. However, the leakiness of the vasculature may allow for greater delivery of drugs or contrast agents to the tumor versus surrounding healthy tissue. There is also a decrease in the ability of tumors to clear waste products. This can be due both to the poor vascularization as well as a less developed lymphatic system in the brain.[38] Anti-angiogenic therapies have attempted to target normalizing the vasculature of tumors.[39]

1.7 Hypoxia

Hypoxia, a reduction in tissue oxygenation, is a hallmark of the tumor microenvironment that results from a decreased vascular supply.[40] Prominent changes in the vascularization of tumors occur as tumors become larger in size and angiogenesis occurs; however, angiogenesis also occurs early in cancer development and is not entirely mediated by hypoxia. Although premalignant lesions are vascularized, the tumor cells are surrounded and separated by a basement membrane. Therefore, tumors initially develop in avascular environments requiring the diffusion of both glucose and oxygen across the basement membrane. As cancer cells proliferate and the tumor increases in size, the necessary diffusion distance increases resulting in only the outermost cells receiving levels of nutrients suitable for sustained growth. Hypoxia develops near the diffusion limit of nutrients, as oxygen does not diffuse as far as glucose, promoting the switch to anaerobic metabolism. Levels of hypoxia within tumors vary with time and can be influenced both by altered blood flow and angiogenesis (promoted by VEGF) once the basement membrane is breached and the tumor becomes vascularized.

The glycolytic switch occurs before the angiogenic switch as lactic acid increases precede changes in vessel permeability.[41] Hypoxia also may not be chronic, but rather fluctuate and vary spatially throughout the tumor. Along with deficiencies in delivering oxygen, the decreased perfusion also leads to a decreased supply of nutrients and an inability to remove metabolic waste products. Cancer cells have a high proliferative rate, which necessitate energy production and synthesis of biomolecules. Although glycolysis may be necessary due to hypoxia, it is an inefficient means of energy production. From these observations, tumor growth and metabolism are tightly regulated to the growth of the vasculature. Further, as the tumor core becomes more hypoxic, necrosis forms and that area of the tumor becomes dormant due to the decreased proliferation. The process of angiogenesis results in expansion of endothelial cells, as well as underlying pericytes;[23] however, the interactions between the endothelial cells and the pericytes is not as strong as in normal vasculature since the vasculature is highly irregular and disorganized resulting in vessels with high permeability.

Hypoxia triggers genetic changes such that signal transducer and activator of transcription 3 (STAT3), an immunosuppressive molecule, is upregulated. STAT3 induces expression of hypoxia inducible factor (HIF-1α), which subsequently increases VEGF. Activation of oncogenes such as epidermal growth factor receptor (EGFR) and loss of tumor suppressor genes such as p53 can both lead to HIF-1α expression.[40] Interestingly, these same mutations also drive many of the metabolic alterations seen in GBM and upregulation of HIF-1α directly upregulates many glycolytic enzymes and downregulates enzymes that target pyruvate for oxidative phosphorylation.[42] HIF-1α also promotes tumor invasion by activating cathepsins, matrix metalloproteinases (MMPs), and transforming growth factor β (TGFβ). In GBM, HIF-1α is expressed at the leading edge of the tumor and corresponds to tumor grade. Fatty acid biosynthesis, required for cellular proliferation, is also upregulated by hypoxia in cancer cells. Hypoxia also induces macrophages to become tumor associated macrophages, also mediated through the STAT3 pathway, and ultimately leads to angiogenesis and invasion. Based on the importance of HIF-1α and VEGF, inhibitors of both molecules are being studied intensely as possible therapeutic targets with most success to date being in anti-VEGF therapies. Interestingly, interactions between anti-VEGF treatments and radiotherapy indicate that hypoxia may decrease the sensitivity of both therapies and further, there is some evidence that when used in combination there is actually an increase in the oxygen tension in the tumor.[43] Areas of hypoxia are thought to trigger genetic changes in tumor cells leading to both increased tumor aggressiveness and heterogeneous cell populations within the tumor. Therefore, even if oxygen levels are restored by angiogenesis, these cells remain more invasive and the decreased sensitivity to both radiotherapy and chemotherapy may remain.

1.8 Acidosis

Cancer exhibits unregulated cell growth and altered metabolism that is shifted towards aerobic glycolysis.[41] In normal tissue, glucose and oxygen are delivered by the vasculature and taken up by cells. Glucose enters the glycolytic pathway and is converted to pyruvate, producing 2 ATP in the process. In the presence of oxygen, pyruvate (the end product of glycolysis) is converted to acetyl-CoA to enter the TCA cycle and fuel oxidative phosphorylation in the mitochondria, producing an additional 30-34 ATP. However, the metabolic phenotype of cancer is one of upregulated glycolysis and reduced oxidative phosphorylation.[44] Although this initial metabolic switch occurs early in cancer development, the driving force behind the metabolic dysregulation is not well understood. The upregulation of glycolysis, as the first metabolic pathway of glucose utilization in cells, necessitates increased glucose consumption to support increased biosynthetic needs. As tumors grow in size, areas of hypoxia develop prior to the development of new vasculature in the tumor (angiogenesis). In the absence of oxygen, pyruvate is converted to the byproduct lactate, in the process reforming NAD^+ to be reused in the glycolytic pathway. Although glycolysis produces NADH from NAD^+, the TCA cycle is the primary producer of NADH to fuel oxidative phosphorylation and together these two pathways are essential for maintaining energy production over a range of oxygen tensions. Glycolysis is normally inhibited by oxygen since oxidative phosphorylation is a more efficient means of energy production, termed the Pasteur effect. Unique to tumors, glycolysis is upregulated even in the presence of oxygen (aerobic glycolysis), termed the Warburg effect. However, as hypoxia develops, metabolism becomes further reliant on glycolysis, exacerbating already altered tumor metabolism. The glycolytic switch precedes the development of hypoxia in the tumor and is therefore thought to be more than just a reaction to the hypoxic conditions; however, a key regulator of the glycolytic response is HIF-1α, which induces increased expression of glucose transporters, VEGF to promote angiogenesis, and the glycolytic enzyme hexokinase.

Genetic mutations in p53, KRAS, and MYC (found in many cancers) accompany some of these metabolic changes and act as a direct link between cancer genetics and metabolism.[42,45,46] In some cancers, the capacity to undergo oxidative phosphorylation is reduced such that if glycolysis is downregulated, the cells are no longer able to compensate in energy production,[47] indicating that genetic changes at the cellular level reduce metabolic fitness. However, altered metabolism allows cancer cells to be better suited for proliferation, a hallmark of cancer, rather than energy production as several signaling pathways are involved in both proliferation and metabolism. Proliferating cancer cells exhibit anabolic metabolism and add to the tumor mass by incorporating nutrients into nucleotides, amino acids, and lipids. Although uncontrolled proliferation is normally prevented by growth factor regulation, cancer cells overcome the regulatory mechanisms by constitutively activating pathways leading to nutrient uptake. However, resistance to therapies that reduce the proliferative and replicative potential of tumors may be due to acquired mutations that change the metabolic phenotype to relying on mitochondrial function to a greater extent.[48] Oxidative phosphorylation is accomplished in mitochondria by the flow of electrons through complexes anchored in the mitochondrial membrane. As oxidative phosphorylation decreases, the reduced function of the electron transport chain allows reactive oxygen species (ROS) to form, which maintains the cancer cell phenotype and leads to further genetic instability, altered metabolism, and increased tumor invasion. Although mitochondrial function is not directly impaired, the metabolic decoupling from oxidative phosphorylation necessitates increased glycolysis. Further, the ROS generated are toxic to cells and would seem to contradict the replicative advantage seen in cancer; however, the upregulation of glycolysis also produces reducing equivalents to handle the oxidative stress associated with increased ROS production.[3]

Additionally, with the upregulation of glycolysis and decreased oxidative phosphorylation, there is both a generation of protons and increased lactate production that result in an acidic intracellular environment (**Figure 1.1**). As acidity is toxic to cells, expression of Na^+/H^+ cotransporters and vacuolar H^+-ATPases is increased to neutralize the intracellular pH and shift the acidic conditions to the extracellular environment. However, exposure to acidic conditions in the extracellular environment promotes necrosis and apoptosis. Since carcinogenesis is accomplished by the selection of specific cell populations with the greatest growth advantage, selected cancer cell phenotypes become resistant to acid induced cell toxicity. The glycolytic phenotype (including extracellular acidosis) may offer a selective advantage to tumor cells because the acidic conditions are toxic to surrounding cells (not adapted to survive in acidic conditions). Further, the low pH increases degradation of the extracellular matrix (ECM) by upregulating metalloproteinases and cathepsins, increasing invasiveness, again a hallmark of cancer. In total, the metabolic changes seen in cancer are a fundamental property of the genetic mutations and altered enzyme expression that lead to a proliferative and replicative advantage.

Lactate is found in the highest concentration in the most hypoxic tumor regions.[49,50] Lactate can also serve as an additional fuel for other cells that are able to capture lactate and utilize it as a metabolic fuel. However, maintaining a near neutral intracellular pH is critical for maintaining the fluxes needed for lactate transport. There are also changes in lipid metabolism, mainly in the carboxylation of alpha-ketoglutarate, that are specifically seen with isocitrate dehydrogenase (IDH) mutations in GBM.

Acidosis in the tumor microenvironment has been associated with many features of cancer progression including remodeling of the extracellular matrix, tumor invasion and metastatic spread.[7,8] Acidosis leads to activation of proteases that disrupts or alters adhesion proteins between cells and between cells and the matrix. Further, proteases found in lysosomes are most active under acidic conditions. Lysosomes may also be involved in removing excess protons from the cytosol if upregulation of transporters was not able to sufficiently remove the amount of generated protons. Tumor regions with the greatest acidity (lowest pH) are areas where the tumor is likely to invade. Acidosis also results in increased angiogenesis due to the release of pro-angiogenic molecules normally found in the extracellular matrix and triggers cells to have more stem-cell like properties. The acidic pH_e (and corresponding alkaline pH_i) contribute to many features of the tumor microenvironment (**Figure 2.2**) and several key impacts of the acidic microenvironment will be discussed individually.

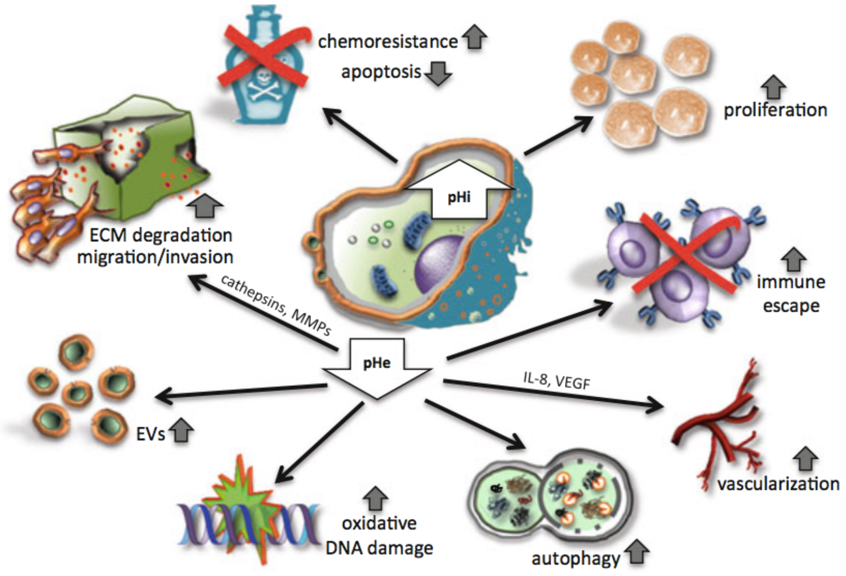

Figure 1.2. Effects of pH changes on the hallmarks of cancer. Dysregulated metabolism leads to a decrease in the extracellular pH (pH_e) along with an increase in the intracellular pH (pH_i). The decrease in pH_e leads to tumor invasion into surrounding tissue, an upregulation of angiogenesis leading to increased vascularization, and aids in creating an immunosuppressive environment resulting in immune escape. The increase in pH_i results in an increased rate of cellular proliferation and a resistance to undergoing apoptosis. Reproduced with permission.[51]

1.9 Acidosis results in tumor invasion

Altered metabolism does not only respond to the tumor microenvironment (hypoxia) but also helps shape it (lactate and proton production and extracellular acidosis). Although hypoxia and acidosis are prominent features of the tumor microenvironment, in GBM the tumor microenvironment is complex and optimal for cancer cell survival, invasion, and metastasis. A unique element of the GBM environment is the presence of tight junctions on the foot processes of astrocytes that forms the foundation of the BBB. Similar genetic alterations that lead to changes in tumor metabolism also play a role in the remodeling of the extracellular matrix (ECM).

The tumor microenvironment is composed of stromal, endothelial, and immune cells in addition to tumor cells. Of emerging importance in the GBM microenvironment is the role of cancer stem cells, which are characterized by expression of CD133 and exhibit a specific phenotype of self-renewal and proliferative advantage.[33] Although a small population of the heterogeneous collection of cells within the tumor, these cells are capable of maintaining the tumor and are surrounded by ECM composed of collagen, glycoproteins, and proteoglycans, which supports tumor cells and creates a specific niche.[31] Integrins located on the cell membranes of stem cells interact with the ECM, triggering cytoskeleton remodeling, proliferation, and gene transcription. Therefore, changes in the ECM can have direct impacts on cellular signaling, cancer cell survival, and invasion into surrounding tissue.

A critical element of tumor development is angiogenesis as a tumor vascular supply is critical for the delivery of oxygen and nutrients. The angiogenic switch occurs later than the glycolytic switch, but is driven by both hypoxia and oncogene activation, primarily through VEGF.[41,52] Further, the stem cell niche is tightly coupled to vascular areas of the tumor. However, the vessels produced through angiogenesis are immature with excessive branching leading to increased vessel permeability and micro-hemorrhages. Finally, there is a role for proteases, such as matrix metalloproteinases (MMPs), that degrade the ECM and lead to local invasion. Although some cancer cells may directly secrete MMPs, other cancer types secrete chemokines that attract protease-secreting proinflammatory cells. In general, however, the tumor microenvironment is immunosuppressive and immune evasion is increasingly becoming evident as a hallmark of cancer.[53]

Solid tumors maintain an acidic extracellular environment with extracellular pH values of 6.2-7.0 being reported (normal tissues have a pH of 7.2-7.5).[54] The altered metabolism in tumors, described previously, results from both genetic changes as well as changes in the tumor microenvironment, such as hypoxia.[42] Acidosis, much like hypoxia, can also vary spatially within tumors.[44] The dysregulation of metabolism results in extracellular acidosis and is directly connected to changes in the tumor microenvironment. For example, mutations in certain oncogenes, such as those found in GBM, upregulate lactate dehydrogenase, glucose transporters and glycolytic enzyme activity, all of which are necessary for regulating tumor cell metabolism. However, acidosis also activates the tumor suppressor p53, which may reactivate oxidative phosphorylation and might aid in alleviating oxidative stress from ROS. Ultimately, loss of function mutations in p53 with chronic acidosis limit this alternate pathway, fully shifting tumor cell metabolism to the predominately glycolytic phenotype. Although the early shift in metabolism is not entirely understood, it results in the selection of cell populations resistant to acid-induced toxicity. In addition to lactate production, protons are also generated by the hydrolysis of ATP and carbonic anhydrase activity. The end result is that protons and lactate accumulate in the interstitial environment.[42] Further, the deregulated pH results in tumor growth and cancer progression.[55] Specifically, an acidic extracellular pH increases proliferation, angiogenesis, and invasion. In gliomas, the decreased extracellular pH can increase the invasiveness by increasing the expression of extracellular degrading proteases which disrupts the basement membranes of the extracellular matrix, promoting tissue invasion.[56]

Although the acidic extracellular pH originates from within the tumor habitat, it is also thought to drive local invasion.[57] The direction of tumor infiltration directly follows the areas with the lowest extracellular pH. The altered pH results in the genetic upregulation of ionic transporters. Specifically, there is an upregulation of the Na^+/H^+ cotransporter to remove protons from the intracellular environment and monocarboxylate transporters (MCTs) to remove lactate, shifting the acidity to the extracellular environment.[58] Additionally, low extracellular pH also promotes angiogenesis through interleukin 8 (IL-8) and VEGF.[51] As metastasis is the process where migratory cells invade the basement membrane, enter the bloodstream, and then spread to distant sites, cells grown in acidic conditions showed greater motility and invasion and may be better enabled to extravasate through fenestrae in blood vessels leading to metastasis.

1.10 Acidosis hinders therapeutic response

Due to the effects of acidosis on promoting a favorable environment for continued tumor growth, the acidic extracellular pH has been proposed as a target for cancer treatment.[59,60] Alkalinizing the extracellular environment can lead to increased sensitivity to some chemotherapy agents and decrease the rate of metastasis.[60] Further, because certain chemotherapy agents have ionizable functional groups with characteristic acid dissociation constants (pK_a), there can be improved response to some therapies with normalization of the tumor pH.[61-63] Low pH decreases sensitivity of radiation therapy, but can also be exploited to enhance delivery of weak-acid chemotherapy agents.[56] Further, the acidic extracellular pH has been exploited to deliver chemotherapy agents in an acidosis-dependent manner such as with the use of low pH insertion peptides (pHLIP). These can also be exploited in the design of nanoparticle-based therapeutics where the drug-containing nanoparticle can be designed to target areas of low pH.[64,65] Because there are few tissues in the body that are highly acidic (muscle and kidneys are notable exceptions) this provides a unique route of specific tumor targeting of therapeutics, but also may explain the muscle and renal toxicities exhibited by many chemotherapeutics.

1.11 Acidosis is immunosuppressive

Specifically, in GBM, acidic extracellular pH promotes a glioma stem-cell like phenotype through the impact of acidic pH on the tumor microenvironment.[66] Immune responses can also be impacted by acidosis such that cytokine production by activated T cells can become inhibited.[67] There is metabolic competition in the tumor microenvironment as nutrients may be diverted from anti-tumor immune cells to the tumor cells themselves resulting in decreased anti-tumor immunity.[68] Acidosis (including lactic acid) impairs many aspects of immune function including chemotaxis, proliferation, and cytokine production. In acidic conditions, T cells are not able to effectively recognize or respond to cancer-specific antigens. There are also direct effects on neutrophil and macrophage function.[67] Therefore, the acidic pH_e has a twofold effect on cancer progression, both by directly increasing proliferation and invasion and decreasing anti-tumor immunity.

Altered anti-tumor immunity is emerging as a hallmark of cancer. However, it should come as no surprise that altered metabolism, acidosis, and hypoxia (previously established as necessities to promote tumorigenesis) all contribute to decreased immune function in the tumor microenvironment. Although immunotherapy is a novel approach to cancer treatment, using the body's naturally occurring immunity to combat tumor cells, its applicability to gliomas has been questioned due to the immune privileged site of the CNS. Sitting behind the selective blood-brain barrier (BBB), it was thought that immune cells did not readily penetrate the CNS and further it is well known that many chemotherapeutics and other pharmaceuticals do not penetrate the CNS with high efficacy. Initial studies with immunotherapy in GBM were suboptimal as difficulties with treating GBM stemmed from a lack of understanding of tumor biology, metabolism, and the microenvironment. In a recent review of the difficulties with immunotherapy in GBM, many of these factors were examined.[69] Although the BBB was thought to maintain this separation, recent evidence suggests that a "glymphatic system" is present and located within the dura, allowing immune cells to cross into the CNS.[38] Lymphocytes have been found in the tumor microenvironment and immunoglobulins are also able to cross the BBB by carrier-mediated transport involving a specific receptor. Further, antigen-presenting cells have also been found in many areas of the brain. Although peripheral immune cells are unable to enter the brain due to the integrity of the BBB, in disease states the BBB becomes disturbed, facilitating the invasion of immune cells into the tumor microenvironment.

Specific interest has revolved around programmed cell death molecule 1 (PD-1) and its ligand (PDL1), which acts as an immune checkpoint and is expressed on microglia. PD1 inhibitors have gained recent attention for their role in promoting immune responses in renal cancer, lung cancer, and melanoma. PD-L1 has been found in human gliomas and expression was found to correlate with tumor grade.[70] Many different strategies for immunotherapy for glioblastoma in preclinical (as well as clinical) studies are underway.[71] PD1 is an inhibitory receptor that inhibits the T cell response after antigen activation and is upregulated when surrounding T cells undergo apoptosis. Interestingly, the efficacy of anti-PD1 therapies is dependent on extracellular acidosis, as low pH decreases the sensitivity of immunotherapy.[61]

Further, a variety of other immune cells are impacted by the tumor microenvironment, specifically macrophages and T cells, which are the foundation of the anti-tumor immune response.[72] In general, the tumor microenvironment is immunosuppressive and interrupts antigen presentation by downregulating MHC expression. Immunosuppression is achieved by inhibiting T cell proliferation and pro-inflammatory cytokine release, as well as by activating regulatory T cells. The upregulation of glycolysis also creates an environment where glucose supply is restricted having significant consequences on T cell metabolism and inhibiting their ability to secrete cytokines.[68] Therefore, even if tumors are highly antigenic, the T cells may not have the nutrient source in order to respond appropriately. The pro-inflammatory cytokines such as interferon gamma (IFN-γ) and tumor necrosis factor alpha (TNFα) are downregulated through IL-10, an immunosuppressive cytokine. The immunosuppressive cytokines include IL-6, IL-10, and TGFβ and their secretion is upregulated in the tumor microenvironment. In GBM, TGFβ promotes both tumor growth and invasion by promoting a GBM stem cell phenotype and angiogenesis. Hypoxia, through activation of HIF-1, will directly activate regulatory T cells (Treg) to modulate the immune response as well as promote the differentiation of macrophages into tumor-associated macrophages (TAMs), which secrete immunosuppressive cytokines. Similarly, acidosis results in the decreased release of pro-inflammatory cytokines (TNFα and IFN-γ) by macrophages.[67] In summary, the entirety of the tumor microenvironment, which is driven by initial genetic mutations and altered metabolism, plays a role in immune evasion and suppression to augment tumor cell progression.

1.12 Implications for clinical cancer imaging

In cancer imaging, a variety of methods have repeatedly demonstrated that extracellular pH is spatially heterogeneous throughout tumors and can be correlated with increased lactate levels.[73] Further, the intracellular pH of tumors remains neutral to alkaline even in the presence of a very acidic extracellular environment.[74,75] Finally, the pH gradient between the intratumoral and peritumoral environment is steeper with less invasive tumors; therefore, the pH gradient can be used as a marker of tumor invasiveness. More invasive tumors have more extensive pH abnormalities and the acidic pH spreads far beyond the tumor boundary.[76] The genetic mutations driving initial cancer formation, the altered metabolism resulting in the upregulation of glycolysis, and the variably hypoxic and acidic tumor microenvironment are now all thought to be hallmarks of cancer and most interestingly, to each be related to one other. Further, the most recent developments in cancer therapy, immunotherapy, are now being found to be dependent on the tumor microenvironment as hypoxia and acidosis directly impact the anti-tumor immune response. The role of developing novel techniques to image the tumor microenvironment in both preclinical models and in clinical practice will only become more relevant and of greater importance as cancer research continues to expand. In the next chapter, the imaging methods to characterize the vascular tumor microenvironment and measure the pH_e will be discussed in detail.

Chapter 2: Metabolic Imaging Methods in Cancer

2.1 Abstract

Acidification of the tumor microenvironment by altered cellular metabolism is a hallmark of cancer. Metabolic dysregulation promotes a switch to glycolysis even in the presence of oxygen, termed the Warburg effect, and enables overproduction of lactate and protons that initially accumulate in the intracellular compartment only to be later extruded into the extracellular space. Therefore, there is great interest in imaging acidosis found in solid tumors. However, imaging methods to measure pH, especially for tumors not located on the skin surface, are challenging. Methods to measure pH have evolved from placing pH electrodes directly into surface tumors or using optical imaging methods to noninvasive imaging methods using magnetic resonance imaging (MRI) and spectroscopy (MRS) or positron emission tomography (PET). Each technique has certain advantages and disadvantages, vary in their spatiotemporal resolution, and may use endogenous contrast or the infusion of exogenous pH-sensitive contrast agents. In this chapter, after a general introduction to MR methodology, a review of the methods available for imaging the pH in the tumor microenvironment will be explored.

2.2 Magnetic resonance imaging (MRI) and spectroscopy (MRS)

MRI is a noninvasive medical imaging modality that does not use ionizing radiation to detect hydrogen atoms of water and is utilized for its excellent tissue contrast properties and capability for three-dimensional imaging. The principles of nuclear magnetic resonance (NMR) govern MRI, resulting in several applications such as spatially encoding information with linear magnetic field gradients to yield an image (MRI) or investigating a range of frequencies to yield a spectrum of molecules other than water (MRS). Since the 1970s, when the use of MRI as a medical imaging tool was realized when it was shown that normal and cancerous tissue resulted in different MRI contrast,[77] MRI has continued to expand in the medical community and become a prominent technique in diagnostic imaging. To fully appreciate the underlying methods that contributes to the utility of MRI, the basis of the MRI signal will be discussed.

2.2.1 Nuclear Spin

Protons and neutrons within an atom have an intrinsic angular momentum (spin) such that atomic nuclei that have an odd number of protons and/or neutrons have a non-zero spin. The rotating charged particles generate a magnetic moment. Each spin is randomly oriented; however, when an atom with a net nuclear spin (such as ^{1}H) is placed in an external magnetic field (B_0), the magnetic moment will align with B_0 in one of two orientations: parallel with B_0 in a low energy state, or anti-parallel with B_0 in a high energy state where the difference in energy between the states for ^{1}H nuclei is given by **Equation 2.1** where γ is the gyromagnetic ratio and h is Planck's constant (h =6.62 x 10^{-34} m^2kg/s).

$$\Delta \mathrm{E} = \gamma h \mathrm{B}_0 \qquad \textbf{(Equation2.1)}$$

For an ensemble of spins, the system forms an equilibrium and it is the difference in number of spins between these two states that leads to a non-zero magnetization, usually termed net magnetization (M_0). The fact that M_0 depends on the difference in spin populations and not the total number of spins leads to the inherent low sensitivity of MRI. The net magnetization depends on the total number of spins (N), the external magnetic field strength (B_0), the temperature (T) and Boltzmann constant (k = 1.38 x 10^{-23} m^2kg/s^2K) as given by **Equation 2.2** and illustrates that greater magnetization is achieved at high spin concentration and higher magnetic field strength.

$$M_0 = \frac{N\gamma^2 h^2 B_0}{4kT} \qquad \textbf{(Equation 2.2)}$$

The nuclear spins in an external magnetic field rotate at a characteristic resonance frequency (Larmor frequency) that is dependent on the gyromagnetic ratio and the external magnetic field strength (B_0) according to **Equation 2.3**.

$$\omega = \gamma B_0 \qquad \textbf{(Equation 2.3)}$$

For example, the ^{1}H nucleus has a γ of 42 MHz/T such that 11.7T, the resonance frequency is 500 MHz; however, each nucleus has a characteristic resonance frequency at a given magnetic field strength. Many elements have an isotope that will have a net magnetic moment; however, few elements have isotopes with a net magnetic moment at high natural abundance. The ^{1}H nucleus is a notable exception with a net magnetic moment, a high gyromagnetic ratio, a natural abundance near 100%, and an extremely high tissue concentration (from the signal in water and fat) making this the most sensitive and important isotope for MRI experiments. A comparison of other nuclei with ^{1}H is shown in **Table 2.1**.

Nuclei	**Spin**	**Natural Abundance (%)**	**Gyromagnetic Ratio (MHz/T)**
^{1}H	**1/2**	**99.985**	**42.48**
^{19}F	**1/2**	**100**	**40.08**
^{31}P	**1/2**	**100**	**17.25**
^{23}Na	**3/2**	**100**	**11.27**
^{13}C	**1/2**	**1.11**	**10.71**
^{2}H	**1**	**0.015**	**6.54**
^{17}O	**5/2**	**0.0373**	**5.8**
^{14}N	**1**	**99.63**	**3.08**

Table 2.1. Comparison of nuclei based on their natural abundance and gyromagnetic ratio. Nuclei with the highest gyromagnetic ratios and highest natural abundance have the greatest NMR sensitivity.

2.2.2 Excitation

The MR experiment is based on using radiofrequency (RF) energy at the resonance frequency in order to manipulate the different populations of spins. The B_1 field refers to magnetization applied perpendicular to B_0 that briefly rotates spins out of alignment with B_0 in a process termed excitation. RF pulses are applied using a transmitter coil that is tuned to the resonance frequency of the nuclei under study and impedance matched to allow efficient power transfer. Depending on the NMR experiment type, the same RF coil can be engineered to also be a receiver or an alternative RF coil can be used as the receiver.

The direction of the main magnetic field (B_0) is defined as the z direction by convention and the net magnetization is aligned in the same direction (M_z). The amount of rotation of the magnetization (M_z) out of alignment with B_0 can be varied by the intensity or duration of the applied B_1 field. An excitation pulse is achieved when M_z is tipped 90°, such that the magnetization is completely in the xy-plane (M_{xy}) and the M_z component is 0. If the duration of B_1 is doubled, an inversion pulse is achieved and M_z is rotated 180°, such that the magnetization is equal to $-M_z$. After the RF is switched off, the magnetization begins to return to equilibrium in a process termed relaxation. Magnetization in the xy-plane precesses around the z axis at the resonance frequency and is the signal that is ultimately detected in MR experiments.

2.2.3 Relaxation

After excitation, the spins relax back into alignment with B_0 in a process governed by the relaxation parameters T_1 (longitudinal relaxation in the direction of B_0) and T_2 (transverse relaxation in the xy-plane), which is detected as the MR signal. The magnetization as a function of time is governed by the relaxation processes and mathematically represented by the Bloch equations. The magnetization in each direction (M_x, M_y, or M_z) is shown in **Equation 2.4**.

$$\frac{dM_x}{dt} = \gamma M_y B_0 - \gamma M_y B_{1,y} - \frac{M_x}{T_2}$$

$$\frac{dM_y}{dt} = \gamma M_z B_{1,x} - \gamma M_x B_0 - \frac{M_y}{T_2}$$

$$\frac{dM_z}{dt} = \gamma M_x B_{1,y} - \gamma M_y B_{1,x} - \frac{M_z - M_0}{T_1} \qquad \text{(Equation 2.4)}$$

The T_1 relaxation time is the first-order rate constant that governs the relaxation of the M_z component of magnetization back into equilibrium and is based on the exchange of energy with the surrounding environment (lattice). After a 90° RF pulse, the net magnetization is tipped into the xy-plane such that $M_z=0$ after which the M_z then recovers along the z axis. The T_1 relaxation is governed by **Equation 2.5** where TR is the repetition time, or time between successive excitations (the amount of time M_z is allowed to recover).

$$M_z = M_0\left(1 - e^{-\frac{TR}{T_1}}\right) \qquad \text{(Equation 2.5)}$$

T_2 is based on spin-spin interactions and loss of phase coherence due to the interaction between nearby spins and refers to the loss of the spin ensemble (i.e., the magnetization) in the transverse plane. As the protons spin, they induce small magnetic fields that impact neighboring spins. After the B_1 field is applied, all spins are in phase; however, as the spins relax, they lose phase coherence, decreasing the net magnetization in the xy-plane according to **Equation 2.6** where TE is the echo time and is the time between the RF pulse and data acquisition.

$$M_{xy} = M_0 e^{-\frac{TE}{T_2}} \qquad \text{(Equation 2.6)}$$

However, magnetic field inhomogeneities result in spins losing phase coherence even faster than would be expected. The observed transverse relaxation rate is called T_2^* and accounts for the inhomogeneities that occur due to a variety of reasons including susceptibility artifacts in tissues or the presence of any nearby paramagnetic materials. The T_2^* is always shorter than T_2, is measured in a different manner than T_2 and can be beneficial if contrast agents that have strong T_2 effects are used. MRI acquisition with multiple TE values is used to measure both T_2 and T_2^* using spin echo and gradient echo methods, respectively.

The relationship between T_2 and T_2^* is given in **Equation 2.7** where T_2' is the relaxation effects due to susceptibly effects or magnetic field inhomogeneities.

$$\frac{1}{T_2^*} = \frac{1}{T_2} + \frac{1}{T_2'} \qquad \text{(\textbf{Equation 2.7})}$$

The T_2^* is also related to the spectral linewidth according to **Equation 2.8**, where $\omega_{1/2}$ is the linewidth at half maximum, such that short T_2^* results in significant line broadening.

$$\omega_{1/2} = \frac{1}{\pi T_2^*} \qquad \text{(\textbf{Equation 2.8})}$$

As the spins relax, they induce a voltage in an RF receiver coil. The MR signal eventually decays back to zero as all spins are back in their equilibrium alignment with B_0, and no longer releasing RF energy to the lattice.

2.2.4 Sequences

Magnetization cannot be detected directly in the M_z direction, but must be present in the M_{xy} plane. To manipulate the magnetization, pulse sequences are used that alter the alignment of the net magnetization. The two most common MRI sequences that are used are the spin echo and the gradient echo.

The spin echo sequence is a 90° pulse to rotate M_z into the xy-plane and followed after a time delay by a 180° pulse to refocus the spins that have dephased during the delay. After an identical delay, the spins will be back in phase resulting in an echo, which is when data is acquired. The total delay, from excitation pulse to data acquisition is the TE. Due to the refocusing pulse, the susceptibility effects and magnetic field inhomogeneities will be cancelled out resulting in pure T_2 decay. The T_2 can be measured using a spin echo sequence and varying the TE, which will yield an exponentially decreasing function governed by T_2 (**Equation 2.6**). Additionally, the T_1 can be measured using a spin echo sequence and varying the TR, which will yield an exponential rise-to-max equation with T_1 as the time constant (**Equation 2.5**). While a spin echo sequence provides excellent image quality, the scans are long. The spin echo sequence can be accelerated by applying multiple 180° pulses within a single TR resulting in acquisition of multiple echoes.

The gradient echo sequence is similar to the spin echo, but instead of using a refocusing RF pulse, uses gradients to produce the echo. Since there is no refocusing pulse, this sequence is used to measure T_2^*. The T_2^* can be measured by varying the TE, which will yield an exponentially decreasing function similar to T_2.

The variations in the MR signal, represented in gray scale in MR images, are based on the amount of net magnetization remaining when measured at specific time intervals after excitation. The pulse sequence chosen is used to maximize one form of contrast, and usually in an imaging session multiple imaging sequences are performed to gain the most information as the complex combination of parameters are altered in different ways based on changes in anatomic structure and physiology.

2.2.5 Contrast

Different amounts of T_1 or T_2 weighting can be encoded onto an image based on the selection of the TR and TE; short TE and short TR yield T_1 weighting while medium TE and long TR yield T_2 weighting. In T_1-weighted images, short TR does not allow much magnetization to recover and therefore it reaches a steady state where the signal intensity is low. At long TR, most of the magnetization has recovered and signal intensity is high. At a given TR, the faster (shorter) the T_1 relaxation time, the more signal recovers and it appears brighter in the image. In T_2-weighted images, short TE does not allow much magnetization to dephase and therefore the signal intensity is high. At long TE, most of the magnetization has dephased and signal intensity is low. At a given TE, the faster (shorter) the T_2 relaxation time, the more signal that decays and it appears darker in the image. Other weighting measures can also be encoded in sequence design including proton density, apparent diffusion coefficient (ADC), and magnetization transfer.

Intrinsic T_1 contrast is usually insufficient for identifying pathological tissue. For example, although tumors do typically have higher T_1 values than surrounding tissue, the contrast is unable to identify anatomic demarcations. To increase the contrast, agents can be administered to alter the relaxation properties of the MR signal in voxels in which the agent is present. Contrast agents for MRI may be either diamagnetic or paramagnetic; however, most commonly used contrast agents rely on the presence of a paramagnetic ion to induce magnetic field distortions and shorten T_1 relaxation times. Some common clinically used contrast agents are shown in **Figure 2.1**. However, many of the lanthanide metals used for these purposes are toxic and therefore need to be conjugated to a macrocyclic chelate which provides a stable molecular structure to deliver the metal while avoiding any undesired toxicity. The most common toxicity is nephrogenic systemic fibrosis and occurs most frequently in those with impaired renal function.

Contrast agents work by shortening the relaxation rates in a concentration dependent manner. Due to the concentration dependence, greater contrast is achieved in regions where the contrast agent accumulates to a greater extent. Contrast agents are evaluated based on their relaxivity (r_1 or r_2) and reduces the relaxation times (T_1 or T_2) according to **Equation 2.9** where $T_{1,0}$ is the intrinsic T_1 relaxation time without the contrast agent and [CA] is the concentration of the contrast agent.

$$\frac{1}{T_1} = \frac{1}{T_{1,0}} + r_1[\mathrm{CA}] \qquad \textbf{(Equation 2.9)}$$

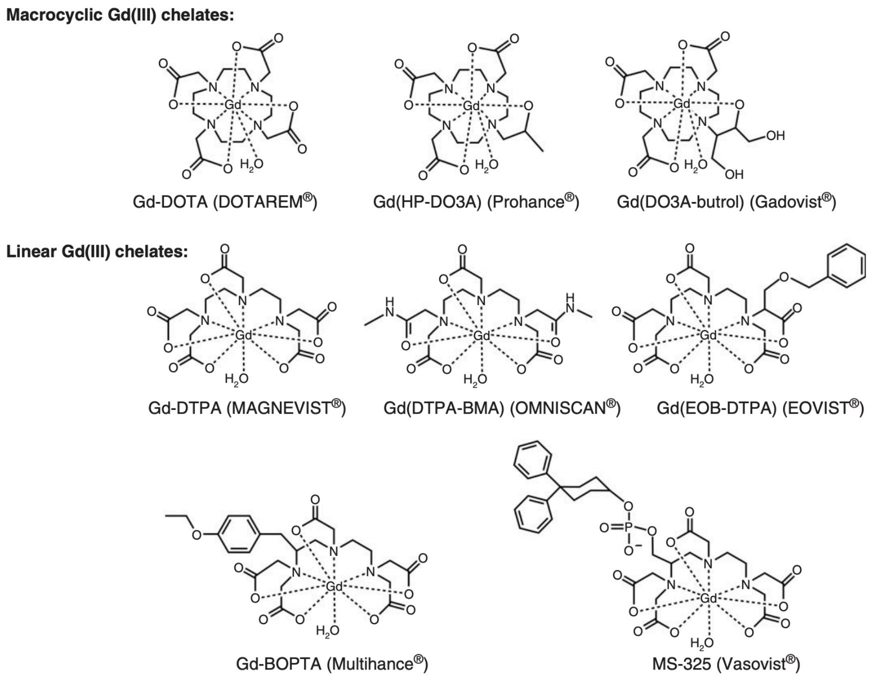

Figure 2.1. Molecular structure of commonly used gadolinium-based contrast agents. The macrocyclic versions of these agents are used most frequently due to improved safety profiles. The macrocyclic agents are based on a 1,4,7,10-tetraazacyclododecane backbone. Reproduced with permission.[78]

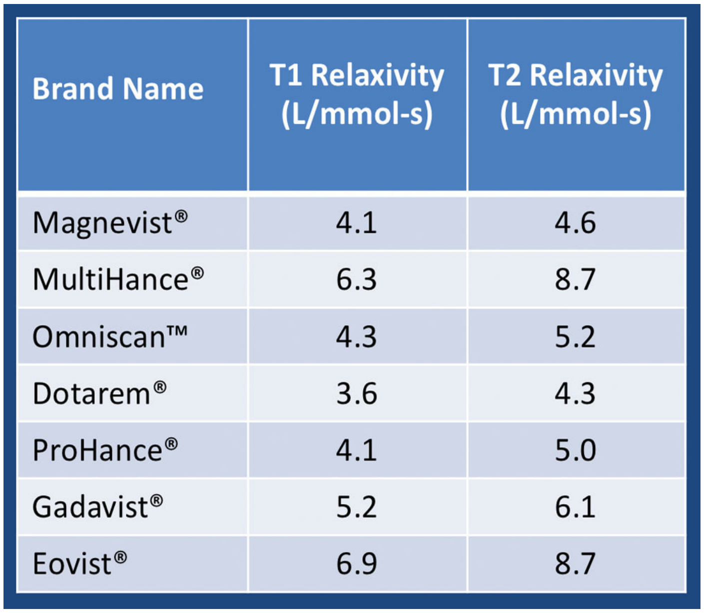

Brand Name	T1 Relaxivity (L/mmol-s)	T2 Relaxivity (L/mmol-s)
Magnevist®	4.1	4.6
MultiHance®	6.3	8.7
Omniscan™	4.3	5.2
Dotarem®	3.6	4.3
ProHance®	4.1	5.0
Gadavist®	5.2	6.1
Eovist®	6.9	8.7

Table 2.2. Relaxivities for common contrast agents. Agents with higher relaxivities have a great effect on the relaxation rates, which leads to greater contrast at the same agent concentration.

Therefore, in pathologies where contrast agents are taken up to a greater extent than healthy tissue will become readily visible on appropriately weighted MRI. Most clinically used contrast agents contain gadolinium and reduce T_1 to a greater extent than T_2. However, there are agents that more efficiently reduce T_2 and are traditionally based on Fe in the form of superparamagnetic iron oxide (SPIO). The reduction in T_1 and/or T_2 relaxation leads to positive or negative contrast in T_1 or T_2-weighted imaging, respectively.

Because these agents work by exerting effects on the relaxation of the water signal, they are not directly detected. However, MRS techniques (described in a later section) can directly detect resonances that emanate from protons on the contrast agent. Gadolinium, however, is the most paramagnetic lanthanide agent and has much higher relaxivity, resulting in much shorter relaxation times. Additionally, the T_2 shortening results in significant line broadening that results in the signal being undetectable by MRS. Agents with other lanthanide metals (e.g., thulium), while less paramagnetic, have relaxation times that result in less signal broadening and allow hyperfine shifts that can be directly detected. Lanthanide agents can act as contrast agents by shortening relaxation times, but in some cases can also act as shift agents by causing a change in the chemical shift as is most commonly seen in ^{23}Na MRS.

2.2.6 Magnetic Resonance Imaging (MRI)

In order to generate an image in MRI, magnetic field gradients are applied to allow spatially localized volumes to be specified. Gradient coils create linearly varying magnetic fields that change the resonance frequency of the spins, such that the resonance frequency of individual spins becomes dependent on spatial location. In slice-selective 2D imaging, a slice is first designated by applying a slice-selective RF pulse corresponding to the resonance frequency range defined by the magnetic field gradient in the slice orientation desired. The slice thickness is determined by the strength of the slice-selective gradient and the RF pulse bandwidth. The two in-plane directions (spatial encoding) are specified by frequency encoding and phase encoding after slice selection. The phase is encoded prior to data acquisition in one dimension while the frequency is encoded during data acquisition in the other perpendicular dimension using a similar approach with magnetic field gradients as used for slice selection. Each unique volume (voxel) is identified with a unique frequency and phase and the signal intensity corresponding to the frequency and phase is used to generate an image.

2.2.7 Diffusion weighted imaging (DWI)

MRI methods have also been adapted to be sensitive to the diffusion of water. The apparent diffusion coefficient (ADC) is a measure of movement of water molecules within an MRI voxel.[79] Diffusion-weighted imaging is based on the spin echo pulse sequence, but utilizes an additional diffusion encoding gradient before and after the 180° refocusing pulse. Nuclei that remain within the imaging voxel during this diffusion time, contribute to the imaging signal, while nuclei that diffuse out of the imaging voxel no longer contribute to the signal. Therefore, by measuring the signal at different durations of the diffusion time can allow the ADC to be quantitatively measured. The strength of the diffusion gradient (denoted b values) is based on the gradient strength (G), duration (δ) and delay (Δ) according to **Equation 2.10** when using symmetric diffusion gradient pulses.

$$b = \gamma^2 G^2 \delta^2 \left(\Delta - \frac{\delta}{3}\right) \qquad \text{(\textbf{Equation 2.10})}$$

Similar to how T_2 is measured by spin echo MRI (**Equation 2.6**), the ADC can be measured using a spin echo sequence by varying the b values to yield an exponentially decreasing function governed by ADC (**Equation 2.11**).

$$\mathrm{M} = \mathrm{M_0 e^{-b(ADC)}} \qquad \textbf{(Equation 2.11)}$$

In solution, diffusion is unrestricted, resulting in high values for ADC. However, in cells and tissues, the inhomogeneous environment results in barriers to diffusion due to cell membranes and the tissue structure that result in a reduction in ADC. In cancer imaging, the ADC is linked to the cellularity of the tumor as more highly cellular tumors have greater diffusion restriction and lower ADC values.[80] Heterogeneity within tumors are also reflected in varying ADC values; in particular, regions of necrosis which are more acellular, have higher ADC values.

2.2.8 Dynamic Contrast Enhanced MRI

Dynamic contrast enhanced (DCE) MRI is a tool that models the dynamic uptake of an exogenous contrast agent and uses a mass conservation equation to model vascular parameters based on the delivery, exchange, and clearance of the contrast agent in different tissue compartments.[81] Contrast agents are delivered by an intravenous injection and are present initially only in the blood. However, in some vasculature the contrast agent extravasates into the interstitial (extracellular) space. The arterial input function (AIF) is modeled based on the contrast agent concentration in a blood vessel over time and can be measured by selecting a region in a large blood vessel in the image. The AIF is based on a bolus delivery of the contrast agent followed by a distribution period where concentration of the contrast agent in the blood decreases. While the gold standard AIF is based on blood sampling during imaging and directly measuring the contrast agent in blood samples, this is frequently not possible.

Throughout the delivery of the contrast agent, a series of fast T_1-weighted images are acquired. Since the images are acquired while the contrast agent concentration is changing, the signal intensity also changes as the amount of contrast-induced relaxation effects are concentration dependent. The signal intensity rises fastest when the bolus of contrast agent in blood first reaches the tissue and extravasates and is followed by a slow washout period. The measured signal intensity (S) is based on the acquisition parameters (TE, TR, flip angle: α) and changes as the T_1 and T_2^* relaxation parameters change with the changing concentration of the contrast agent throughout data acquisition according to **Equation 2.12**.

$$S = S_0 \frac{e^{-\frac{TE}{T_2^*}}\left(1-e^{-\frac{TR}{T_1}}\right)\sin(\alpha)}{1-\cos(\alpha)e^{-\frac{TR}{T_1}}} \qquad \textbf{(Equation 2.12)}$$

Analysis of DCE data can either rely on non-parametric analysis or parametric analysis.[82] Nonparametric approaches are used most commonly clinically, because they do not rely on modeling, but rather on the rate of signal intensity rise or area under the curve approaches; however, these methods do not allow for quantitative measures of vascular parameters. Parametric measures require the signal intensity curve to first be converted to a concentration signal using **Equation 2.9**, which requires measurements of the intrinsic T_1 ($T_{1,0}$) and relaxivity of the contrast agent. The data is then fit to a pharmacokinetic model so that tissue parameters can be quantified.[83] The model is based on perfusion (F_p) and permeability (PS), which is determined by the rate of exchange of the contrast agent from the blood compartment (v_p) to the extracellular compartment (v_e).

The two-compartment exchange model is governed by **Equation 2.13**. Applying mass balances to both the extracellular and blood compartments shows how the plasma, extracellular, and arterial concentrations of the contrast agent (C_p, C_e, and C_a, respectively) change with time.

$$\frac{dC_p}{dt} = \frac{PS}{v_p}\left(C_e - C_p\right) + \frac{F_p}{v_p}\left(C_a - C_p\right)$$

$$\frac{dC_e}{dt} = \frac{PS}{v_e}\left(C_p - C_e\right)$$

$$C_t = v_p C_p + v_e C_e \qquad \textbf{(Equation 2.13)}$$

The total concentration of the contrast agent (C_t) is given by the sum between the extracellular and plasma compartments. An additional vascular exchange parameter (K^{trans}) is derived from the PS term according to **Equation 2.14**.

$$PS = \frac{K^{trans}}{1 - \frac{K^{trans}}{F_p}} \qquad \textbf{(Equation 2.14)}$$

While a variety of other models have been proposed and tested, they largely are based on making assumptions from the two-compartment exchange model.[82] Limitations of these approaches are assumptions about the distribution of the contrast agent in the compartments (well mixed) as well as fast exchange between compartments.

2.2.9 Magnetic Resonance Spectroscopy (MRS)

When placed in an external magnetic field, nuclei within a molecule experience a unique magnetic environment based on electron distributions and the presence of neighboring nuclei. The magnetic properties of nuclei (resonance frequency and relaxation parameters) depend on the chemical environment in which the nuclei are found. The resonance frequency of each nucleus is determined by the effective magnetic field, which is dependent on the chemical environment and the degree of electron shielding. Since different nuclei within a molecule experience different degrees of electron shielding from the external magnetic field (B_0), the effective magnetic field of each nucleus (B) is shown in **Equation 2.15** where σ is a shielding constant.

$$B = B_0(1 - \sigma) \qquad \textbf{(Equation 2.15)}$$

The effective magnetic field is more commonly defined by the chemical shift (δ) as given by **Equation 2.16** where ω is the resonance frequency of the nuclei and ω_{ref} is the resonance frequency of a reference compound and is reported in units of ppm.

$$\delta = \frac{\omega - \omega_{ref}}{\omega_{ref}} x10^6 \qquad \textbf{(Equation 2.16)}$$

When obtaining a spectrum, each of the nuclei within a molecule experience unique magnetic environments and frequencies where the sample has resonance will absorb more energy, leading to more RF energy being returned and resulting in peaks in the spectrum. Unlike in MRI, it is not the tissue water that is being measured, but rather the intensity and chemical shifts of protons of distinct metabolites. MRS is based on the differences in chemical shifts of different metabolites, resulting in excellent chemical specificity and allowing for the study of metabolism *in vivo*. The area under the peaks in a spectrum is proportional to the number of nuclei (i.e., concentration of a specific metabolite) and can be split into multiplets by the interaction of neighboring nuclei (scalar or J coupling). Most metabolites need to have a concentration of at least 0.5 mM (due to spatial and temporal resolution) for detection by MRS at 11.7T, but higher concentration (as well as larger volumes from which the signal is acquired) lead to both higher signal and sensitivity. Due to the lower concentration of metabolite signals, MRS necessitates a lower spatial resolution in comparison to MRI.

By far, ^{1}H MRS is most frequently used due to high natural abundance and high gyromagnetic ratio; however, MRS can be used with any nuclei that has a nuclear spin (e.g., ^{31}P, ^{23}Na, ^{19}F, ^{13}C, etc.) (**Table 2.1**). In ^{1}H MRS, the water signal is several orders of magnitude larger than the signal from metabolites that are trying to be detected, which necessitated technique development to suppress the water signal. Further, although the chemical shifts are based on the specific chemical environment of metabolites, many resonances overlap requiring methods such as using shift reagents, differences in relaxation/diffusion properties, frequency selective excitation, or scalar coupling to determine which metabolite corresponds to which peak. Although the integrated area under the resonance in an NMR spectrum is representative of metabolite concentration, it can be difficult to quantify due to contributions by difference in T_1 and T_2 weighting, diffusion, and exchange. To quantify the NMR signal, a reference standard must be used (internal references being preferred). Further, most biologic samples are inherently inhomogeneous and the NMR signal will not be the same throughout the sample. Further, multiple spatial localizations are possible (similar to how information from the signal can be encoded in space for MRI) by applying the RF pulse combined with phase encoding gradients in a technique termed magnetic resonance spectroscopic imaging (MRSI). Together, MRI and MRS are powerful tools for imaging and quantifying metabolites in tissues and can be adapted to imaging the tumor microenvironment.

2.3 Magnetic resonance (MR) methods to measure pH

pH-sensitive MR-based methods have been developed to measure areas of acidosis within tumors. In cancer imaging, pH dependent techniques are of critical importance because of the acidic environment and the relationship between acidosis and tumor invasion. pH has been associated with the ability of tumors to invade the basement membrane for both local tumor invasion and progression to metastatic disease.[84] Given the importance of pH_e in defining the tumor microenvironment, noninvasive imaging of pH_e is a potentially important biomarker of aggressive tumors and monitoring therapeutic response.

A variety of MR methods have been proposed and developed for measuring the pH; however, different methods are more sensitive to either measures of the intracellular pH (pH_i) or extracellular pH (pH_e). While a variety of relaxation and chemical exchange methods have been studied, MRS and spectroscopic imaging has had more success in quantitative pH measurements. MRS has decent spatial resolution, is sensitive and specific for measuring pH *in vivo*, and is generally based on chemical shift differences between pH dependent and pH independent resonances. Here, many of the MR methods used to measure pH are discussed, which also have been recently reviewed.[85,86]

2.3.1 Relaxivity

Intrinsic relaxation in MRI is not pH dependent. However, MRI relaxation-based methods to measure extracellular pH have been attempted using lanthanide-based contrast agents. Clinically used paramagnetic gadolinium agents (**Table 2.2**) provide contrast;[78] however, they do not by themselves provide pH or physiological information. Gadolinium is frequently used as a T_1 contrast agent in MRI as it is the most efficient lanthanide at having relaxation effects on bulk water, shortening the T_1 relaxation time and leading to increased signal intensity on T_1-weighted imaging. Using large Gd^{3+} complexes incorporating phosphonate groups, the relaxation effects of the contrast agent can be designed to be pH dependent. The most common chelate with pH sensitivity is 1,4,7,10-tetraazacyclododecane-1,4,7,10-tetrakis(acetamido-methylenephosphonic acid) (DOTA-4Amp^{8-}) which has shown promise. The pH dependence is due to the protonation of the pendant arms of the chelate, which results in changing effects on relaxation due to the proximity of water molecules to the paramagnetic metal. Therefore, by measuring the relaxation parameters, the pH can be determined.[87] The pK_a of phosphonates are in the physiological range and are therefore effective for being sensitive to small changes in physiological pH. Further, administered contrast agents tend to remain extracellular and therefore provide a readout primarily of pH_e.

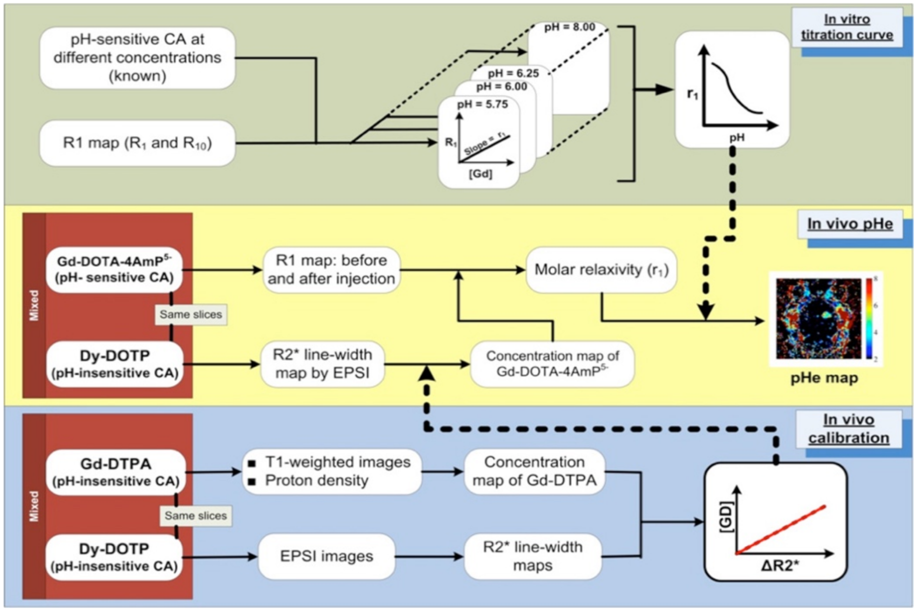

Figure 2.2. MRI protocol for relaxivity-based pH_e measurement. Calibration is performed to convert changes in T_2 relaxation to contrast agent concentration. The T_1 change using a pH-sensitive contrast agent is then calibrated using the concentration determined from the other agent. Using the calibration, *in vivo* pH_e maps are generated as demonstrated in a C6 rodent glioma model. Reproduced with permission.[88]

However, methods based on changes in relaxation are technically challenging because the relaxivity depends on other factors including the agent concentration, making quantification of pH very difficult as illustrated by **Figure 2.2**. Therefore, a second agent that is typically not pH responsive is required to act as a standard and an approach is used where one agent is used to determine the agent concentration and the other agent is used for the pH measurement.[88,89] Limitations of this approach include the administration of two contrast agents and assuming that the biodistribution of the two administered agents are the same. Further, the two agents must be administered serially as relaxation effects from each agent cannot be detected simultaneously from the same imaging voxel. Since the method is based on relaxivity changes to the water signal, the sensitivity is higher than other methods and allows pH_e mapping at high spatial resolutions comparable to standard anatomical MRI.

Instead of using two agents, other applications have utilized the pH dependent T_1 and T_2 contrasts from the same agent.[89] In this case, the pH independent measurement allows quantification of the contrast agent concentration, while the pH dependent measurement yields quantification of pH. Other methods have been proposed to account for the concentration dependence in the relaxivity measurement. Synthesizing Gd-DOTA-4 Amp derivatives that include a radiotracer (that may be detectable by PET) could be used for determination of concentration from a single molecule.[90] However, this requires access to combined MRI-PET technology which is not readily available.

2.3.2 CEST

Chemical exchange saturation transfer (CEST) MRI relies on exchangeable protons in certain molecular functional groups (-OH, -NH, $-NH_2$) in exchange with protons of surrounding water molecules. In CEST, a RF saturation pulse is applied at the resonance frequency of the exchangeable group, nulling the MR signal. As water protons exchange with this group, the water signal is reduced in a process that is pH dependent and depends on the exchange rate constant that is specific to each exchangeable group. The pK_a of the functional group will govern the rate of chemical exchange.

Therefore, this measurement relies on the presence of either endogenous or exogenous molecules that are CEST active. Diamagnetic agents (diaCEST) can be found naturally and include amino acids and sugars, as well as other organic molecules containing functional groups with exchangeable protons. Using endogenous contrast holds appeal because it does not require the administration of a contrast agent. The most common pH sensitive endogenous pool is found in amide groups and amide proton transfer (APT) has been used to measure pH.[91] However, since this method relies on amide groups found on amino acids and proteins, it tends to be weighted towards pH_i. Further, using a single CEST contrast is not enough to quantitatively measure pH as CEST contrast does depend on the concentration of the exchangeable protons. Exogenous diaCEST agents can also be administered with the most common being ipromide and iopamidol, which are commonly used contrast agents for other medical imaging modalities, and are pH sensitive.[92]

Paramagnetic agents (paraCEST) contain lanthanide metals and are based on the structure of the gadolinium-based contrast agents used clinically.[93-95] The benefit of the paraCEST agents is that the resonance frequency of the exchangeable protons are located far away from the water peak so there are no competing background effects that must be considered, leading to greater specificity in the measurements. Agents containing a variety of paramagnetic metals have been used for this application. ParaCEST agents either have an exchangeable proton group or use the exchange of water molecules near the paramagnetic core of the molecule for CEST contrast. In all cases, the agents are designed so that the exchange rate is pH sensitive. However, due to the large chemical shift dispersion of the exchangeable proton groups, high B_1 fields are required for saturation and limit their translation due to tissue heating concerns.

When there are multiple exchange sites, either on the same molecule or in a combination of two molecules, a ratiometric approach can be utilized to eliminate the concentration-dependent nature of the pH measurement. A ratiometric approach has been used with amine and amide proton exchange in a method termed amine/amide concentration independent detection (AACID) that eliminates the need for quantifying the contrast agent concentration and allows quantitative pH mapping.[96] diaCEST methods using endogenous contrast is difficult to interpret because it is dependent on amino acid/protein concentration, which can change in different tissue types and in comparing healthy tissue to disease states. However, diaCEST methods have promise for clinical translation because they do not require the administration of contrast agents, have low saturation power requirements, and are based on readily implementable pulse sequences that are available on clinical scanners. Therefore, amine and amide proton transfer has been studied on endogenous pools in glioblastoma and has shown contrast compared to surrounding healthy tissue; however, absolute pH quantification from these methods remains challenging. Another concern with exogenous diaCEST agents is the necessity for large concentrations of the CEST agent (>30 mM) at clinical magnetic field strengths, which may in itself alter the pH being measured and is not practical for clinical applications. The CEST effect in diaCEST experiments are also impacted by a variety of other factors including temperature, concentrations of ions, and perfusion. Direct saturation of the water resonance as well as overlap with magnetization transfer from macromolecules also impacts the interpretability of the measurements. Applications of CEST with both amide groups[97] and amine groups on amino acids[98] have been used to measure the pH in tumors, including GBM. Recent developments with CEST[99] and amide proton transfer (APT)[100] have also been used as potential biomarkers of tumor proliferation.

2.3.3 MRS

^{31}P, ^{19}F, and ^{1}H MRS has been used to detect both endogenous and exogenous compounds which are generally representative of the intracellular and extracellular pH, respectively. The compounds used have high pH sensitivity, are metabolically stable, have a high signal to noise ratio (SNR) with reasonable imaging times, and are non-toxic.

^{31}P MRS can be used for pH determination since phosphorus is abundant, has a high sensitivity, and there are many phosphorylated metabolites that can be detected whose resonances are pH dependent. ^{31}P MRS was one of the first MR techniques applied for measuring pH. Specifically, the most easily detected metabolites are P_i, PCr, and ATP and the intracellular pH can be measured because the difference in chemical shifts between PCr and P_i is pH dependent.[101] However, for measures of pH_e, exogenous agents such as 3-aminopropyl phosphonates (3-APP) are required.[75] 3-APP has a pH dependent chemical shift and since the agent remains extracellular, reports on pH_e. Together, these methods have allowed for quantification of the pH gradient (pH_i-pH_e).

^{19}F MRS can also be used for direct detection of ^{19}F containing exogenous MR probes. ^{19}F MRS is promising due to the 100% natural abundance of ^{19}F and little to none endogenous

^{19}F background signal. These properties result in specific detection and relatively high SNR allowing pH measurement with higher sensitivity and less compartment artifacts than ^{31}P MRS. Exogenous fluorinated vitamin B6 derivatives are commonly used as pH probes and interestingly, these compounds insert into cell membranes and are able to report on both the intracellular and extracellular environments, allowing the intracellular-extracellular pH gradient to be determined.[102] Other fluoroaniline sulfonamide agents have been used for pH_e measurement where the chemical shifts of the ^{19}F resonances are pH dependent.[103] Like other MRS techniques, the sensitivity is low and requires delivery of a sufficient concentration of the agent to the tumor (mM range). These agents do not have specific uptake in tumors, requiring larger doses of the administered agent and suffer from some of the agents not being stable under physiological conditions. Further, MRS with any non-^{1}H nuclei, requires specialized equipment that is not always readily available.

^{1}H MRS is the most commonly used MRS isotope and is useful because of its higher sensitivity, improved spatial resolution and shorter imaging times and is available in most MR scanners for readily available implementation. ^{1}H has a very high natural abundance and is found in high concentrations in the physiological environment, primarily in water and fat but also in nearly all metabolites. Many of these metabolites are present in the mM concentration necessary for detection and can be detected directly. However, no detectable endogenous ^{1}H MRS signal is inherently pH sensitive. Although *in vivo* measures of histidine have been attempted due to the presence of multiple pH sensitive resonances, concentrations are too low for accurate pH quantification requiring supplementing the signal with administered histidine, which complicates the measurement as the pH measured is an average of pH_e and pH_i.[104] Therefore, pH measurements with ^{1}H MRS requires exogenous imidazoles to be used as pH probes.[105] Other agents such as 2-imiadazole-1-yl-3-ethoxycarbonyl propionic acid (IEPA) have a pH sensitive resonance that does not overlap with endogenous signals, localizes in the extracellular space, can be detected with ^{1}H MRS and provides a measure of pH_e.[106]

Hyperpolarized ^{13}C MRS has also been used for pH measurements using a variety of different administered substrates.[107-109] Dynamic nuclear polarization involves changing the distribution of magnetic spins so that there is a greater difference in spins between two states, increasing the sensitivity of NMR. This has most commonly been done with ^{13}C by using microwave irradiation to transfer magnetization from electrons to adjacent nuclei at extremely low temperatures (1-4 K). Although hyperpolarization can lead to several orders of magnitude increase in sensitivity, the hyperpolarization is quickly lost at higher temperatures with T_1 relaxation times of less than 1 min. Therefore, the hyperpolarizer must be located immediately adjacent to the MR scanner and must be administered immediately after being formed, and then imaged immediately after being injected. Even under ideal circumstances, the timing of these events means that the actual sensitivity gain in the actual scan is much lower. A variety of substrates have been used including ^{13}C-labeled zuymonic acid, bicarbonate, or lactate. These measures again tend to be a weighted average of pH_e and pH_i as the substrates can freely cross cell membranes.

2.3.4 BIRDS

An expansion and more recent application of an MRSI technique is Biosensor Imaging of Redundant Deviation in Shifts (BIRDS), which exploits the pH-dependent chemical shifts of the non-exchangeable protons on lanthanide chelates. Instead of using relaxivity differences (which are inherently concentration dependent), this technique expands the use of lanthanide contrast agents, similar to those used for enhancing MRI contrast, by using MRS and chemical shift imaging to directly measure the chemical shifts emanating from protons on the contrast agent itself. Because the pH dependence is based on the chemical shift (and not relaxivity), the pH readout is not concentration dependent. Thulium (Tm^{3+}) based agents have the highest pH sensitivity and are therefore frequently used because they can give pH readouts with lower concentrations of the agent.[110] Additionally, by modifying the chelate to include an amino group, the contrast agent can have both CEST and BIRDS properties, allowing added redundancy for measuring pH.[111,112] The BIRDS methodology is discussed in much greater detail in Chapter 3.

2.4 Other pH imaging methods

In addition to the MRI/MRS based methods for measuring pH, it should be mentioned that a variety of other techniques have been utilized for imaging acidosis in cancer.

2.4.1 Direct electrode recordings

pH electrodes work by using a H^+-selective glass electrode to measure the concentration of H^+ ions and convert into a pH value on a logarithmic scale. pH electrodes can be inserted directly into tumors to measure the pH; however, this is a highly invasive procedure and each recording involves a new insertion requiring many recordings to spatially map pH. Although these may be considered the gold standard because it can be externally calibrated using solutions of known pH, likely these measurements are a weighted average of the intracellular and extracellular environment as they rupture the cells upon insertion. Due to the need to directly insert the electrode, tumors just under the skin are the most suitable to this kind of approach and has been applied in the study of melanoma.

2.4.2 Optical imaging methods

Optical imaging methods are based on using pH dependent fluorescent molecules which can be detected using microscopy methods. Optical methods allow for rapid measurement with high temporal resolution and very high spatial resolution. However, the optical methods are usually limited in their FOV such that only part of the tumor or surrounding tissue can be imaged at a time and have very poor depth penetration such that only excised tissue or surface tumors right under the skin can be studied.

There are a variety of optical imaging probes that are responsive to pH. For example, pHLIP proteins insert into cellular membranes only at low pH (normally <6.5).[113,114] Therefore, these proteins can be targeted to solid tumors where the pH is low. The pHLIP proteins are fluorescent and with fluorescent imaging, regions of low pH can be identified; however, these methods typically do not result in quantitative pH values, but only demonstrate if the pH is below a threshold value which is dependent on the properties of the pHLIP protein. In another optical technique termed fluorescence ratio imaging microscopy (FRIM), a single fluorophore is detected at two different emission wavelengths, such that the concentration of the fluorophore is not needed for quantification. the pH is determined by measuring the fluorescence at two different wavelengths. This normalizes for the concentration of the fluorophore as well as differences in the acquisition parameters (such as intensity). In a similar approach, semi-napthorhodafluorescin-1 (SNARF-1) can be used due to its pH dependent emission spectra and by measuring fluorescence at two different wavelengths can yield concentration-independent pH measurements.[6]

Some limitations of these methods are the autofluorescence of tissues and quenching of the fluorescent signal in deeper tissues. Further, fluorescent probes need to have pK_a values in the physiological range, which can be challenging as many of them have maximum pH sensitivities at much higher pH values. Benefits include that they are less invasive than pH electrodes, provide high spatial resolution of pH mapping, can be optimized to measure the pH_e or pH_i depending on the fluorophore chosen, and are very sensitive such that only very low concentrations of the fluorophore are needed for detection.

2.4.3 Positron emission tomography

Positron emission tomography (PET) relies on the administration of small doses of radioactive isotopes (radiotracers) conjugated to molecules designed to target specific physiological targets in the body and is used as a molecular imaging tool.[115] The radioactivity is localized using the decay properties of the radiotracer and regions of radiotracer accumulation are identified. PET is performed routinely clinically using the ^{18}F-fluorodeoxyglucose (^{18}FDG) tracer, which detects upregulation of glucose uptake as a proxy for increased glycolytic metabolism, in cancer.[116] Although PET is very sensitive, allowing detection of small amounts (nM) of the radiotracer, PET has lower spatial resolution, on the order of 2-3 mm clinically, due to the nature of the detected signal.

pH sensitive PET tracers have also been developed. Although initial attempts using the pH-dependent ionization of radiotracers were unable to detect acidification in tumors,[117] current approaches involve radiotracers that have been conjugated to pH low insertion peptides (pHLIP) similar to those use for the optical methods described previously. Detection of these proteins that insert into the cell membranes in a pH-dependent manner have been successfully used to identify acidosis in tumors.[114,118,119] However, due to the sigmoidal nature of peptide insertion, these methods are generally non-quantitative and can only be used to determine if the pH is below a threshold value similar to their optical counterparts. Recently, ^{18}FDG has been synthesized to be in a molecular "cage" using a glycosylamine linkage that is released in a pH-sensitive manner under acidic conditions,[120] demonstrating acidic conditions in tumors which can be increased through systemic bicarbonate administration. While promising, the PET methods are unable to provide absolute quantification of pH and suffer from lower spatial resolution, making studying pH gradients in tumors challenging.

2.5 Applications to cancer imaging

In cancer imaging, these methods have repeatedly demonstrated that pH_e is acidic, with a corresponding alkalinization of pH_i, in many tumor types and can be spatially heterogeneous. The pH gradient between the intratumoral and peritumoral environment can be used as a marker of tumor invasion into surrounding tissue as more invasive tumors have acidic pH that spreads beyond the tumor boundary. Further, through the combination of different imaging methods, pH_e can be compared to aid in the confidence of the measurements as well as compare to other measures that are expected in acidic environments, such as a correlation with increased lactate levels from ^{1}H MRS. However, each imaging modality comes with differences in the spatial resolution achievable, the need for the administration of exogenous agents, and the ability of the method to yield a quantitative pH value.

Chapter 3: Methodological descriptions of BIRDS for molecular imaging of pH and temperature

3.1 Abstract

Biosensor Imaging of Redundant Deviation in Shifts (BIRDS) is a magnetic resonance spectroscopic imaging (MRSI) technique that relies on the temperature and pH-dependent chemical shifts of non-exchangeable protons on lanthanide-containing paramagnetic contrast agents. pH and temperature are physiologically relevant parameters with many medical applications. As discussed in Chapters 1 and 2, an acidic extracellular space is a hallmark of the tumor microenvironment, where acidosis has been postulated to promote the aggressive and invasive characteristics of tumors and also inhibit the therapeutic response. Therapeutic hypothermia has applications in cerebral ischemia and traumatic brain injury (TBI) where temperature measurements are needed to evaluate efficacy of neuroprotective procedures. Therefore, an imaging method such as BIRDS that allows for quantitative and spatial pH and temperature mapping is highly desirable.

Here we describe the development and implementation of BIRDS in the context of evaluating the acidic pH_e in glioblastoma models in rodents in small-bore 11.7T clinical scanners, where acidic pH_e represents tumor invasion in untreated tumors. Since there are no other tomographic pH_e mapping methods and directly altering pH_e is difficult to implement, we looked to assess the quantitative BIRDS-based temperature readout, which could be compared against direct temperature recordings, in a hypothermia model because temperature is much more easily altered than is pH. Selective brain cooling using an innovative cerebrospinal fluid (CSF) cooling platform was used to induce hypothermia in the

brain. Temperature mapping of healthy sheep brain in wide-bore 7.0T clinical scanners provided dynamic temperature measurements from the whole brain. The brain temperature decreased significantly with cooling over all defined brain regions to levels known to be neuroprotective, while maintaining systemic normothermia, and was in agreement with thermocouple measurements. Rapid and synchronized temperature fall/rise upon cooling onset/offset was observed reproducibly such that dynamic thermal mapping can provide high spatiotemporal temperature measurements to aid in optimizing selective neuroprotective protocols. All temperature mapping work in this chapter has been previously published and is used with permission.[121]

3.2 Introduction to BIRDS

An acidic microenvironment is a hallmark of most solid tumors due to a metabolic shift towards glycolysis even in the presence of oxygen (Warburg effect) and immature vasculature that does not permit the clearance of waste products.[41] The reduced extracellular pH (pH_e) has been associated with promoting tumor cell proliferation and promoting angiogenesis and invasion[5,122-124] as well as creating an immunosuppressive environment.[33,125] Further, the low pH_e leads to a poor response to many therapies,[7] and neutralization of pH_e has been proposed as an effective therapeutic strategy.[126,127] Given the important contribution of extracellular acidosis to shaping the tumor microenvironment, it would be desirable to be able to quantitatively and spatially map pH_e for evaluating the metabolic state of the tumor and how metabolism changes during tumor growth and response to therapy.

Here we describe a magnetic resonance spectroscopic imaging (MRSI) technique termed Biosensor Imaging of Redundant Deviation in Shifts (BIRDS) which exploits the pH and temperature based dependent chemical shifts of non-exchangeable protons on lanthanide-based contrast agents for quantitative pH (and temperature) measurements.

While there are other methods that have been developed for organ-wide absolute pH tomographical measurement, there are several assumptions of which to be aware when comparing pH readouts across different modalities as discussed in Chapter 2. First, some methods are weighted more towards extracellular pH, while others are weighted more towards intracellular pH. ^{31}P magnetic resonance spectroscopy (MRS) is the gold standard for quantitative pH measurement; however, this method is heavily weighted towards intracellular pH because the readout is dependent on inorganic phosphate and phosphocreatine.[75,128] Further, the reduced sensitivity of ^{31}P necessitates large imaging volumes, decreasing the spatial resolution achievable. Many magnetic resonance imaging (MRI) methods are available for pH readout. A variety of chemical exchange saturation transfer (CEST) techniques have also been proposed for quantitative pH mapping.[91,129-131] The CEST readout exploits the MRI detectable exchange between protons in dilute pools (of hydroxyl, amide, or amine protons in various endogenous or exogenous molecules, both small and large) and bulk water. However, the diamagnetic CEST contrast using endogenous exchangeable pools is heavily influenced by protein concentration and a variety of other physiological factors making quantification difficult. Additionally, many of these methods rely on knowledge of the contrast agent concentration for pH quantification, which is difficult to measure in *in vivo* applications. There are also paramagnetic CEST agents that can provide simultaneous temperature and pH measurements.[132] Finally, there has been success using

MRS detection of hyperpolarized ^{13}C substrates (e.g., lactate, bicarbonate) that have led to quantitative extracellular pH measurements. But caution must be used with hyperpolarized ^{13}C MRS since these small molecules easily cross cell membranes.

However, BIRDS is a unique method that achieves higher spatial resolution pH measurements by exploiting the higher sensitivity of ^{1}H MRI with the specificity of ^{1}H MRS. As explained below, due to several unusual features of BIRDS agents, the ^{1}H MRSI data acquisition is acquired at ultra-high speed but with little compromise of MRI-like spatial voxel sizes.

Contrast agents used for BIRDS are based on the macrocyclic structure used in commercially available gadolinium-based contrast agents. The pendant arms of these molecules can be optimized to allow for greater specificity in measuring the physiological parameter of interest (e.g., pH or temperature). For example, the contrast agent $TmDOTMA^{-}$ is a carboxylate that only exhibits temperature dependence, whereas $TmDOTP^{5-}$ is a phosphonate that gives pH sensitivity (in addition to temperature). While many paramagnetic metal ions can be complexed to the different chelates, Tm^{3+} containing compounds have shown the largest hyperfine shifts of their ^{1}H resonances, which provide higher specificity for temperature and pH readouts.

Additionally, since BIRDS specifically detects the proton resonances and the chemical shift is the measured property, as opposed to their effects on water relaxation, the BIRDS readout of pH is concentration-independent. The hyperfine shifted resonances of the detected resonances are diverted far from water (-140ppm, 60ppm, and 80ppm in $TmDOTP^{5-}$) so that there is no overlap with any intrinsic metabolites, increasing the specificity of the measurement. Further, due to the presence of multiple detected proton resonances that shift in different directions with changing pH and temperature, the measurement is redundant and allows for simultaneous quantification of both pH and temperature.

The chemical shift of each chelate proton resonance depends on the spatial location of that proton in relaxation to the paramagnetic ion, which also affects the temperature and pH dependencies of each proton resonance. Protons that are closer in proximity to the paramagnetic ion will have resonances that are farther shifted away from the water peak due to changes in the effective magnetic field experienced. *In vitro* calibrations of the pH and temperature dependence of the chemical shifts are conducted under a variety of conditions to demonstrate the reliability of the pH calibration that is applied *in vivo*. The method also allows for complete three-dimensional acquisition over the entire tissue or organ of interest because of the extremely shortened relaxation times of these resonances,[133] and since the contrast agents remain extracellular, the measurements are weighted towards the extracellular compartment.[134]

Due to the presence of the paramagnetic metal, both the longitudinal (T_1) and transverse (T_2) relaxation times are extremely short (<5ms) allowing for fast averaging and insensitivity to shim and magnetic field inhomogeneities. Moreover, because the $\sqrt{(T_2/T_1)}$ of the BIRDS readout is high, the measurement is quite stable across magnetic field strengths. The paramagnetic nature of these agents also provides T_2 contrast that can be used for relaxation-weighted MRI and some versions of these molecules include exchangeable protons which can also be used for paramagnetic CEST applications.[132]

BIRDS is limited by the signal to noise ratio (SNR) such that a sufficient concentration of the agent (>1mM) must accumulate in the tissue of interest for adequate sensitivity to accurately make the pH or temperature measurement. In tumors, leaky vasculature allows the agent to accumulate to a sufficient degree; however surrounding tissue may have low agent concentrations. The concentration of the contrast agent can be increased by reducing the clearance of the agent through surgical or pharmacologic renal inhibition. For applications involving novel contrast agents and advanced imaging methods, animal models must be used. To pre-clinically evaluate BIRDS, orthotopic xenograft models of glioblastoma (GBM) are beneficial because they resemble human tumors and allow for the invasion of the tumor into the surrounding tissue. A variety of tumor models[22,25] have been used in this regard including the 9L and RG2 models that are used in immunocompetent Fisher rats as well as the human-derived U87 and U251 models in Athymic/Nude rats. With this background of the rational for BIRDS pH_e and temperature mapping, the methodology and technicalities will be discussed for performing BIRDS on preclinical tumor models. The methods will reflect the *in vitro* calibration of BIRDS and its application to the *in vivo* measurement of pH_e in the tumor microenvironment. BIRDS was also further developed into a longitudinal pH_e mapping platform to allow for evaluation in changes in the metabolic features of the tumor microenvironment during tumor progression. While all initial development of BIRDS was performed on animals with renal ligation to increase the concentration of agent in the surrounding tissue, longitudinal measurements using BIRDS can be achieved by temporarily inhibiting renal clearance using probenecid.[135]

Since there are no other tomographic pH_e mapping methods to compare with BIRDS-readout of pH_e and directly altering pH_e at a systemic or local level is difficult to implement, we evaluate BIRDS temperature mapping because temperature is much more easily altered using cooling methods and can be compared against direct temperature electrode recordings. We then demonstrate the BIRDS method in a hypothermia model in sheep. While although a different application, these measurements demonstrate the dynamic and sensitive nature of the temperature measurements and their accuracy against previously recorded temperature measurements in the same model system.

3.3 Methods for tumor pH_e mapping

3.3.1 Characterization of temperature and pH sensitivity in BIRDS

A database of thulium (III) 1,4,7,10-tetraazacyclododecane-1,4,7,10-tetra(methylenephosphonate) ($TmDOTP^{5-}$; Macrocyclics) samples are needed to construct the pH and temperature calibration curves *in vitro* which can then be applied for *in vivo* analysis. The characterization is performed at various temperatures and pH values. All data were acquired on a 11.7T (500 MHz) vertical bore magnet (Bruker) with temperature control. Samples of 10 mM $TmDOTP^{5-}$ in DI H_2O were prepared in NMR tubes (Wilmad Lab Glass). To each sample, 10% by volume deuterium oxide (D_2O; Sigma) was added along with 3 mM trimethylsilylpropanoic acid (TSP; Sigma) as a chemical shift standard. Seven samples were prepared over the physiological pH range (6-8). The pH of each sample was measured using a pH meter and the pH of each sample was adjusted using small volumes of dilute Hydrochloric acid (HCl; Sigma) or Sodium hydroxide (NaOH; Sigma). For each pH value, data were acquired over a range of temperatures (30-40 °C).

Spectra for each sample were acquired, line broadened (50 Hz) and baseline and phase corrected. The chemical shift of each proton resonance (H2, H3, H6) was measured (**Figure 3.1**). Chemical shift data for each proton resonance were plotted in 3D against both temperature and pH and the temperature and pH sensitivity were then quantified by fitting the data to a 2nd order polynomial. The calibration is based on the difference in chemical shifts between sets of proton resonances.[134] For the best accuracy, the average of temperature and pH calibrations from two sets of proton resonances are used as shown in **Equation 3.1** and **Equation 3.2**. The difference in the H2 and H6 chemical shifts (x=H2, y=H6 in the following equations) and the difference in the H3 and H6 (x=H3, y=H6) chemical shifts are used for calibration where the constants a_i and b_i are from a multi-parametric non-linear least squares fit.

$$T^{[x,y]} = a_1^{[x,y]} + a_2^{[x,y]}\delta_x + a_3^{[x,y]}\delta_y + a_4^{[x,y]}\delta_x^2 + a_5^{[x,y]}\delta_y^2 + a_6^{[x,y]}\delta_x\delta_y \quad (\textbf{Equation 3.1})$$

$$pH^{[x,y]} = b_1^{[x,y]} + b_2^{[x,y]}\delta_x + b_3^{[x,y]}\delta_y + b_4^{[x,y]}\delta_x^2 + b_5^{[x,y]}\delta_y^2 + b_6^{[x,y]}\delta_x\delta_y \quad (\textbf{Equation 3.2})$$

The pH and temperature dependencies of $TmDOTP^{5-}$ that are used in the calibration for *in vivo* experiments are shown in **Figure 3.1**.

To account for the impact of other ions or proteins in the blood on the chemical shift, the calibration is also validated in the presence of different physiological concentrations of ions (Na^+, K^+, etc.) and in the presence of proteins (BSA, blood, etc.). Similar samples were prepared by varying the concentration of different ionic salts by adding sodium chloride (NaCl; Sigma), potassium chloride (KCl; Sigma) or calcium chloride ($CaCl_2$; Sigma). The ionic concentrations were varied over the physiologic range with Na^+ (130-150 mM), K^+ (5-10 mM), and Ca^{2+} (0-4 mM). For completeness, the calibration can be repeated by dissolving $TmDOTP^{5-}$ in PBS, 4% BSA, or blood plasma. While Na^+ and K^+ concentrations were not found to influence the chemical shifts or the resulting calibration, Ca^{2+} does have an effect.

Since Ca^{2+} does influence the chemical shifts, an *in vivo* concentration for Ca^{2+} is assumed to be 1 mM for applications of the calibration.[134] Using the calibration curve yields spatial pH maps *in vivo* that are representative of the extracellular pH (pH_e) as the contrast agent does not cross the cell membrane and therefore only reports on the extracellular environment. However, in the brain, the agent is located in interstitial, vascular, and CSF spaces and the pH reported will be a volume-weighted average of the pH in the voxel. Different contrast agents can be used with the BIRDS method, such as $TmDOTMA^-$, which only has chemical shift sensitivity to changing temperature.[136] However, any reporter molecule requires the same extensive characterization, calibration, and validation before use, but the general method is adaptable to a variety of chemical moieties that each have different reporter properties.

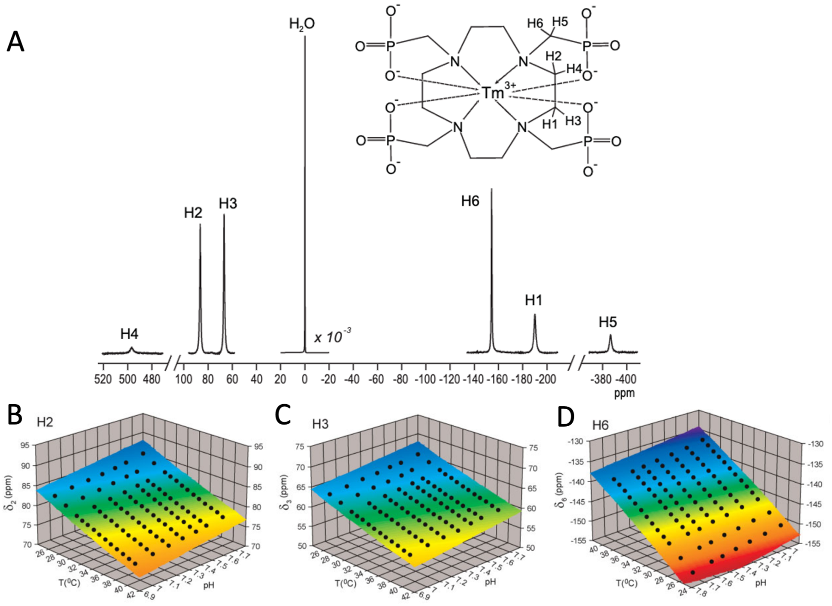

Figure 3.1. *In vitro* characterization of $TmDOTP^{5-}$ for temperature and pH_e measurements. Chemical structure and NMR spectrum of 10 mM $TmDOTP^{5-}$ acquired at 11.7 T (A). Temperature and pH dependence of the H2 (B), H3 (C), and H6 (D) proton chemical shifts. The sample contained 4 mM $TmDOTP^{5-}$ with 1 mM $CaCl_2$ and 3 mM TSP for reference. The 3D plots show the best fit of the chemical shifts for each proton resonance as a function of pH and temperature. Reproduced with permission.[134]

3.3.2 Animal preparation for in vivo tumor studies

Most solid tumors maintain an acidic pH_e; however, the degree of acidosis can vary based on primary tumor site and type.[133,137] Here a glioblastoma (GBM) model is used as a representative tumor. Although GBMs in the brain come with a variety of limitations regarding access, tumor size monitoring, and drug delivery due to the presence of the blood-brain barrier, the benefit is that the head is not prone to respiratory or other motion, eliminating this concern from the imaging experiments. Another consideration is the growth characteristics of the tumor. Tumors that are highly infiltrative before forming a mass may lead to symptom development prior to a large tumor developing. Less infiltrative tumors, although less representative, provide the benefit of becoming larger allowing better contrast agent or drug delivery. U87 and U251 are both human-derived GBM cell lines that can be intracranially injected in athymic mice or rats. Both of these tumor types result in a disrupted blood brain barrier, which allows contrast agents/drugs to pass into the tumor. However, for any sort of longitudinal scanning, the tumors may have to be initially imaged when the tumors are smaller.

The following procedures are used for generating U87 or U251 tumor xenografts in the brain of athymic/nude rats. Note that a variety of different cell lines (e.g., 9L, RG2, etc.) as well as patient derived xenografts (PDX) have been reported in the literature and can be used with cell-specific culture and injection protocols in both mice and rats.[22] All animal protocols and procedures are approved by the Yale University Animal Care and Use Committee. Animals are maintained in an animal facility maintained by the Yale Animal Resources Center.

U87 and U251 cells were acquired from the American Type Culture Collection (ATCC). Cells are maintained in T75 flasks containing culture media supplemented with 10% fetal bovine serum (FBS) and 100 units/mL penicillin and 100 μg/mL streptomycin. U87 cells are maintained in 10 mL of supplemented high-glucose (4.5 g/L) Dulbecco's modified eagle medium (DMEM), while U251 cells are maintained in 15mL low-glucose DMEM (Gibco). All cells are maintained in an incubator at 37 °C and 5% CO2 atmosphere.

On day of intracranial injection, U87 or U251 cells are harvested from culture at high confluence (>70%). Cells are resuspended in serum-free DMEM at a concentration of 40,000 cells/μL for U87 and 100,000 cells/ μL for after a manual cell count using a hemocytometer. A total of 5 μL of the cell suspension is loaded into a 10 μL syringe (Hamilton) connected to a 26G beveled needle, which is used with a microinjector (Micro4, World Precision Instruments) system.

Athymic/ nude rats (Envigo) are anesthetized with isoflurane (2-3%) and provided appropriate pre-emptive analgesia (buprenorphine, 0.05 mg/kg). The animal head is shaved, sanitized using washed of betadine and 70% ethanol, and positioned in a stereotactic holder (Kopf Instruments). The scalp is opened by making a 2-3 cm incision using a scalpel and then using two pairs of hemostats to hold the skin back to expose the skull where the bregma is visually identified. A drill is positioned directly over the bregma and then moved 3 mm to the right. The drill is turned on and lowered until the tip of the drill just penetrates through the skull, before being turned off and raised. The needle and microinjector syringe containing the cell suspension is positioned over the burr hole. The needle is lowered 3.5 mm into the cortex and then raised 0.5 mm. The 5 μL cell suspension is then injected at a rate of 1 μL/min after which the needle is left in place for 5 min before slowing withdrawing the needle (0.5

mm/min). The burr hole is then sealed with bone wax, the incision is closed with sutures, and the incision site is sanitized. The animal is removed from the stereotactic holder and placed in a clean cage on a heating pad until the animal recovers from anesthesia. Post-surgical analgesia (carprofen, 5 mg/kg and buprenorphine 0.05 mg/kg) is continued for 48 hours. The animal is monitored daily for changes in body weight or any signs of neurological symptoms.

3.3.3 Animal setup for magnetic resonance imaging/spectroscopy experiments

The animal is anesthetized with 2-3% isoflurane in O_2 in an induction chamber prior to transferring the animal to a heating pad on the bench. Since the imaging procedures require the intravenous administration of contrast agents, a tail vein catheterization is performed. A needle attached to PE10 (Braintree Scientific) line filled with heparinized saline is inserted into the lateral tail vein (either right or left) and secured to the tail with tape. The functionality of the infusion line is verified by drawing blood back into the line and confirm that there is no resistance when pushing ~100 μL of heparinized saline.

The animal is then placed on a custom-made rat holder with a nose cone that allows for gas (1.5% isoflurane anesthesia) delivery. The head is centered, making sure that it is relaxed and flat, and held in place with small foam pieces to prevent animal motion during the imaging scan. Ointment is applied to the animal's eyes to prevent drying. After positioning the animal in the animal holder, the animal is positioned under a 1.5cm diameter RF surface coil.

Animal monitoring during the experiment is important since in small bore animal MR scanners, the animal is not visible during the experiment. In particular, respiratory monitoring is essential to monitoring depth of isoflurane anesthesia. Respiratory monitoring is conducted by placing a pneumatic pillow under the chest of the animal, which is integrated with animal monitoring software (Small Animal Instruments). For sufficient anesthesia throughout the experiment, the respiratory rate should be maintained between 30-60 breaths per minute.

Additionally, maintaining animal body temperature is also vital. Animals under anesthesia naturally have a decrease in core body temperature that may result in delayed recovery after a survival experiment or possibly even death. Warm water is circulated from a water bath, maintained at 44-48 °C, through a warming pad that is placed on top of the animal to maintain body temperature around 37 °C. For athymic rats (or other animals without fur), a paper towel should be placed between the animal and the heating pad so as to prevent burns on the skin. The temperature is monitored using a rectal optical thermocouple probe.

3.3.4 Contrast Agent Preparation

Prior to the start of imaging, the contrast agents used for BIRDS, such as $TmDOTP^{5-}$, are prepared. However, these agents are cleared by the kidney relatively quickly, similar to the clinically used gadolinium contrast agents.[78] To increase the circulation time of the agents, renal clearance needs to be decreased. In terminal experiments, this can be done directly by renal ligation, resulting in near zero clearance of the agent throughout the duration of the experiment. However, for experiments necessitating longitudinal imaging, a nonsurgical approach must be used. This can be achieved by using probenecid, an organic anion transporter inhibitor, which is used to temporarily pharmacologically inhibit the renal clearance of the agent.[138-140] We find that a predose of the probenecid prior to the start of the contrast agent infusion along with an additional coinfusion while administering the agent leads to the greatest increase in agent concentration.[135] Note that the concentration of the agent within the contrast-enhancing region of the tumor is largely unaffected by these strategies as the blood brain barrier is compromised within the tumor and the agent is delivered to the tumor even without renal inhibition. However, the contrast agent in the brain is greatly reduced without methods to decrease renal clearance.

A stock solution of probenecid (Sigma) is prepared at a concentration of 100 mg/mL by dissolving probenecid in 0.5 M NaOH. The pH of the solution is measured using a pH meter, and then adjusted down to 7.4 by the addition of saturated KH_2PO_4 (Sigma). A single dose (1.5 mL) of $TmDOTP^{5-}$ (Macrocyclics) is prepared fresh before each experiment based on the individual animal weight (1 mmol/kg). The volume of the dose, as opposed to the concentration, is fixed during preparation since the infusion is planned for a set amount of time. The amount of $TmDOTP^{5-}$ needed is the animal weight in kg multiplied by the molecular weight of $TmDOTP^{5-}$ (914.2 g/mol). To this solution, 100 mg/kg probenecid is added (using the probenecid stock solution the volume added in μL is equal to the animal weight in grams). The volume of the solution is then brought up to 1.5 mL and is vortexed until there are no signs of any particulate in the solution.

To perform the contrast agent infusion during imaging, a PE10 line that has been flushed with saline from a syringe pump is run to the bore of the magnet and connected to the tail vein catheter. First, a 100 mg/kg predose of probenecid is infused over 10 min with the rate set by the infusion volume. For example, if 250 μL of probenecid solution needs to be infused, the syringe pump rate is set at 25 μL/min. At the end of the infusion, the infusion line is disconnected from the tail vein catheter and flushed with saline. After a 20 min waiting period to allow the probenecid to take effect, the infusion of the $TmDOTP^{5-}$ and probenecid solution is begun at a rate of 15 μL/min for a total infusion time of 100 min. The initial infusion of $TmDOTP^{5-}$ must be performed slowly to monitor animal physiology; however, after an initial period (usually ~30 min), the injection can be sped up in order to reduce the infusion time. The rate of infusion should be decreased if any changes in animal physiology (respiratory rate) is observed; however, an increase in the respiratory rate is usually seen during the beginning of agent infusion.

3.3.5 MRI and BIRDS Acquisition

All data is acquired on a high-field, horizontal-bore small animal MRI scanner. All experiments were either performed on an 11.7T Bruker scanner (21cm bore size, amplifier with peak power of 500 W, and gradient system with 400 mT/m maximum amplitude, 150 μs rise time) or a 9.4 T Bruker scanner (16cm bore size, amplifier with peak power of 500 W, and gradient system with 500 mT/m maximum amplitude, 180 us rise time). An RF coil setup is required for acquiring MR and BIRDS data. A small (1.5cm) single loop surface coil tuned to 500 MHz (^{1}H resonant frequency at 11.7 T) is used for BIRDS experiments. The surface coil diameter must be large enough to allow coverage of the entire tissue of interest (e.g., brain); however, the diameter must be kept small enough to allow efficient RF power transfer yielding high SNR.

The animal holder and RF coil are slid into the magnet bore and the animal is positioned in a straight position in the isocenter. All details provided are for a Bruker scanner running ParaVision 5 or higher. Prior to the start of imaging, the RF coil is tuned and matched to the acquisition frequency. A fast low angle shot (FLASH) sequence is performed to obtain scout images in three perpendicular imaging planes to serve as a fast localizer scan to position the animal in the center of the imaging field of view (FOV). Next a rapid acquisition with relaxation enhancement (RARE) sequence is performed where the power, shim, frequency offset, and receiver gain are optimized using automated setup features in Paravision. A point resolved spectroscopy (PRESS) sequence is used for second-order shimming over an ellipsoid ROI using the B_0 map and the MapShim feature in Paravision. Once all setup is complete, the imaging experiments can begin and can vary based on which contrasts are desired. For BIRDS experiments for pH imaging, an anatomical image and spectroscopic imaging (MRSI) sequence must be acquired at a minimum.

A T_2-weighted multi-slice spin echo sequence (MSME) is performed to generate anatomical images as well as quantitative T_2 maps (**Figure 3.2B**). Imaging parameters include a repetition time (TR) of 6 s and equally spaced echo times (TE) ranging from 10 to 100 ms**.** It is important that the FOV (25x25 mm) is the same for the anatomical imaging scans as well as for BIRDS to allow for easy coregistration between the two methods. Further, the slice thickness of the anatomical scans should be chosen to match the resolution of the BIRDS scans. A slice thickness of 1 mm is used for the anatomical imaging and a resolution of 1x1x1 mm^3 for the 3D MRSI. Although the in-plane resolution will differ, the slices can easily be aligned. If needed, a 3D FLASH sequence at reasonable isotropic resolution can be performed for anatomical coregistration (**Figure 3.2A**). Coregistration is important for longitudinal studies where the same animal is to be scanned on multiple occasions and also if other imaging sequences (e.g., DCE, CEST, etc.) necessitating different coil setups are performed on the same animal and the animal must be removed from the bore and repositioned.

After all MRI is performed and prior to the start of BIRDS, the contrast agent infusion is started (see section 3.4). After 30 min of TmDOTP^{5-} infusion, global spectroscopy scans optimized to the chemical shifts of the paramagnetic resonances of TmDOTP^{5-} can be performed to ensure that the three resonances of TmDOTP^{5-} are visible (see **Figure 3.1**). A peak with high SNR at the expected chemical shifts confirms that the infusion of agent was successful, although it does not confirm specifically the location of the agent within the FOV. While continuing the agent infusion, these scans are repeated until adequate SNR has been achieved, usually after 45 min (**Figure 3.2D**). If no signal is detected, the infusion has likely failed and the tail vein line will need to be repositioned in either a more proximal location up the tail or using the other lateral tail vein. Once the first MRSI scan is complete, spectra should be visualized to ensure that acquisition was successful.

Once sufficient agent has accumulated, as evident in the global spectroscopy scans, the 3D MRSI scan optimized for BIRDS with TmDOTP^{5-} is performed. The sequence utilizes a dual-band Shinnar-Le Roux (SLR) RF pulse with duration 205 μs, bandwidth of 40,000 Hz and power of 150 W. The offset of the pulse is -19,800 Hz at 11.7T to ensure that all three proton resonances of TmDOTP^{5-} are excited. The RF pulse has a short duration and very wide bandwidth, but with a null in the middle (minimizing excitation of the water peak). Therefore, the bandwidth of the pulse must cover the chemical shift range where the three proton resonances are expected so that all three resonances can be excited during the same scan. The offset of the pulse must be chosen so that the dual bands cover this chemical shift range. The pulse power must also be optimized to achieve as close to a 90° pulse possible, as this would lead to the highest SNR. Due to the bandwidth. the required power tends to be high and as such, a small surface RF coil is needed for efficient power transfer during excitation. Other acquisition parameters include a TE of 285 μs and a TR of 5 ms. The paramagnetic agents used for BIRDS have incredibly short T_1 and T_2 relaxation times (<2 ms). Therefore, the TR of the MRSI experiment must be extremely short (<5 ms) to have adequate SNR. This also necessitates that no additional features or modifications to the pulse sequence are possible. However, the very short TR does allow for extensive averaging. These experiments are normally acquired in ~18-20 min depending on the number of averages (~120-170 averages) and spherical encoding factor (usually 0.55), and are repeated continuously throughout the duration of the agent infusion. During data analysis, the signal from multiple experiments can be summed to increase the SNR further.

At the end of the contrast agent infusion and the BIRDS scans, the global MRS scan is repeated to confirm that the agent concentration has continued to increase throughout the experiment (See **Figure 3.2D**). The spin echo MRI sequence for T_2 mapping is also repeated. $TmDOTP^{5-}$ acts predominately as a T_2 contrast agent, which can be seen as signal darkening in the tumor upon administration of the agent (See **Figure 3.2C**). The contrast agent concentration can be estimated in multiple ways. The transverse (r_2) relaxivity of the agent can be measured at the given field strength and the T_2 values measured before and after administration of the agent along with the known r_2 relaxivity, allows a voxel scale estimation of the contrast agent concentration.

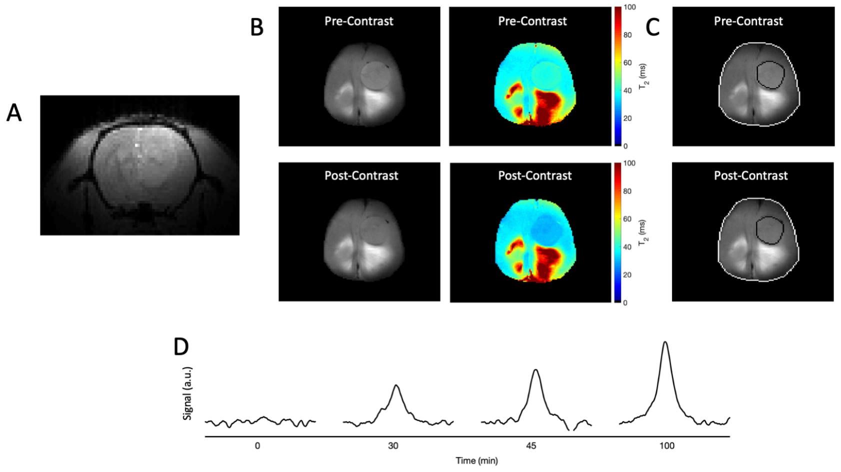

Figure 3.2. Example of in vivo imaging of U87 tumors in rat brain with administration of the contrast agent TmDOTP^{5-}. A high-resolution 3D FLASH sequence is performed for coregistration (**A**). The image can be reconstructed in any orientation (axial reconstruction shown). Coronal anatomical T_2-weighted images (TE: 30 ms, TR: 6 s) and quantitative T_2 maps are acquired before and after administration of TmDOTP^{5-} (**B**). Signal darkening in the T_2 weighted images and a reduction in T_2 values within the tumor after administration of the contrast agent confirms delivery of the agent to the tumor. Note that in the surrounding brain there is also a reduction in T_2 values, suggesting that agent (at a lesser concentration) also extravasates into the brain. The increased contrast can be used to mask the tumor (**C**). The brain is outlined in white and the tumor is outlined in black. Global CSI scans are performed throughout administration of the contrast agent. The H6 proton resonance is shown before (0 min) and after (100 min) of contrast agent infusion (**D**). The global signal from the H6 peak of TmDOTP^{5-} increases throughout the contrast agent infusion, suggesting that the delivery of the agent was successful.

3.3.6 MRI and BIRDS Analysis

All MR data is acquired and processed using Paravision software, while all post-processing and data analysis is performed in Matlab (Mathworks) using custom scripts written in house for Bruker imaging systems. The Matlab scripts are integrated into a package which allows for both MRI and MRSI datasets to be processed in a streamlined fashion.

Reconstructed images from the T_2-weighted sequence and all imaging parameters (FOV, matrix size, number of averages, position offsets, number of slices, slice thickness, echo times, and repetition time) are loaded. The signal intensity data is fitted to single exponential functions to allow for quantitative, multi-slice, 2D longitudinal (T_1) or transverse (T_2) relaxation maps to be generated. Similar fitting algorithms are also possible for apparent diffusion coefficient (ADC) mapping from diffusion-weighted imaging data. For MRSI data, the fid and all acquisition parameters (RF offset, spectral window, RF pulse parameters, and encoding in addition to all listed parameters above) are loaded. Selection of specific imaging parameters and geometric orientations are possible for image visualization and spectroscopic evaluation.

For analyzing BIRDS data, the anatomical images are visualized and appropriate regions of interest (ROIs) around the tumor and the brain are manually selected. The brain (white) and tumor (black) ROIs are outlined on the anatomical images (See **Figure 3.2C**). To mask the MRSI data around the selected ROI, the resolution of the ROI from anatomic imaging is converted into the resolution of the MRSI dataset by resampling the CSI dataset at the same resolution acquired for the anatomical imaging and identifying all tumor voxels. CSI voxels that are more than 50% located within the anatomical mask are identified for masking of the CSI dataset. The ROI (either for the entire brain or only the tumor) is applied to the dataset, so that only values from the correct ROI are maintained.

To analyze the MRSI data, the raw data is output as a “fid” file when using Bruker software. The “slices” in the 3D MRSI dataset that correspond to the slices from the anatomical images are identified. The chemical shift range to analyze for each peak is selected based on the expected resonances for the H6, H2, and H3 protons at -143, 78, and 60 ppm, respectively, under physiological conditions. Generally, a chemical shift range of +/-20 ppm of these values is analyzed. A Fourier transform of the fid data is performed using the fft function in Matlab. On a voxel-by-voxel basis, the data are first-order baseline corrected around each peak by using the linfit function in Matlab and zero-order phase correction is performed around each peak by varying the phase of the spectrum from 0 to 180º and choosing the phase that leads to the most symmetrical peak shape. Line broadening, typically 300-500 Hz, is applied to each peak. Using the previously created ROIs at the resolution of the CSI dataset, the MRSI data is masked either around the entire brain or around the tumor depending on the area of interest for the particular analysis. Voxels outside of the tumor, in the otherwise healthy appearing brain, have low SNR because of the agent not being able to cross the blood brain barrier in large amounts resulting in low tissue level concentrations (<0.5 mM). Strategies can be employed to increase the agent concentration in the brain including the long infusion time such that the agent concentration remains high in the vascular compartment setting up a diffusion gradient from the vascular compartment to the tissue. Further, by infusing over a long time, agent is constantly replacing that which has been cleared, so tissue concentrations can increase with time.

On a voxel-by-voxel basis, the chemical shifts of the three resonances from $TmDOTP^{5-}$ and the water chemical shift are measured, and each of the three chemical shift values are stored as a parameter in Matlab for each voxel. The calibration curve generated from section 3.1 is applied to each voxel using the measured chemical shift values *in vivo*, resulting in a pH value for each voxel. When individual voxel pH values are displayed spatially, this results in quantitative pH maps, as shown in **Figure 3.3**, covering the entire region over which the contrast agent could be detected. These processes can be largely automated in Matlab. However, SNR can become limiting in the brain. Further, due to the larger size of the voxels in the MRSI scan, the factors that influence the chemical shift (namely pH) are an average of the pH values within the voxel and there is likely a distribution of values. This can be reflected in broadening of the peaks or non-Lorentzian line shapes. In voxels in which this occurs, the automated peak fitting might not properly define the peak and manual correction becomes necessary.

For a tumor average, the values in all identified tumor voxels are averaged; however, different spatial analyses can also be performed. In this case, voxels on the tumor boundary/periphery can be chosen and an average value from these voxels can be compared to intratumoral values. Additionally, a spatial distribution of values can be obtained by finding the center of mass (COM) of the tumor and then selecting all voxels in 1 mm concentric circles from the tumor center allowing the gradient to be obtained. Care must be made when interpreting pH values from voxels that contain large contributions from non-tissue compartments including voxels at the edge of the brain where significant vascular contributions may be present and SNR is low, as well as voxels that include the ventricles and other regions with large volumes of CSF. Additionally, in healthy brain, there may be differences in the local environment between gray and white matter that are largely volume averaged in the voxel size achievable with MRSI experiments.

Using BIRDS, the pH_e has been measured in a variety of GBM rodent tumors including 9L and RG2 (**Figure 3.3**). In all tumors studied, the pH_e was found to be acidic with the more aggressive tumor (RG2) having a lower pH_e and the acidification extending beyond the anatomically-defined tumor boundaries.[141] Studies such as this serve as the foundation for treatment studies where it was shown that temozolomide, a common alkylating chemotherapeutic agent used in the treatment of GBM was found to increase the intratumoral pH_e closer to normal values (Chapter 5), potentially serving as a biomarker of the therapeutic response.[142] However, in these prior studies, renal ligation was used to increase the contrast agent concentration, precluding longitudinal measurements of pH_e throughout tumor progression or before and after treatment in the same animal. Given the variation in pH_e between individual tumors, it makes drawing conclusions from individual animal studies challenging. The protocol described here allows for longitudinal studies in both the context of untreated and treated tumors as described further in Chapter 4 and Chapter 5, respectively. Additionally, pH_e is a difficult physiologic parameter to validate *in vivo* and the changes observed were based on *in vitro* calibrations. However, BIRDS also allows for temperature measurements either alone (using $TmDOTMA^-$) or in combination with pH_e (using $TmDOTP^{5-}$). Since temperature is easier to manipulate using direct cooling and can be compared to direct temperature recordings, the remainder of this chapter demonstrates the utility of temperature mapping using BIRDS in the context of a hypothermia model.

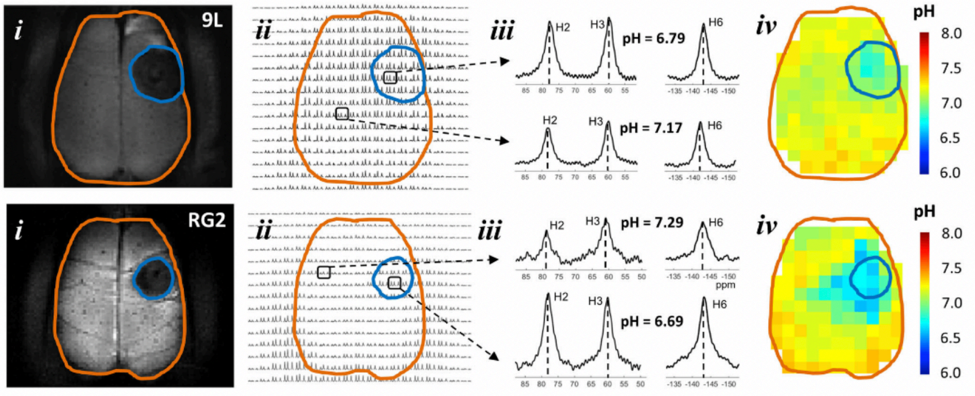

Figure 3.3. Example of in vivo BIRDS pH$_e$ measurements in 9L and RG2 tumor types. The anatomical T$_2$-weighted images (i) are shown with corresponding CSI maps (ii) that were acquired with the same FOV. Representative spectra in select voxels (iii) show the three distinct resonances of TmDOTP^{5-}. From the CSI data, quantitative pH$_e$ maps were produced (iv) that show an acidic pH$_e$ within the anatomically-defined tumors. However, in the more aggressive RG2 tumors, the acidic pH$_e$ spreads the tumor boundary. Reproduced with permission.[141]

3.4 Application to Hypothermia

In traumatic brain injury and its concomitant ischemic injury, the promise of neuroprotection from therapeutic hypothermia remains elusive. The rapid and timely delivery of therapeutic hypothermia for patients with traumatic brain injury (TBI) remains problematic. Two recent randomized clinical trials – EuroTherm 3235 and POLAR RCT- failed to show a treatment effect of therapeutic hypothermia for TBI.[143,144] Unlike patients with cardiac arrest or neonatal hypoxic-ischemic encephalopathy, where the timely application of hypothermia provides neuroprotection, patients with brain injury present a complex array of conditions and comorbidities, which hinder early application of prophylactic hypothermia.

Another potential confounding variable may relate to the method of hypothermia delivery itself. In many previous studies, including the two large randomized trials, the primary methodology to induce hypothermia was the use of intravenous solutions or endovascular devices to achieve systemic whole body cooling. Here we evaluate an innovative technology to induce localized hypothermia in the brain to temperatures known to be neuroprotective, while maintaining overall systemic (i.e., body) normothermia.

Physical and ischemic brain injuries result in inflammatory processes and dysregulated brain cooling mechanisms leading to brain temperatures higher than measured core body temperatures.[145] Therefore, decreasing the brain temperature (therapeutic hypothermia) has been shown to be neuroprotective. Therapeutic hypothermia has demonstrated efficacy and has become a mainstay in treatment of global cerebral ischemia following cardiac arrest, with further evidence suggesting a neuroprotective benefit after TBI and ischemic stroke. Together, these conditions represent major contributors to morbidity and mortality in the United States.[146]

Despite hundreds of unsatisfying pharmacological attempts to identify drugs with neuroprotective effects, hypothermia remains a viable therapeutic option that has demonstrated efficacy. Experimental studies in animal models of ischemic stroke have shown a clear benefit of hypothermia in reducing infarct volumes. Moreover, hypothermia in animal models of TBI has demonstrated neuroprotective effects.[147]

Cerebral temperatures are easily approximated in the absence of pathology when brain and body temperatures are similar and regulated by the hypothalamus. However, in pathological states, brain temperature may deviate from body temperatures.[148] Additionally, under anesthesia, brain temperature decreases.[149,150] Temperatures are elevated in ischemic stroke lesions in the brain,[151] and after brain injury temperature is usually higher than in normal states. The greatest benefit of hypothermia is achieved in the time period immediately following the physical or ischemic injury, and it is therefore critical to start treatment immediately upon symptom/trauma onset. The neuroprotective effects may be lost if hypothermia is induced after reperfusion.

Brain temperature is closely coupled to brain metabolism/perfusion, and tight temperature control is critical for normal brain function.[145] In animals, changes in brain temperature of 2-3 °C have been observed with behavioral stimuli, providing a link between increased brain metabolism/activity and temperature. There is a close relationship between temperature and oxidative metabolism, which is a measure of brain activity.[152] Although temperature is increased in hypermetabolic states, thermoregulatory effects can compensate to lower brain temperature. Since heat exchange in the brain is hindered by its location within the insulating skull, heat is removed primarily by an increase in blood flow. Cerebral flow-metabolism coupling may be lost during hypothermia, where decreased temperature leads to a decrease in both metabolism and blood flow.[145]

Although whole body cooling strategies have been proposed and tested, significant side effects limit their use. These include shivering, decrements in cardiovascular function, immunosuppression leading to higher rates of infection and pneumonia, ion/electrolyte imbalances, and problems with coagulation and acid/base regulation.[153] For ischemia, such as after cardiac arrest, where many organ systems are affected, whole body cooling is likely beneficial. However, for brain injury or focal ischemia during stroke, targeted brain cooling may be more advantageous, by limiting systemic adverse effects. Despite the obvious need for techniques that selectively cool the brain, and possibly even only cool the single affected hemisphere, few current options are available.

The challenge in achieving this aim is to develop techniques that can be implemented quickly in a clinical setting during the critical time window immediately following the injury or onset of ischemia and before reperfusion injury. Methods to lower temperatures can be either noninvasive or invasive.[154,155] Noninvasive methods rely on cold packs/blankets, which generally lower core body temperature as well as brain temperature, or pharyngeal cooling which may be more selective but is limited to temperature decreases 1-3 °C.[156,157] To alleviate these effects, invasive methods try to directly cool the brain. This has been achieved using endovascular approaches whereby intravenous or intraarterial catheters have been inserted and used for intravascular injections of cooled saline/blood.[158] While providing direct and selective cooling, these methods result in transient cooling and are limited by the volume of solution that may be infused, limiting the magnitude of the temperature decrease and the duration of the effect. Depending on catheter placement, these techniques can result in more specific cooling of the brain with less impact on body temperature.

Here we utilize a novel cerebrospinal fluid (CSF)-cooling based platform which allows for chilled saline to be pumped through a closed-loop catheter inserted into the lateral ventricles of the brain.[159] The refrigerant enters by one lumen of the catheter and exits by another, never interacting directly with the CSF. This novel system cools the CSF conductively and, via natural CSF flow, allows convective cooling of the entire brain. Invasive strategies are generally used to provide selective cooling to the brain in an effort to reduce the side effects associated with systemic whole-body cooling. While there are added risks with invasive procedures, this method provides rapid, direct, and reversible cooling that can be maintained over an extended time period.

To demonstrate the efficacy of intracerebral cooling is challenging, given the location of the brain beneath the skull. Further, regional measurements of variations in temperature within the brain, though usually lacking, are indeed required to understand the neuroprotective effects of hypothermia, for example when particular brain regions are not being effectively cooled. Although there are both intraparenchymal and intraventricular temperature probes for directly monitoring brain temperature, these methods allow only for localized temperature measurements at the precise site of the temperature probe. Dynamic and more comprehensive measurements of temperature distributions during cooling are necessary to understand the cooling efficiency of any cooling device prior to clinical translation.

To achieve this we have used Biosensor Imaging of Redundant Deviation in Shifts (BIRDS) with TmDOTMA^- to yield quantitative, high-resolution temperature measurements across the entire brain.[134,136] Using BIRDS, we measured the temperature maps in four healthy sheep brains before, during, and after the onset of cooling induced by the implanted CSF cooling device. The results show sustained decreases in brain temperature across both hemispheres upon the onset of cooling, with a return to baseline temperatures after the cessation of cooling. Throughout all experiments, systemic normothermia of the animals was maintained. Thus, temperature mapping with BIRDS provided a direct measurement of cooling efficiency of a CSF cooling device, which can be further employed in evaluating selective brain cooling strategies for therapeutic hypothermia.

3.5 Temperature study methods

Four juvenile crossbreed neutered male sheep (Ovis *aries*) weighing 26.5, 24.2 kg (age: 14 weeks), 34.5, and 32.0 kg (age: 22 weeks) were supplied by Thomas D. Morris, Inc. (Reisterstown, MD, USA). The lambs were pair housed, provided with environmental enrichment, and acclimated in the Yale Animal Resource Center (YARC) for 9-10 days prior to surgery and imaging procedures. The room temperature was maintained at 22.2 ±1.1 °C with a photoperiod of 12 hours of light and 12 hours of darkness. Water and hay were provided ad libitum and animals were fed 2-3% of body weight daily with commercially prepared ruminant diet (Teklad 7060) supplemented with fresh vegetables. Each animal was examined and determined to be healthy and free of clinical disease by Yale veterinary clinicians.

The Animal Care program is fully accredited by the Association for the Assessment and Accreditation for Laboratory Animal Care International (AAALAC), and all procedures and experiments were approved in advance by the Yale University Institutional Animal Care and Use committee (IACUC).

Each fasted lamb was premedicated with acepromazine (0.05 mg/kg) dosed intramuscularly and then induced with ketamine (2.7 mg/kg) and diazepam (0.2 mg/kg) intravenously to allow endotracheal intubation and subsequent maintenance on isoflurane gas (1-3%) via mechanical ventilation. Buprenorphine (0.01 mg/kg) was given intramuscularly to provide opioid analgesia and lactated Ringers solution was administered intravenously at the continuous rate of 4ml/kg/hour for fluid maintenance. Thermal support was provided with a circulating warm water pad to control and maintain body temperature (38-39 °C), and an orogastric tube was placed to allow venting of gas thus preventing excessive rumen distension.

Prior to the initial incision a local anesthetic injection of 0.5% bupivacaine solution (1 mg/kg) was made at the surgery site to provide multimodal analgesia. Continuous monitoring of the depth of anesthesia and stability of vital signs in the surgery suite was accomplished using a Mindray DPM6 patient monitor (Mindray DS USA, Inc). Burr holes were made bilaterally 1.5 cm anterior and lateral to the posterior fontanelle at an angle of 10° from the sagittal plane on each side. A pediatric slotted stylet was inserted into through each burr hole and guided anatomically into the lateral ventricle. Proper location in the lateral ventricle was confirmed by CSF flow, and pressures were measured by manometry.

The cooling catheters were designed by CoolSpine, LLC (Woodbury, CT) and contain three lumens: two lumens accomplish the delivery and removal of supersaturated saline in a closed loop circuit, which is maintained at -7 to -10 °C. Additionally, the third lumen functions as an external ventricular drain (EVD) for intracranial pressure management. This lumen was modified to allow contrast agent infusion during the imaging procedures. $TmDOTMA^-$ (7mg/kg) was infused directly into the lateral ventricles at an infusion rate of 1ml/h. Two cooling catheters were placed via the burr holes directly into both the right and left lateral ventricles (named right and left catheters, respectively). This technique is consistent with capabilities of common clinical practice in neurological intensive care units. Continuous monitoring of the depth of anesthesia and vital signs in the MRI suite was accomplished using an Invivo Precess 3160DCU patient monitor (Invivo Corporation Orlando, FL USA). Following the completion of the imaging procedures, each animal was euthanatized with an intravenous dose of sodium pentobarbital-based euthanasia solution (Euthasol®).

The magnetic resonance imaging (MRI) and spectroscopy (MRS) datasets were obtained on a Varian 7.0T/68cm horizontal-bore spectrometer (Magnex Scientific Ltd.) using a ^1H resonator/surface coil RF probe. The MR images were acquired using a 128 x 128 gradient-echo (GE) pulse sequence with a field of view (FOV) of 10cm x 10cm, with 17 slices of 5mm thickness with a repetition time (TR) of 200ms and an echo-time (TE) of 5ms. The 17x17x17 3D chemical shift imaging (CSI) datasets were acquired with spherical encoding of k-space as previously described[133] with a TR of 20ms and a FOV of 15.3cm x 15.3cm x 15.3cm. A single-banded refocused 90^0 Shinnar-Le Roux (SLR) radiofrequency (RF) pulse of 40 kHz bandwidth and 500 μs was used for selective excitation of the $TmDOTMA^-$ methyl group protons.

The CSI data was reconstructed to 34x34x17 resolution with a voxel size of $4.5x4.5x9.0\ mm^3$. The spectra were line broadened (200 Hz), phased (zero order) and baseline corrected (first order) in Matlab. The temperature was calculated in each voxel from the chemical shift of TmDOTMA$^-$ methyl group (δ_{CH3}) according to **Equation 3.3**:

$$T = a_1 + a_2(\delta_{CH3} + 103) + a_3(\delta_{CH3} + 103)^2 \qquad \textbf{(Equation 3.3)}$$

where δ_{CH3} is the measured chemical shift of the methyl resonance of TmDOTMA$^-$ and a_1, a_2 and a_3 are 34.45± 0.01, 1.460±0.003 and 0.0152±0.0009, respectively, from linear least square fitting of calibration data over the physiologic range of temperature values.[136] The temperature from each voxel was measured and plotted in an axial slice, which was coregistered with anatomical imaging to show the spatial distribution of the temperature values throughout the brain.

During the imaging session, baseline anatomic images were acquired before the TmDOTMA$^-$ infusion. Next, baseline temperature maps were acquired to establish the basal brain temperature. Then the flow of cooling solution was started through the right catheter at a rate of 35 mL/min, during which CSI data for temperature mapping was obtained. Each animal underwent a cooling paradigm with temperature maps acquired at 10 min intervals throughout all phases of cooling and recovery.

In two animals, flow was initiated in the right catheter and after cooling for 40 min, flow was then directed through both catheters with increasing flow rates up to 48 mL/hr before cooling was stopped and the temperature was allowed to recover. In two additional animals, flow was initiated in the right catheter for 30 min and then stopped for 10 min to allow the temperature to recover. The flow was then restarted in only the left catheter for 30 min. Again after a cooling period, the flow was either stopped and the temperature was allowed to recover or flow was initiated through both catheters. Throughout all phases of cooling and recovery, CSI data was obtained every 10 min for temperature mapping. A final

CSI dataset for temperature mapping was obtained at the end of the experiments after the cessation of cooling to show the return of temperature towards normothermia.

For consistency of the analysis when calculating cooling or recovery rates, we used temperature measurements obtained during the first cooling event in each sheep. The initial cooling phase was considered to be the period after the baseline temperature mapping and until the first period of recovery (during which the flow through the catheter had been stopped). Similarly, the initial recovery phase was the first period during which flow through the catheter was stopped, but before flow of the cooling solution was restarted. The rate of temperature change k was calculated based on the change in temperature (ΔT) divided by the time interval over which the change occurred (Δt).

$$k = \frac{\Delta T}{\Delta t} \qquad \textbf{(Equation 3.4)}$$

The subsequent diverse time courses of temperature change in individual animals (when flow was initiated either through each catheter or when flow was increased through both catheters) showed that BIRDS is able to capture dynamic changes in temperature throughout cooling and is indicative of the robustness and reproducibility of the method.

Regional variations of temperature were assessed by assigning voxels to ROIs corresponding to different brain regions based on a previously published high-resolution sheep brain atlas. All statistics were performed based on average ROI temperature values. All temperature measurements, changes in temperature, and rates of change of temperature are all reported as mean ± standard deviation. All comparisons were assessed using a two-tailed t test where p values <0.05 were considered to be significant.

3.6 Temperature study results

3.6.1 MR Imaging of Catheter Placement

Four sheep underwent catheter placement in both the right and left lateral ventricles. Gross anatomy of the sheep brain provides landmarks that were used for identification of morphological features and for registration to imaging datasets (**Figure 3.4A**). The intraventricular catheter (**Figure 3.4B**) is composed of a tube with a distensible sac at the end to allow variable expansion according to the available ventricle volume and shape. The catheter was designed to circulate chilled saline in a closed circuit via two cooling lines, one for inflow and the other for outflow, to and from the distensible sac. A third (central) line was used for release of the CSF pressure created by the expansion of the distensible sac during cooling. The contrast agent was infused via a thin delivery line (P10) positioned inside the central (pressure-release) line (**Figure 3.4B**).

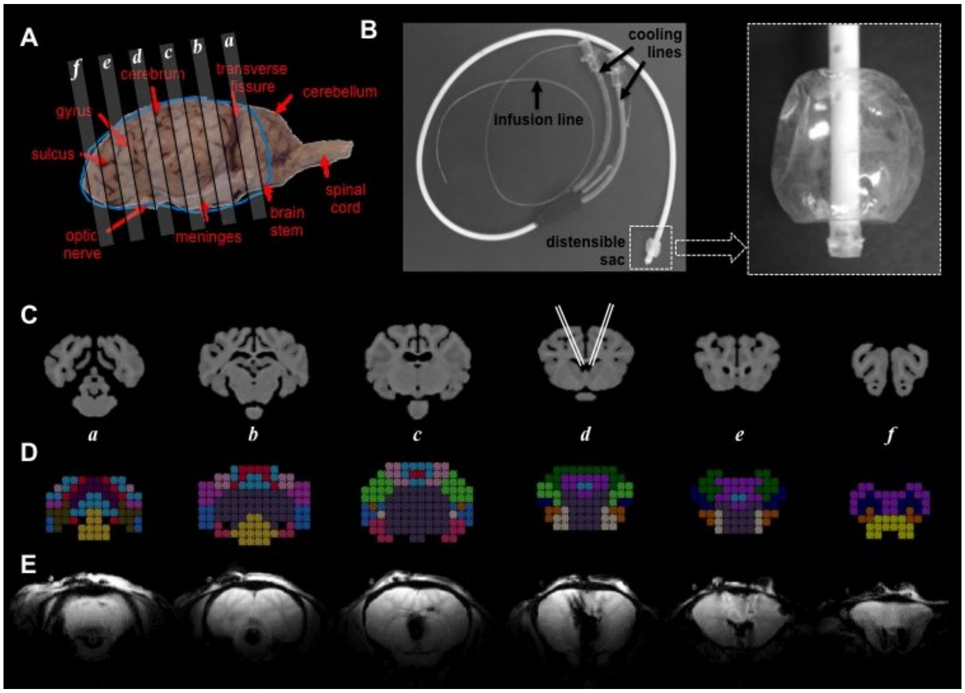

Figure 3.4. Representative anatomical images of the sheep brain and description of the cooling device. The gross anatomy of the sheep brain (A) is shown with several axial slices identified. The cooling catheter used for intraventricular cooling (B) was inserted at an angle into the lateral ventricles of both hemispheres. Representative high-resolution anatomical MR images corresponding to axial slices in (A) are shown in (C), along with the approximate location of the catheters in slice d. Using a previously published anatomical atlas,[160] a lower resolution CSI-based anatomical atlas was generated, and 17 distinct regions of the brain were identified and color-coded (D). The region identifications are summarized in **Figure 3.5**. The MR images acquired during the temperature studies (E) were used for localization of various brain regions.

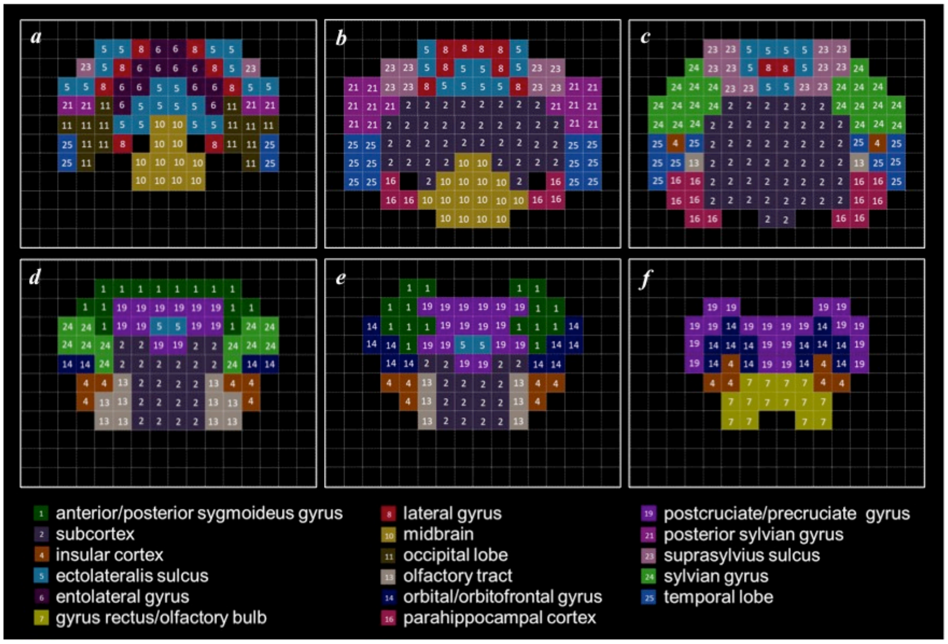

Figure 3.5. Identification of specific brain regions as shown in a sheep brain atlas. The identified regions from the anatomical atlas [21] were rescaled to the resolution of the CSI datasets used for temperature mapping. The numbering of the regions used here is the same as that used in the high-resolution anatomical atlas. However, some of the small regions in the high-resolution anatomical atlas were combined in the CSI atlas reducing the number of regions from 53 to 17. Therefore, the numbering of the regions is not continuous because, when several regions were combined into one, we named the combined region using the name of the largest original region.

A previously published high resolution anatomical atlas of the sheep brain (**Figure 3.4C**) was used to group its 53 high resolution brain regions[161] into 17 separate larger brain regions (**Figure 3.4D** and **Figure 3.5**), that were subsequently used for regional temperature mapping analysis. The regrouping of some of the smaller anatomical regions into larger ones was necessary for better overlap with the lower resolution (4.5mm×4.5mm×9mm) CSI grid. The numbering of the regions used here is the same as that used in the high-resolution anatomical atlas. However, some of the small regions in the high-resolution anatomical atlas were combined in the CSI atlas, reducing the number of regions from 53 to 17. Therefore, the numbering of the regions is not continuous because, when several regions were combined into one, the combined region was named using the number of the largest original region. T_2-weighted anatomical images of the sheep brain were used to verify the approximate position of catheter placement (**Figure 3.4E**).

3.6.2 Temperature Mapping

BIRDS was successfully used for 3D temperature mapping of sheep brain after administration of $TmDOTMA^-$ at a resolution of 4.5x4.5x9.0 mm^3, acquired in about 10 min and repeated throughout several cooling and recovery processes for each animal (**Figure 3.6**). The temperature was calculated according to **Equation 3.3**. Average baseline temperature in the sheep brain was 38.5 ± 0.8 °C, with corresponding body temperature of 39.2±0.4 °C. We used a sagittal slice through the center of the brain to show the temperature distribution in the sheep brain (**Figure 3.6A**) pre-cooling, post-cooling, and after recovery, corresponding to distinct time points in the temperature time course (**Figure 3.6B,** marked with #, * and $, respectively). For all animals, three independent BIRDS measurements were made to establish a baseline temperature before cooling. After chilled saline began to be circulated in the catheters, temperature measurements using BIRDS continued throughout the duration of the experiment. Separate measurements of the left and right hemispheres (**Figure 3.6B**) are shown for each of the 17 brain regions investigated. The time course for temperature in all 4 animals shows reproducible temperature changes throughout the cooling and recovery process (**Figure 3.7**). Although brain temperature fluctuated rapidly with the onset/offset of cooling, body temperature remained nearly constant and normothermic throughout the duration of the experiment (**Figure 3.6B**). The water bath temperature used to maintain the body temperature in the anesthetized animals was not adjusted throughout the experiment, such that the temperature fluctuation represents maintenance of body temperature despite thermal support.

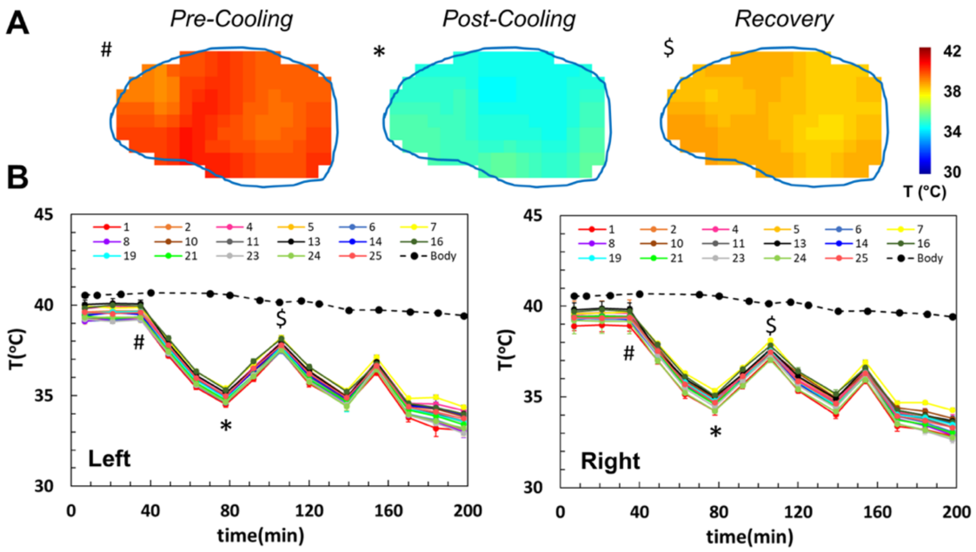

Figure 3.6. Representative example of temperature variation during intraventricular cooling in a sheep brain. During the experiment, several baseline temperature maps were obtained. Temperature maps were then acquired every 10 to 15 min during repeated cooling and recovery cycles, using catheters lateralized to a single hemisphere or in both hemispheres. At the end of the experiment, the flow rate of the chilled saline through the catheter was increased from 35 to 42 mL/min to show that further temperature reductions could be achieved. Temperature maps of a central sagittal slice before cooling (#), after cooling (*), and after recovery ($) are shown in (A). The corresponding time-points are indicated using the same symbols on the temperature versus time curve in (B). The average temperature over time in each of the 17 anatomically defined regions was calculated (B). Additionally, the core body temperature was also measured throughout the duration of the experiment and is shown for comparison. The time course shown represents sheep 4 as shown in **Figure 3.10** and **Figure 3.11**.

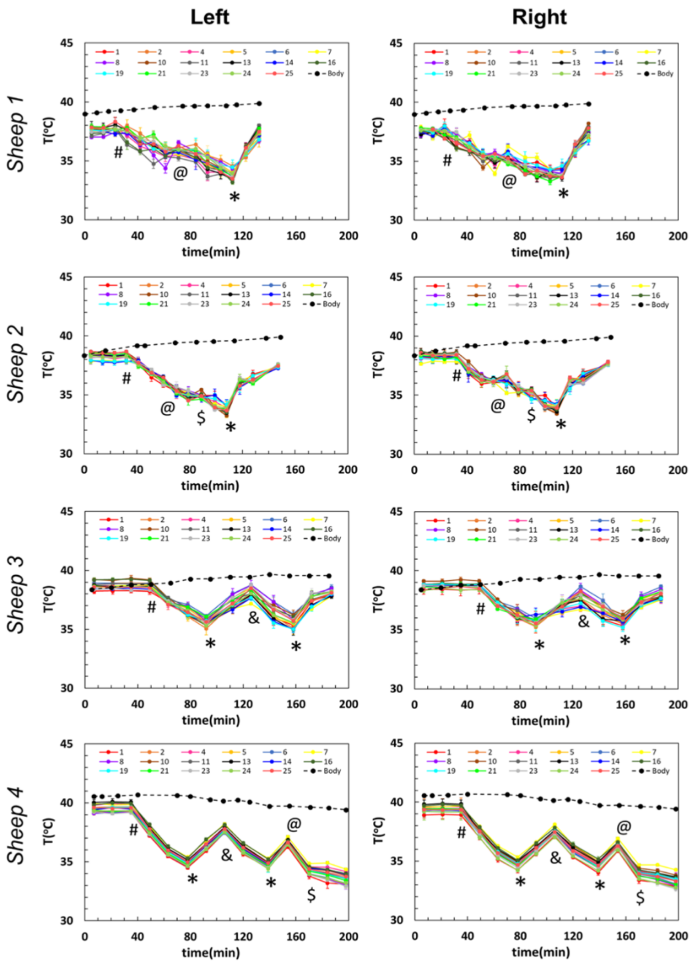

start cooling right
& start cooling left
@ start cooling both

$ increase flow rate
* stop cooling

Figure 3.7. Experimental temperature time courses for all four sheep. Each sheep had two intraventricular catheters implanted, one in each of the right and left lateral ventricles. After baseline temperature measurements, cooling was always started by circulating chilled saline through the right catheter (#). In some animals, cooling was switched to the left catheter (&), while in others cooling was stopped (*) to allow the temperature to return to baseline. The circulation was then switched to the left catheter and the experiment repeated. In some animals, the flow was oriented so that it would go through both catheters (@). The flow rate was always initially set to 35 mL/min; however, in some animals the flow was increased to 42 mL/min ($) to determine if greater reductions in temperature could be achieved.

	Core Body Temp (CBT, °C)	Baseline Brain Temp (BBT, °C)	Nadir Brain Temp (NBT, °C)	% Decrease CBT vs NBT	% Decrease BBT vs NBT	p value
Sheep 1	38.9 ± 0.3	37.6 ± 0.2	33.9 ± 0.4	12.8	9.8	$p<0.0001$
Sheep 2	38.2 ± 0.5	38.3 ± 0.2	33.8 ± 0.2	11.4	11.7	$p<0.0001$
Sheep 3	38.5 ± 0.2	38.7 ± 0.2	35.7 ± 0.2	7.4	7.9	$p<0.0001$
Sheep 4	39.9 ± 0.7	39.5 ± 0.3	33.4 ± 0.4	16.3	15.3	$p<0.0001$
Mean	38.9 ± 0.8	38.5 ± 0.7	34.2 ± 0.9	12.0	11.2	$p<0.0001$

Table 3.1. Temperature results for each sheep. Core body temperatures are calculated as an average of all values prior to initiation of cooling. Baseline brain temperatures are calculated as global brain temperatures just before initiation of cooling. Nadir brain temperatures represent the lowest global brain temperatures reached throughout cooling. Percent changes in temperature are calculated relative to both core body temperature and baseline brain temperatures. All values are reported as mean ± SD. Statistical analyses are performed using a two-tailed Student's t test with p values <0.05 considered significant.

Global brain temperatures were measured as an average of all temperature measurements over the entire brain (**Table 3.1**). An average 11% decrease (4.2 °C) in brain temperature was observed in the four sheep, while the brain temperature decreased an average of 12% relative to core body temperature. The results of the temperature measurements pre- and post-cooling and after recovery in the 17 regions are shown for the left (**Figure 3.8A**) and right (**Figure 3.8B**) brain hemispheres. The differences in baseline temperatures between all regions were distributed throughout a 0.7 °C range. Moreover, based on anatomical identification of brain regions using the high-resolution sheep brain atlas, the 17 brain regions were further combined into two main regions: one superficial (termed non-core) and one deep (termed core) (**Figure 3.9**). We employed this two-zone separation to better understand the differences between superficial and deeper brain structures. The core contained the regions identified as the subcortex, midbrain, olfactory tract, temporal lobe, occipital lobe, and parahippocampal cortex. The rest of the 17 regions were combined into a non-core (superficial) region. When grouped by core and non-core regions, the results show non-significant temperature differences ($p>0.05$) between left and right brain hemispheres in both core and non-core regions, pre- and post-cooling and after recovery (**Figure 3.8C**). Post-cooling temperatures reached 35.5±0.6 °C vs. 35.6±0.2 °C in the right and left hemispheres of the brain, respectively, showing no differences relative to catheter placement (**Figure 3.8C**). When left and right hemispheres were analyzed together (**Figure 3.8D**), the pre-cooling (baseline) temperature of the core of the brain was slightly warmer than non-core regions (~0.2 °C) but was not significant ($p=0.26$). Post-cooling, average brain temperature (including both core and non-core regions) decreased significantly ($p<0.0001$, 38.5±0.7 °C vs. 35.6 ±0.6 °C) and after recovery temperatures increased significantly ($p<0.0001$, 35.6 ±0.6 °C vs. 37.6 ± 0.4 °C). No significant differences were found between core and non-core regions. Interestingly, the temperature after cooling did not differ significantly throughout the different regions of the brain. Although there were slight differences in basal temperatures between core and non-core regions of the brain, the initially warmer core regions reached the same temperature after cooling as the non-core regions, reflecting greater cooling efficiency of the core regions of the brain (**Figure 3.8C** and **3.8D**).

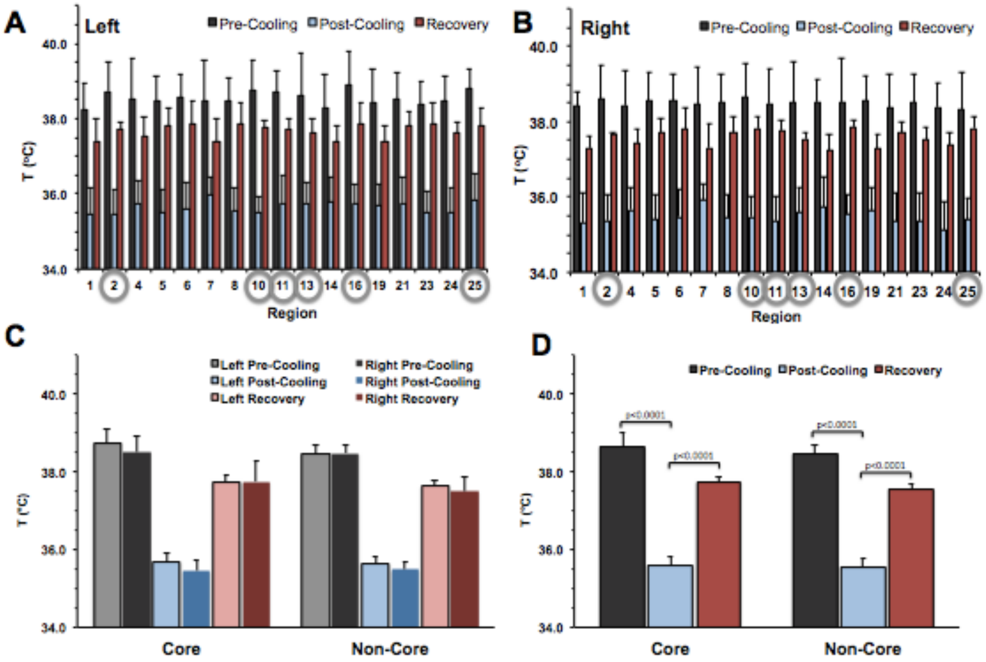

Figure 3.8. Absolute temperature measurements from various regions of the brain. The pre- and post-cooling, and the recovery temperatures are reported for the 17 brain regions (shown in **Figure 3.6**) as average +/- SD in the left (A) and right (B) hemispheres across all animals. Based on their location, these 17 brain regions were further combined into core (deep) and non-core (superficial) regions (**Figure 3.9**). The core regions (subcortex, midbrain, occipital lobe, olfactory tract, parahippocampal cortex and temporal lobe) are identified by gray circles in (A) and (B), while the rest are the non-core regions. The average temperature in the left and right hemispheres for the core and non-core regions is reported before cooling, after cooling, and after recovery (C). No significant changes are observed between the right and left hemisphere of the brain. Average temperatures across the entire brain (D) are also shown. In all regions and for the entire brain, statistically significant temperature decreases (p<0.0001) were achieved during cooling with corresponding significant temperature increases (p<0.0001) after recovery.

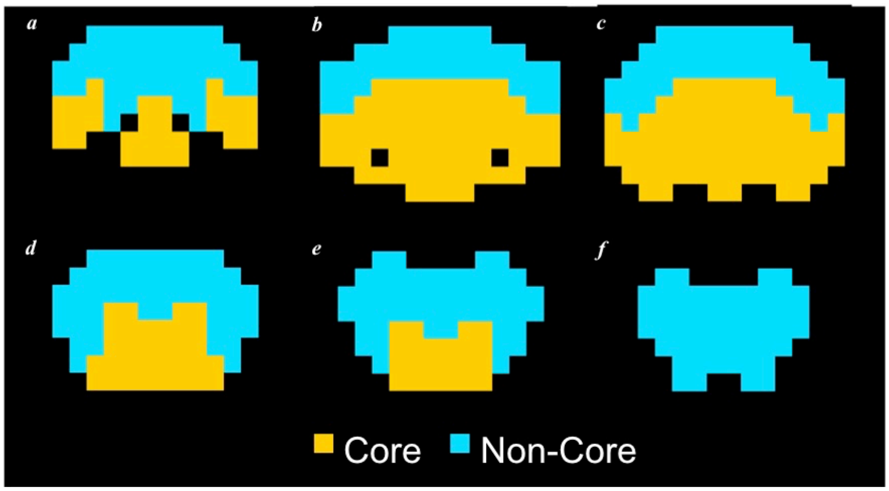

Figure 3.9. Identification of core and non-core regions of the brain. Anatomic regions were classified as either core or non-core based on their physical location in the brain. Of the 17 identified regions, 6 were identified as core regions (subcortex, midbrain, occipital lobe, olfactory tract, parahippocampal cortex and temporal lobe).

3.6.3 Temperature Changes and Rates of Change During Cooling and Recovery

To further quantify the efficiency of cooling, regional variations in the magnitude of temperature change and the rate of change in temperature throughout the brain were calculated. For consistency, we calculated the temperature changes and the corresponding cooling rates only during the first cooling event, done in each of the four sheep using the catheter positioned in the right ventricle. Similarly, we calculated the temperature changes during recovery and the corresponding recovering rates only during the first recovery event. Cooling using one intraventricular catheter resulted in a rapid temperature decrease throughout both core and non-core regions in each sheep (**Figure 3.10A**). Similar temperature changes during cooling were also measured in both the left and right hemispheres (light vs. dark colors in **Figure 3.10C** and **3.10D**). Post-cooling, the absolute temperature throughout the brain was significantly lower, with changes in the range from -2.1°C (in the non-core region of sheep 2, **Figure 3.10C**) to -4.7°C (in the core region of sheep 4, **Figure 3.10C**). When averaging the measurements in all 4 sheep, temperature changes of -3.2±0.5 °C and -3.1±0.5 °C were observed in the core of the left and right hemispheres, respectively (**Figure 3.10D**). In the non-core regions of the brain, the average temperature changes were -2.9±0.4 °C and -3.1±0.4 °C for the left and right hemispheres, respectively (**Figure 3.10D**). Although slightly greater temperature decreases were observed in core vs. non-core regions of the brain (~0.2 °C), this was not found to be significant (p=0.43, **Figure 3.10D**).

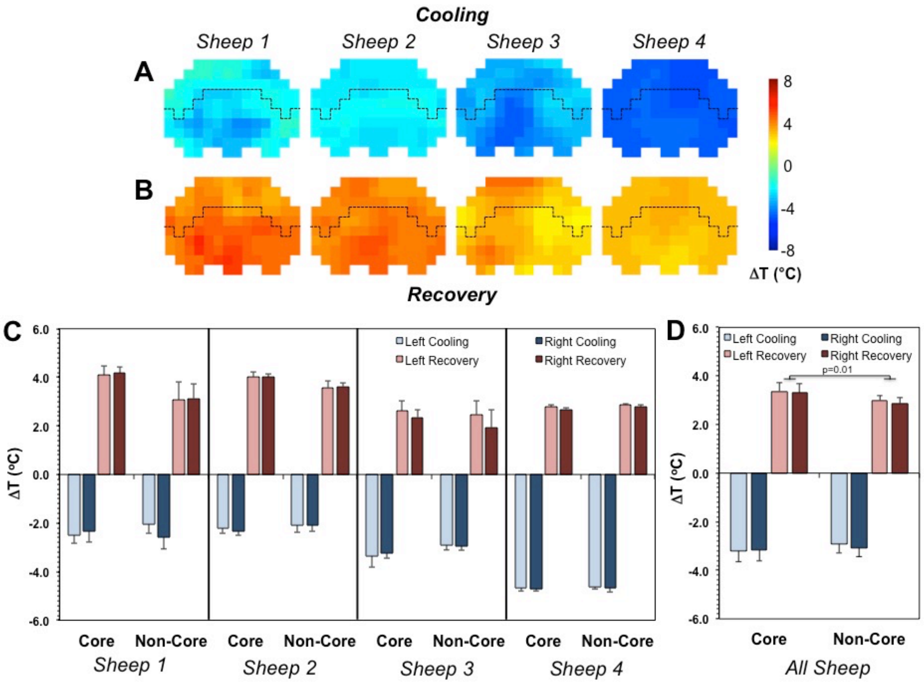

Figure 3.10. Temperature changes during cooling and recovery. Spatial distributions of the absolute temperature change in an axial slice (slice c in **Figure 3.5**) during the first cooling event using the right catheter (A) and during the first recovery (B) in all four sheep. Quantification of the absolute change in temperature during cooling and recovery are shown for both the left and right hemispheres for core and non-core regions of the brain in individual animals (C). Average absolute temperature changes are reported for all animals (D) with significant differences (p=0.01) between core and non-core regions of the brain during recovery. Temperature changes are all reported as average +/- SD. The dashed line in (A) and (B) represents the demarcation between the core (bottom) and non-core (top) regions.

During the recovery period, the temperature in the core regions of the brain increased to a greater extent than in the non-core regions (**Figure 3.10B, 3.10C** and **3.10D**). In the core regions, the average temperature changes during recovery were 3.4±0.3 °C and 3.3±0.4 °C for the left and right hemispheres, respectively, while in the non-core regions these were 3.0±0.2 °C and 2.9±0.2 °C (**Figure 3.10D**). Although there are no significant differences between the left and right hemispheres, there is a greater temperature change (0.4 °C) observed in the core regions versus non-core regions (p=0.01, **Figure 3.10D**). The measured temperatures after recovery show a reestablished temperature gradient in the brain, with core regions slightly warmer than the non-core regions (37.8±0.1 °C vs. 37.6±0.1 °C, **Figure 3.10D**).

To further investigate how fast the brain is cooled, the rate of temperature change (**Equation 3.4**) was compared between core and non-core regions of the brain. Synchronized temperature fall/rise upon cooling onset/offset was observed with cooling rates ranging from 0.05 to 0.11 °C/min and recovery rates ranging from 0.06 to 0.21 °C/min (**Figure 3.11C**). Cooling rates were identical between core and non-core regions, but slightly faster (but not significant) rates were detected during re-warming in core regions (p=0.18, **Figure 3.11C** and **3.11D**). However, there were no differences between ipsilateral or contralateral hemispheres of the brain relative to catheter placement. The average cooling rates were -0.082±0.009 °C/min and -0.080±0.010 °C/min in the core of the left and right hemispheres, respectively, while in the non-core regions the rates were -0.074±0.024 °C/min and -0.079±0.026 °C/min (**Figure 3.11D**). The average recovery rates were 0.118±0.024 °C/min and 0.116±0.026 °C/min in the core and 0.103±0.012 °C/min and

0.100±0.014 °C/min in the non-core regions of the left and right hemispheres, respectively (**Figure 3.11D**).

We also examined whether the volume of the ROI had an effect on the absolute temperature changes and on the rates of cooling/recovery. The subcortex was the largest ROI used in the analysis (volume: 12 mL), while there were many ROIs with smaller volumes (1-3 mL; **Figure 3.5**). The results show that the temperature changes during both cooling and recovery (**Figure 3.12A** and **3.12B**), but also the cooling and recovery rates (**Figure 3.12C** and **3.12D**) were independent of the size of the various brain structures being cooled.

Further temperature decrease was achieved either when we cooled using both catheters or when we increased the flow rate of the circulating chilled saline (**Figure 3.7**). When cooling the brain using both catheters, we achieved an additional temperature decrease of 1.7±0.5 °C in the contralateral (left) hemisphere, and 1.2±0.3 °C in the ipsilateral (right) hemisphere (sheep 1 and 2, **Figure 3.7**). Moreover, after we increased the flow rate through both catheters from 35 to 42 mL/min we achieved another additional temperature decrease of 0.9±0.3 °C in the contralateral (left) hemisphere, and 1.0±0.4 °C in the ipsilateral (right) hemisphere (sheep 2 and 4, **Figure 3.7**). The maximum temperature decrease observed was 6.5±0.1 °C measured in several gyrus regions (ectolateralis, lateral, posterior sylvian, suprasylvius and sylvian) in the right hemisphere in sheep 4 (**Figure 3.7**) where the lowest temperature reached was 32.8 ±0.2 °C.

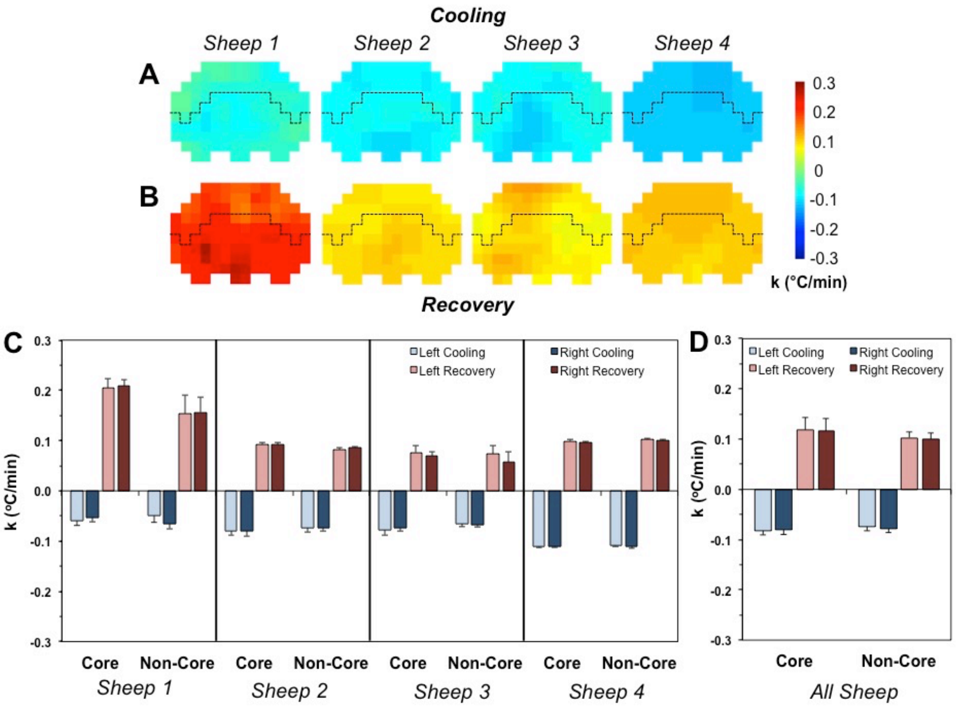

Figure 3.11. Rates of temperature change during cooling and recovery. Spatial distributions of the rate of temperature change in an axial slice (slice c in **Figure 3.5**) during the first cooling event using the right catheter (A) and during the first recovery (B) in all four sheep. Quantification of the rate of temperature change during cooling and recovery are shown for both the left and right hemispheres for core and non-core regions of the brain in individual animals (C). Average rates of temperature change are reported for all animals (D) with no significant differences between the core and non-core regions of the brain or the left and right hemispheres. Rates of temperature changes are all reported as average +/- SD. The dashed line in (A) and (B) represents the demarcation between the core (bottom) and non-core (top) regions.

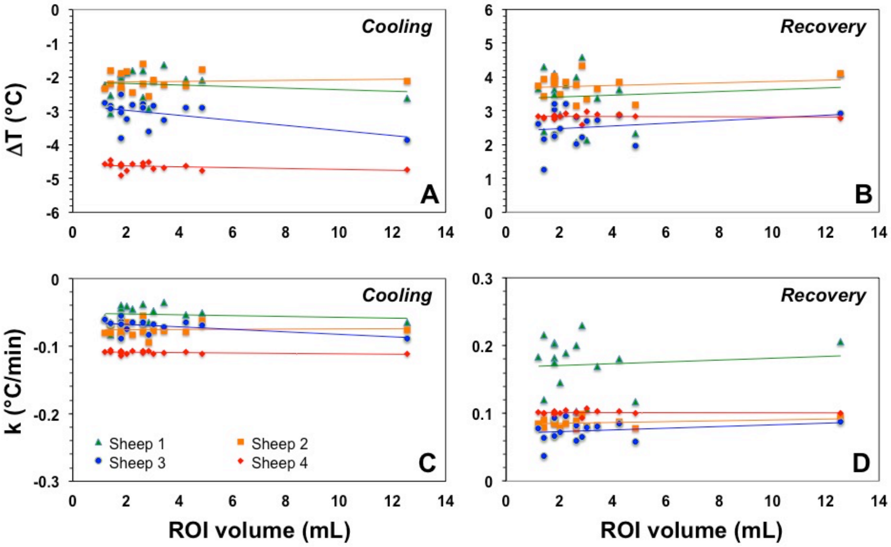

Figure 3.12. Effect of ROI volume on absolute change in temperature and rate of the temperature change. Although the anatomically-defined ROIs are of different sizes, the absolute change in temperature, as well as its rate of change, are independent of the size of the ROI.

3.7 Temperature Study Discussion

Therapeutic hypothermia is neuroprotective; however, prior methods to achieve hypothermia rely on systemic body cooling, resulting in many adverse effects. Although some targeted cooling methods have been proposed, their effects are modest. External cooling devices may only lower brain temperature by <1 °C.[162] Further, measuring the effects of hypothermia is challenging. With systemic body hypothermia, cooling measurements made on the brain surface are not reflective of temperature in deep brain structures. Since metabolism continues in the presence of hypothermia to varying degrees, the temperature throughout a tissue may not be uniform. Therefore, dynamic measurements of spatial temperature distribution made throughout the target tissue are needed to better understand the interaction between cooling and metabolism.

In this work we used temperature mapping with an MRSI method (BIRDS) to measure the temperature distribution throughout the brain during cooling as well as after cooling was stopped (recovery). The usage of a CSF-based intraventricular cooling catheter represents an innovative method for brain cooling. In a prior experiment, we demonstrated cooling of the brain with this CSF-based technology.[159] Brain temperatures in that effort were measured by needle-based temperature sensors that were inserted into the brain parenchyma at a depth of 15 mm posterior and anterior to the ventricles. As those results were site specific and required an additional burr hole for the insertion of the temperature sensor itself, we undertook this current effort to achieve a more comprehensive and less invasive mapping of cooling throughout the brain.

Measuring the cooling rates allows for a dose-response relationship to be established. The amount of cooling (or the “dose”) is reflective of the flow rate of saline and the effectiveness of heat transfer between the CSF and the cooling solution. The dose-response relationship can be easily tuned using the cooling rates measured with BIRDS. For example, to achieve a temperature decrease of 2°C in a brain region where the measured cooling rate was 0.1°C/min, we need 20 minutes of cooling. However, faster cooling can be achieved with higher flow rate of the cooling solution.

The procedure used to insert the catheter is similar to that regularly performed by neurosurgeons to safely access the intraventricular region of the brain to relieve intracranial pressure using ventricular access devices placed in the lateral ventricles. These procedures are commonly and safely performed in the neuro ICU and although not without risks, have a history of successful outcomes in the literature.[163] In addition, expanding this procedure to induce therapeutic hypothermia would add significant benefits without increasing risks.

Other methods currently in use to induce hypothermia, such as intravascular infusions of chilled saline/blood, are also invasive and come with their own risks and may be limited in the degree and length of time hypothermia can be maintained. In contrast, using a CSF cooling catheter, hypothermia could be maintained for as long as the catheter is implanted. Catheters used for intracranial pressure monitoring can be left in place for several days. Therefore, this cooling method is well suited for maintaining hypothermia as long as the temperature of the circulated chilled saline solution is maintained. Moreover, a benefit of the current system is that cooling can be turned off at any point allowing for rapid rewarming, or the flow could be adjusted to maintain specific temperature reductions in the brain.

Although the circulated saline does not enter and is not in direct contact with the CSF, the intraventricular catheter device allows for rapid cooling of the CSF, which then flows throughout the brain, providing generalized cooling via convection. The surface of the brain in contact with the CSF is very large and is increased even further by interactions with the vasculature in perivascular and interstitial spaces.[164] Therefore, by cooling the CSF we were able to efficiently and uniformly remove the thermal energy from the brain and thus to modify its thermal environment.

This is somewhat similar to the primary means of heat removal from the brain via cerebral blood circulation, where changing the vasodilation results in increased blood flow and more efficient heat removal (whereas vasoconstriction results in heat accumulation).[165] Although the catheters were inserted through the right and left hemispheres of the brain, the positions of both catheters are near the center of the brain (**Figure 3.4**), which may explain the relatively uniform temperature distribution during cooling/recovery in the ipsilateral versus contralateral hemispheres.

The supersaturation of the saline solution flowing through the intraventricular catheter can lower the water freezing point; thus the circulating saline has a temperature of -7 to -10 °C in the water pump reservoir. However, one limitation of the current experimental setup is that the non-MR-compatible pump was located ~7 meters away from the magnet bore, allowing the saline solution to warm up while flowing through the delivery line. Therefore, the temperature of the cooling fluid reaching the animal was warmer than in our prior experiments.[159] Thus, we expect that even greater and faster brain temperature decreases may be achievable inside the magnet, with optimization of the delivery method (for example using a thermally isolated delivery line). In human application in the neuro ICU, the length of the cooling lines would be minimal and such issues would not pertain.

A historical thermal map of the primate brain has previously been constructed and illustrated temperature differences of 0.3-0.5 °C between brain regions, with the highest temperatures seen in the deep regions of the brain.[166] In the case of basal temperature data in the sheep brain, we observed variations between brain regions of up to 0.7 °C, in good agreement with prior literature values demonstrated in a sheep brain.[167]

The effects of anatomic site and activity on brain temperature have been reviewed extensively;[164] these studies highlight potential hemispheric differences in temperature, but also demonstrate temperature fluctuations due to sleep, arousal, and stimulation. In addition, under anesthesia there are also differences in brain temperature from the awake state, with temperature reductions seen, and minimal fluctuations in temperature.

We did not observe any interhemispheric differences, with regional differences between the right and left hemisphere generally not exceeding 0.3 °C. It has been noted that regional brain temperatures increase more rapidly than arterial temperatures, suggesting that local heat production due to increased metabolism is primarily responsible. In humans, deep brain temperature is less than 1 °C higher than body temperature.[168] Ambient environmental temperature can impact superficial cerebral sites, but has no effect on deep brain structures or blood temperature.

Temperature mapping with BIRDS using $TmDOTMA^-$ has been well characterized and validated.[136] In contrast to previous applications of BIRDS for temperature mapping, where $TmDOTMA^-$ was injected into circulating blood, here we directly injected the agent into the CSF via the intraventricular cooling catheter. Other temperature mapping techniques, such as phase shift MRI have been applied to monitor temperature changes in the brain.[156] However, the phase shift MRI method can only report a change in temperature, and not the absolute temperature. Furthermore, accuracy is reduced because the sensitivity of the temperature measurement by phase shift MRI is on the order of 0.01 ppm/°C, compared to 0.7 ppm/°C for BIRDS with $TmDOTMA^-$.

The error in temperature measurement is directly related to the signal-to-noise ratio (SNR) observed for the $–CH_3$ proton resonance.[136] The SNR values higher than 5 measured in the sheep brain indicate an error in the temperature measurements smaller than 0.01 °C. Similar cooling experiments were previously performed in sheep by our group, in which the local temperature was measured using thermocouples in four brain regions. The temperature changes (1.4 - 5.7 °C) and the rates recorded are similar to those observed here with BIRDS.

In terms of changes during cooling seen within individual sheep in this study, the absolute temperature for Sheep 4 decreases much more than in the other three sheep. This can be attributed to the baseline temperature being higher by nearly 1 °C in this animal. Also, since the brain metabolism competes with the cooling process, this higher temperature decrease could be due to a lower brain metabolism in this sheep, possibly because of a deeper state of anesthesia. We also observed that the absolute temperature for sheep 1 and 2 during recovery increased by about 1 °C more than in the other two sheep (**Figure 3.10B** and **3.10C**), most likely because of a lower brain temperature at the beginning of the recovery period, achieved while cooling the brain using both catheters (in sheep 3 and 4 only the right catheter was used for cooling before the recovery period).

Although the number of animals used (n=4) was low, the aim of the current study was to assess the degree of hypothermia achieved by intraventricular cooling by measuring 3D temperature profiles throughout the brain. One limitation of this study is that there was no secondary validation of the temperature changes measured with BIRDS. However, direct temperature recordings using the same cooling system have been made previously using thermocouple probes inserted directly in four cortical brain locations.[159] These thermocouple measurements provided similar results, with temperature decreases of 3.7 °C, which are in agreement with the current BIRDS results from the cortical (non-core) regions of the brain (3.0 °C). This comparison is summarized in **Table 3.2**. However, comparisons between these two measurements must be mindful of the following differences. For the thermocouple measurements, cooling was induced using two catheters (right and left) with continuous cooling for 3 hr. For BIRDS, cooling was varied between the right and left catheter (or both) and was stopped and started over the course of 2 hours to better study the dynamics of the temperature changes induced by the cooling catheter. Moreover, for the thermocouple measurements, the temperature reported is an average value from four temperature sensors placed in the anterior and posterior cortex of both the right and left hemisphere, while for BIRDS we used the average cortical temperature. It should also be noted that there is variability between animals for both thermocouple and BIRDS measurements, which may be due to the effectiveness of the catheter placement, the level of brain metabolism and/or anesthesia depth.

Moreover, the temperature measurements with BIRDS have been validated *in vivo* in the rodent brain under several different activity states.[136,169] The $TmDOTMA^-$ MR signal is not dependent on ion concentrations or pH, which is important for its application to disease states, such as TBI or stroke, which are known to induce both ion imbalances and dysregulated osmoregulation. The measurements made in this current study are performed in otherwise healthy brain tissue, which should have uniform characteristics allowing for quantitative temperature mapping without other contributing factors. Systemic body temperatures measured by a rectal probe were monitored throughout the duration of this study and showed only minimal changes (±1 °C) in systemic temperature throughout the experiment (**Figure 3.6** and **Figure 3.7**). Note that typically animals under anesthesia experience a decrease in body temperature; therefore, while the animals were under anesthesia, a body warming blanket was used to maintain the body temperature despite the cooling of the brain tissue. This is an applicable strategy that could be employed clinically, as heat gain by the body is not expected to significantly increase brain temperature, permitting maintenance of systemic normothermia.

Hypothermia is the only treatment shown to be neuroprotective in global cerebral ischemia following circulatory arrest. This provides positive implications for potential neuroprotection in TBI and ischemic stroke. Further, hypothermia has been a mainstay of surgical procedures involving deliberate cardiac arrest, including many forms of open heart surgery (in which core body temperatures are commonly lowered to below 18 °C).[170] Although significant hypothermia is required following spontaneous cardiac arrest, the data following ischemic stroke are less clear, with neuroprotective effects being demonstrated with much smaller levels of cooling (e.g., core body temperature reductions to 34 °C).[171]

Lowering the temperature results in reduced cellular metabolism and lower oxygen demands of any tissue and reduces the stress placed on damaged cells. The greater the tissue cooling, the greater the reduction in oxygen consumption, and therefore oxygen demand, allowing cells to tolerate inflammatory and ischemic conditions better. There are also affected mechanisms at the cellular level, whereby hypothermia reduces the development of inflammation and necrosis in ischemic regions.

	Thermocouple					BIRDS			
Sheep #	1	2	3	4	5	1	2	3	4
Baseline T (°C)	38.7	38.8	38.2	37.5	37.8	37.6	38.2	38.6	39.4
Cooling T (°C)	33.4	37.3	33.8	31.8	36.0	35.7	36.2	35.7	34.7
Delta T (°C)	5.4	1.4	4.4	5.7	1.8	1.9	2.0	2.9	4.7
% Change	-13.9	-3.6	-11.4	-15.1	-4.7	-5.1	-5.2	-7.5	-11.9

Table 3.2. Comparison of previously reported thermocouple temperature measurements to BIRDS temperature measurements during cooling using the intraventricular catheter. Brain temperatures reported by thermocouple are the average of four thermocouples inserted in into anterior and posterior regions of both the right and left cortex. [159] Brain temperatures reported by BIRDS are the average of all cortical (non-core) voxels. The baseline temperature is the brain temperature just before initiation of cooling. The cooling temperature is the brain temperature after cooling. These two values are then used to calculate the change in temperature (ΔT) and the percent change in temperature from baseline. Note that the temperatures reached after cooling using the thermocouples were after 3 hours of continuous cooling, whereas the temperatures measured by BIRDS were after cooling in a single catheter for 30-40 min.

Ischemia leads to neuronal damage through several mechanisms including energy depletion, excitotoxicity, calcium influx, membrane damage, formation of free radicals, and activation of protein kinases.[171] In the case of TBI, treatment is challenging due to the heterogeneity of the presenting modes of injury and clinical symptoms.[146] Further, the time after injury or the onset of ischemia will always be a confounding factor in understanding the effects of hypothermia.

Although questions will always remain about the optimal cooling methodology, targeted temperature, and duration of hypothermia, selective and targeted cooling strategies show potential for improved management of localized brain injury and ischemia, where temperature mapping with BIRDS could provide the means to assess the efficiency of the cooling strategies throughout the whole brain. In the future we plan to compare different cooling strategies and to assess therapeutic efficacy of mild hypothermia in a large animal model of TBI.

3.8 Conclusion

Recent clinical trials failed to demonstrate the promise of therapeutic hypothermia in TBI, yet neuroprotection against ischemic injury remains a high clinical priority. Despite the myriad of successful animal studies in TBI as well as in other morbidities, use of topical cooling has been unsuccessful. However, perhaps it is not the hypothermia itself that has limited the translation of therapeutic hypothermia, but rather the method of delivery has not been effective. The use of this novel CSF-based cooling platform results in significant and uniform cooling throughout the cortex of the sheep brain, which has similar ventricular landscape as the human brain. Interestingly, by using a single catheter, the technique can induce cooling throughout both hemispheres of the brain. Temperature mapping with high spatiotemporal resolution using BIRDS was feasible in the sheep brain both before and after induction of hypothermia. BIRDS allows for rapid imaging that has high temperature sensitivity, allowing for robust and accurate temperature mapping. In these experiments, CSF-based cooling provides a very efficient method for inducing therapeutic hypothermia, raising promise for improved clinical treatment of TBI or ischemia, because the brain can be selectively cooled, obviating the adverse side effects of whole body cooling.

Chapter 4: Imaging Hallmarks of the Tumor Microenvironment in Glioblastoma Progression

4.1 Abstract

Glioblastoma progression involves multifaceted changes in vascularity, cellularity, and metabolism. Capturing such complexities of the tumor niche, from the tumor core to the periphery, by magnetic resonance imaging (MRI) and spectroscopic imaging (MRSI) has translational impact. In human-derived glioblastoma models (U87, U251) we made simultaneous and longitudinal measurements of tumor perfusion (F_p), permeability (estimated with the transfer constant K^{trans}), and volume fractions of interstitial (v_e) and plasma (v_p) spaces from dynamic contrast-enhanced (DCE) MRI, cellularity from apparent diffusion coefficient (ADC) MRI, and extracellular pH (pH_e) from an MRSI method called Biosensor Imaging of Redundant Deviation in Shifts (BIRDS). Spatiotemporal patterns of these parameters during tumorigenesis were unique for each tumor. While U87 tumors grew faster, vascularization seemed more aggressive for U251 tumors, as reflected by the higher rate of increase for F_p, K^{trans}, and v_p parameters. Perfused regions between tumor periphery and core with U87 tumors exhibited higher F_p, while K^{trans} of U251 tumors remained lowest at the tumor margin, suggesting primitive vascularization. Tumor growth was uncorrelated with v_e, ADC, and pH_e. U87 tumors showed correlated regions of reduced v_e and lower ADC (higher cellularity), suggesting ongoing proliferation. U251 tumors had higher core v_e and elevated ADC (lower cellularity), suggesting necrosis development. The entire tumor was uniformly acidic (pH_e 6.1-6.8) early and throughout progression, but U251 tumors were more acidic, suggesting lower aerobic glycolysis in U87 tumors. Characterizing these cancer

hallmarks with DCE-MRI, ADC-MRI, and BIRDS-MRSI is useful for exploring tumorigenesis as well as timely therapies targeted to specific aspects of the tumor microenvironment.

4.2 Introduction

Glioblastoma (GBM) is the most frequently occurring and aggressive primary brain tumor in adults.[172] Despite intensive surgical and medical intervention, prognoses remain poor with an average survival of less than 2 years.[173] Magnetic resonance imaging (MRI) with transverse (T_2) or longitudinal (T_1) relaxation times can elucidate potential changes between tumor and normal tissue and is used for initial clinical identification upon symptom onset, although biopsy remains the gold standard for diagnosis. Specifically, contrast-enhanced T_1-weighted and T_2 fluid-attenuated recovery (FLAIR) images are used for clinical detection and size monitoring after treatment;[174] however, there remain numerous unmet imaging needs as many findings are nonspecific and do not allow for direct mapping of the tumor microenvironment that may be reflective of treatment response.[175] Further, these imaging contrasts largely ignore spatial heterogeneity as tumors are extremely diverse in their anatomic features, do not highlight variation in tumor metabolism and vasculature which are reflective of different genetic mutations in GBM, and are confounded in the setting of different therapies, especially anti-angiogenic therapies, that results in drastic changes in the imaging findings despite little change in the structural tumor architecture.[16] Therefore, more specific imaging methods are needed to characterize tumor progression as well as to evaluate therapeutic response. In this study, we aim to demonstrate multi-modal longitudinal characterization of the GBM microenvironment in preclinical GBM models to highlight the spatial heterogeneity that exists in tumor cellularity, vascularity, and metabolism and how it changes throughout tumor progression.

Tumorigenesis in GBMs is highly complex and involves metabolic changes in tumor cells and interactions with the surrounding microenvironment. GBMs, like other solid tumors, display many of the hallmarks of cancer including dysregulated metabolism and vascularization which drives the promotion of angiogenesis.[2] Angiogenesis, the development of new blood vessels, occurs in tumors in response to the development of hypoxia and to aid in delivery of nutrients to the metabolically active tumors. However, the newly formed vasculature is tortuous and leaky. The tumor microenvironment is shaped by these abnormalities in the vascular architecture leading to heterogenous and inadequate perfusion.

GBMs are highly heterogeneous due to tumor growth patterns and development of necrosis. Spatial heterogeneity, not only in morphology, but also in perfusion and metabolism may contribute to differing patient prognoses and therapeutic efficacy. Thus, detecting and measuring tumor size does not fully capture the tumor phenotype. Hypoxia develops in specific regions of the tumor and contributes to tumor aggressiveness. Therefore, imaging methods to quantify the vascular architecture of tumors is important for tumor characterization and has been studied using a MRI technique termed dynamic contrast enhanced (DCE) MRI.[176] DCE-MRI models the dynamic uptake and exchange of gadolinium-based contrast agents between the vascular and tissue spaces, specifically those regions in which the agent has extravasated into the extravascular space. This can identify tumor regions that have high vascular permeability or conversely, regions that are under-perfused and indicative of regions of hypoxia. The images are acquired with a high temporal resolution and the signal intensity-time curves are then converted to a contrast agent concentration term that is then fit to a two-compartment exchange model.[82] This allows for several vascular parameters to be quantified, including the plasma flow (perfusion), vascular permeability, extracellular volume fraction, and plasma volume fraction.

Additionally, GBMs undergo a metabolic upregulation of glycolysis even in the presence of sufficient oxygen, a phenomenon termed aerobic glycolysis (Warburg effect). This leads to elevated production of intracellular acids and lactate, which are then extruded thereby acidifying the extracellular environment.[3,41] Specifically, extracellular acidosis, defined as a reduction in the extracellular pH (pH_e) in relation to intracellular pH (pH_i), is an important indicator of tumor aggressiveness as the reduction in pH_e has been directly linked to increasing tumor invasiveness, reduced therapeutic response, increased angiogenesis and immunosuppression.[8] In normal brain tissue, the pH_e is ~7.2-7.4, but in tumors there is a drastic reduction in pH_e to ~6.2-6.8.[141] Metabolic abnormalities are not confined to tumor cells, but also shape the tumor microenvironment leading to distinct locations both within and beyond the tumor boundary that are more prone to cancer cell survival.[177]

Thus, metabolic imaging methods have become a focus in the past decade for tracking cancer. Several imaging methods have been proposed and studied for measuring both pH_i as well as pH_e.[86] While pH electrodes are the gold standard, a variety of imaging methods including optical, PET, and magnetic resonance imaging and spectroscopic methods have been used for quantitative pH mapping. However, these methods vary in their specificity for pH_e (vs pH_i) and their ability to quantify the pH. In this study, for pH_e imaging we use a magnetic resonance spectroscopic imaging (MRSI) method called Biosensor Imaging of

Redundant Deviation in Shifts (BIRDS). BIRDS uses the pH-sensitive chemical shifts of non-exchangeable protons of lanthanide-based contrast agents.[134] The chemical shifts are characterized in relation to their temperature and pH sensitivities *in vitro*. The signals are resilient and can be observed even in the presence of strong T_2 contrast agents, and therefore are unaffected by the presence of other contrast agents.[178] BIRDS agents have been modified to increase their delivery and thereby their sensisitvity.[132,179,180] Further, BIRDS has been used to map the pH_e in a variety of tumor models.[181,182]

Quantitative BIRDS-pH_e mapping has revealed highly acidic tumors where pH_e changes can reflect tumor viability and response to therapy.[141,142] However, BIRDS-pH_e mapping requires the use of paramagnetic contrast agents, such as thulium 1,4,7,10-tetraazacyclododecane-1,4,7,10-tetra(methylenephosphonate) ($TmDOTP^{5-}$), and limitations due to the need for sufficient contrast agent accumulation have previously prevented longitudinal pH_e measurements. However, organic anion transporter inhibitors (e.g., probenecid) can slow the renal clearance of the contrast agent.[135] Here we demonstrate that a co-infusion of probenecid and $TmDOTP^{5-}$ can allow for repeated longitudinal pH_e mapping in the same tumor over time and when combined with multi-modal imaging can be useful in measuring tumor growth and monitoring the tumor microenvironment in human-derived models of GBM. We were able to measure tumor growth and map pH_e in the same U87 and U251 gliomas reproducibly and found that despite significant tumor growth, acidosis plateaus early in tumor formation once the tumor is identifiable by imaging methods.

In this study, the cellularity, vascularity, and acidosis of untreated U87 and U251 human-derived GBM models were measured longitudinally throughout tumor progression. U87 and U251 orthotopic glioma models exhibit many characteristic microenvironmental features of human GBM in different aspects including the development of necrosis, rapid growth, invasion into surrounding tissue, and differences in vascularization that lead to hypoxic regions and enhanced angiogenesis.[183,184] However, a limiting factor in translating preclinical GBM treatment studies is being able to longitudinally and non-invasively map the tumor microenvironment in the same tumor over days and weeks. The vascularization of these tumors is important for delivery of MRI contrast agents, including gadolinium agents used for the DCE method and $TmDOTP^{5-}$ used for BIRDS.

Here we describe a multi-modal MRI study of mapping the vascularity, cellularity, and acidosis in the tumor microenvironment in the same imaging space longitudinally throughout tumor progression, which enabled interrogating spatiotemporal changes of these parameters through tumor progression. We hypothesized that there would be restructuring of the vasculature over time in these models, and that metabolism would change throughout progression. While common measures of tumor progression are only tumor size, we hypothesized that these measures would provide additional characterizations of the changing tumor microenvironment that were not solely related to the size of the tumor and changes might develop earlier during tumor formation. Characterization of the vascular and metabolic microenvironment in tumors is essential for choosing therapeutic strategies as well as for monitoring tumor progression and therapeutic response.

4.3 Methods

4.3.1 Cell Culture

U87 cells were purchased from American Type Culture Collections (ATCC) and U251 cells were from Dr. Meser Ali at Henry Ford Hospital. All cells were maintained in an incubator in a 5% CO_2 atmosphere at 37 °C. Dulbecco's modified eagle's medium (DMEM) was supplemented with 10% heat-inactivated fetal bovine serum (FBS) and 1% penicillin-streptomycin. U87 cells were cultured in high glucose (4.5 g/L) DMEM and U251 cells were grown in low glucose (1.5 g/L) DMEM. All cells were used at low passage (<20). Cells (U87 and U251) were harvested at high confluence (>80%) and suspended in serum-free DMEM prior to intracranial injection.

4.3.2 Animal Models of GBM

All animal protocols were approved by the Institutional Animal Care and Use Committee (IACUC) at Yale University. Female athymic/NUDE rats were acquired from commercial vendors (Envigo) and weighed 150-250g. Animals were maintained in temperature and humidity-controlled rooms with food and water provided *ad libitum*. Animals were housed for a minimum of two weeks prior to experimentation.

For intracranial injection of U87 and U251 cells, the animals were anesthetized with isoflurane (2-3%). The animals were positioned in a stereotactic holder and the scalp was sterilized with betadine and 70% ethanol. Local anesthetic (Bupivacaine, 2 mg/kg) was administered prior to a midline incision of their scalp. After exposing the skull, a hole was drilled using a motorized drill at a position 3 mm to the right of the bregma. A 5 μL suspension of 2×10^5 U87 cells or 5×10^5 U251 cells was loaded into a 10-μL Hamilton syringe equipped with a 26G needle. The needle was positioned through the burr hole and injected 3 mm below the dura into the right striatum. The cells were injected using a microinfusion pump at a rate of 1 μL/min over 5 minutes. The needle was then left in place for 5 minutes prior to being removed at a rate of 0.5 mm/min to prevent any leakage of cells from the injection site. The burr hole was sealed with bone wax and the incision site was sutured and sterilized. Animals were given carprofen (5 mg/kg, subcutaneously) for analgesia during the procedure which was continued for 48 hours postoperatively. Animals were monitored daily for weight loss or development of any neurological symptoms. Tumors were allowed to grow for 10 days prior to initial MRI experiments to monitor for tumor growth.

4.3.3 MRI

All imaging data were acquired using an 11.7 T Bruker horizontal-bore spectrometer. 10-15 days after cell injection, animals underwent T_2-weighted MRI to check for tumor formation using a spin-echo sequence with TR 6000ms and 10 TE (10-100ms), FOV 25x25mm^2, matrix 128x128, and slice thickness 1 mm. During imaging, body temperature was maintained using a circulating warm water heating pad and Paralube vet ointment was applied to the eyes to prevent dryness. Imaging was repeated every 3-7 days until a tumor was identified on T_2-weighted imaging, typically 1-2mm, prior to beginning the multi-modal imaging protocol. Due to experimental variations, tumors were initially identified at days 10-28 for U87 tumors and days 13-69 days for U251 tumors. After tumor identification, animals underwent the full multi-modal imaging protocol, which was then repeated every 4-7 days, unless predetermined humane endpoints were met (e.g., body weight loss, clinical neurological signs), in which case the animals were immediately imaged and euthanized.

For the multi-modal imaging studies, which require the administration of contrast agents, a tail vein infusion line was first established prior to the experiment. During this procedure, the animal was anesthetized with 3% isoflurane and placed on a heating pad to maintain body temperature and ointment was placed on the eyes. A 30G needle was inserted into a PE10 (Braintree Scientific, LLC) line and filled with heparinized saline. The needle was inserted into the lateral tail vein of the rat and checked for backflow to ensure correct placement within the vein, prior to being anchored to the tail with tape. Heparinized saline (~50 μL) was flushed through the line approximately every 20 min throughout the remainder of the imaging session to ensure proper functioning of the infusion line and to prevent clotting.

The animal was placed in a prone position within a volume (8 cm) transmit/surface (3.5 cm) receive radio-frequency (RF) coil (RAPID MR International). The animal and coil were then placed in the isocenter of the magnet bore. Body temperature was monitored using a rectal fiber-optic temperature probe and the breathing rate was monitored using a respiratory monitor.

The imaging protocol consisted of the following order of sequence acquisition which were acquired over a 6 hour imaging session. Positioning and power optimizations were performed using Bruker-defined gradient-echo (GE) and fast spin-echo (FSE) sequences. Shimming was done on an ellipsoid voxel to bring the H_2O linewidth down to less than 30 Hz. Quantitative T_2 mapping was performed by acquiring T_2-weighted images acquired using the same parameters listed above for initial tumor identification. Diffusion-weighted imaging was performed using an EPI sequence with 6 b values (0-3000 s/mm^2). Apparent diffusion coefficient maps were generated by fitting voxel-level data to a monoexponential function in MATLAB. Quantitative T_1 mapping consisted of T_1-weighted images acquired using a RARE sequence with TE 10ms, 5 TR (400-8000ms), slice thickness 0.7mm with 0.3mm gap, 25 × 25 mm FOV, 128 × 128 matrix. Quantitative T_1 maps were generated by fitting voxel-level data to a monoexponential function in MATLAB. The multi-TR T_1 sequence was then repeated after DCE-MRI (see below) to serve as a post-contrast image which was used, along with T_2 images, to delineate tumor boundaries. Because this was acquired at the end of the DCE acquisition, it represented late (20 min after contrast agent infusion) contrast enhancement. A contrast enhanced T_1-weighted 3D FLASH was also acquired with TE 5ms, TR 30ms, and 0.33mm isotropic resolution for high-resolution coverage of the entire tumor for coregistration.

4.3.4 DCE-MRI

DCE-MRI was acquired using a dual-echo spoiled gradient echo acquisition (TR/TE: 39ms/2.5-5ms) with a flip angle of 15° every 5 seconds over 22 min. At 2 min into the dynamic scan, a bolus IV injection of 0.25mmol/kg gadobutrol (Gadavist, Bayer HealthCare Pharmaceuticals Inc.), a clinically available macrocyclic gadolinium agent, was injected and then flushed with heparinized saline. For co-registration, DCE-MRI acquisition was done over three central slices of the tumor aligned with the same positioning, FOV (25 × 25 mm), and matrix (128 × 128) as the T_1 sequence.

Measurements from pre-contrast T_1-weighted images were used to transform the signal time-intensity curves into time-concentration curves (TCCs), using the dual echo acquisition to correct for the T_2 effect of the contrast agent. The arterial input function (AIF) was measured by collecting arterial blood samples at discrete time points post-injection in a representative animal. A hematocrit of 0.45 was assumed for deriving the contrast agent concentration in the blood. The raw AIF was fit to a bi-exponential curve and applied to the analysis for all datasets. A region of interest (ROI) was placed in the tumor, including the contrast-enhancing rim, which was the area used for all analyses.

To measure vascular parameters [K^{trans} (volume transfer coefficient, min^{-1}), F_p (plasma flow rate, min^{-1}), v_e (interstitial volume fraction, unitless), v_p (plasma volume fraction, unitless)], a two-compartment exchange model (2XCM) was used to fit the DCE data. The parameters were estimated by fitting each voxel using least squares regression using MATLAB.[185] All parameters were quantified on a voxel by voxel basis in the predefined ROI, and spatially plotted in MATLAB overlaid on T_2-weigheted images.

4.3.5 BIRDS pH_e Measurements

Prior to the start of pH mapping, the animal was removed from the magnet bore and transferred to a custom-built 1.4 cm single loop surface coil. The animal was repositioned in a ventral position such that the tumor was located where coil sensitivity was highest and then the animal and coil were reinserted into the magnet. Position and optimization scans were performed as described previously. Next, quantitative T_2 mapping was performed for tumor localization. For BIRDS pH_e measurements, 100 mg/kg probenecid was administered over 10 min and followed after 20 min by a co-infusion of 100 mg/kg probenecid and 1 mmol/kg $TmDOTP^{5-}$. Probenecid was used to increase the plasma concentration of the circulating contrast agent and reduce its rate of renal clearance. All infusions were performed using a syringe pump at a rate of 15 μL/min for a total infusion time of 100 min. MRSI began 45 min after the start of the infusion and the total imaging time was 56 min.

Chemical shift imaging for BIRDS was performed to measure the chemical shifts of the pH_e-dependent proton resonances of $TmDOTP^{5-}$ to calculate pH_e within each voxel at an isotropic resolution of $1mm^3$ as previously described.[133,134,141] A 205 μs dual-banded Shinnar-Le Roux pulse with a bandwidth of 40kHz was used for excitation of the H2, H3, and H6 resonances of $TmDOTP^{5-}$. The pH_e in each voxel was quantified and the average pH_e of all voxels within the tumor boundary defined by T_1 contrast enhancement was measured. At the end of the BIRDS experiment, post-contrast quantitative T_2 mapping was performed such that reductions in T_2 could be related to contrast agent concentration and T_2 contrast could be used for identifying tumor margins. Although Gd^{3+} is injected earlier in the experiment, the agent does not impact the chemical shifts from $TmDOTP^{5-}$, largely clears from the tumor prior to starting BIRDS and at this concentration does not have significant T_2 effects.

4.3.6 Histology

At the end of the imaging experiment, animals were perfused and the brain was extracted and fixed in 4% paraformaldehyde prior to slicing into 3 mm coronal slabs. The tissue was paraffin-embedded and sectioned into 10 μm slices. Sections were deparaffinized and rehydrated prior to hematoxylin and eosin (H&E) staining using standard protocols. In a subset of tumors, tissue sections also underwent immunohistochemistry (IHC) for proliferating cell nuclear antigen (PCNA) and vascular endothelial growth factor (VEGF) with hematoxylin as a counterstain. In brief, sections were deparaffinized and rehydrated prior to antigen retrieval and peroxidase blocking. Sections were incubated with primary antibodies (PCNA, VEGF) followed by incubation with a biotinylated secondary antibody and 3,3-diaminobenzidine (DAB). All stained sections were mounted on glass slides and microscopy was performed (4×, 10×) for digitization and visualization using an automated high-resolution microscope with stitching capabilities (Keyence, IL, USA).

4.3.7 Statistical Analysis of Parametric Maps

Each parameter was assessed within the tumor boundary defined by both T_2 and T_1 contrast enhancement at each time point. Average tumor values were quantified as the average of all tumor voxels over three imaging slices. Values in all cases are reported as mean ± standard deviation. Parametric maps were registered in the same space and voxel level distributions were shown to reflect the heterogeneity in parameter measurements.

For the spatiotemporal analysis of each parameter, the imaging slice with the largest tumor cross-sectional diameter was selected. The total number of voxels across all three tumor slices were utilized to calculate the tumor volume. Each voxel was also assigned a depth value based on distance from the tumor margin, within the 2-dimensional plane of the selected slice. The depth values for voxels of each tumor were individually rescaled so that the largest depth for each tumor would be 1, and we call this rescaled parameter the distance to the tumor margin (0 is tumor margin or periphery, 1 is center of tumor). Various relaxation, diffusion, DCE and pH_e parameters were plotted against distance from the tumor margin and tumor volume. Fitting was done using quadratic surfaces (2nd order polynomials). Given internal tumor heterogeneity, the Bisquare fitting algorithm was used to make the fitting robust to outliers. For easier comparison, each of the coefficients for the polynomial surface fit were normalized to the median parameter value (averaged medians for both U87 and U251 tumors) and the largest tumor volume (for the respective tumor type, U87 or U251).

4.4 Results

4.4.1 Tumor Growth

Both U251 and U87 tumors were monitored longitudinally over up to three time points. A total of 25 time points acquired across 14 rats with U87 tumors and 24 time points acquired across 12 rats with U251 tumors were used in the analysis. Tumor volume was measured using both T_2-weighted and contrast-enhanced T_1-weighted imaging to manually identify tumor margins over all imaging slices (**Figure 4.1**). After tumor detection, size increased exponentially in both U251 and U87 tumors (**Figure 4.1**). Tumor growth was normalized to when tumors were first identified by imaging (Day 0), usually once reaching 1-2 mm in cross-sectional diameter. The tumor size at time of initial scan was 18.4 ± 7.1 mm^3 for U87 tumors and 20.7 ± 9.2 mm^3 for U251 tumors. By the final time point, tumor volume reached 166.9 ± 35.2 mm^3 for U87 tumors and 103.9 ± 24.6 mm^3 for U251 tumors. While at the initial time point the two tumors were approximately of the same size, at the final time point both tumors grew significantly larger but U87 tumors were ~60% larger than U251 tumors ($p<0.0004$). At the same time points, cellularity (from ADC), vascularity (from DCE), and metabolism (from BIRDS) were also successfully monitored longitudinally in the same subjects (**Figure 4.2**).

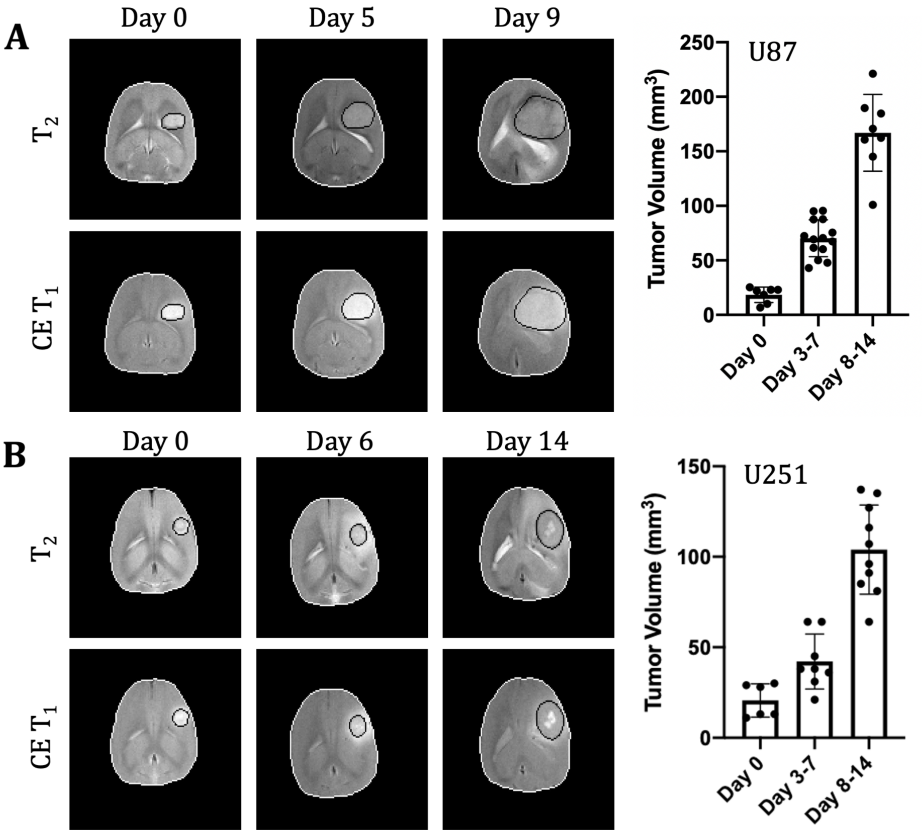

Figure 4.1. Longitudinal growth characteristics of U87 and U25 tumors. T_2 and contrast enhanced T_1-wegithed imaging contrasts are shown at three time points in the same U87 (A) and U251 (B) tumors. The tumor is outlined in black and the brain in white. Tumor volume was measured across all imaging slices and quantified by multiplying the number of tumor voxels by the imaging spatial resolution and slice thickness. Imaging timepoints across all tumors are included.

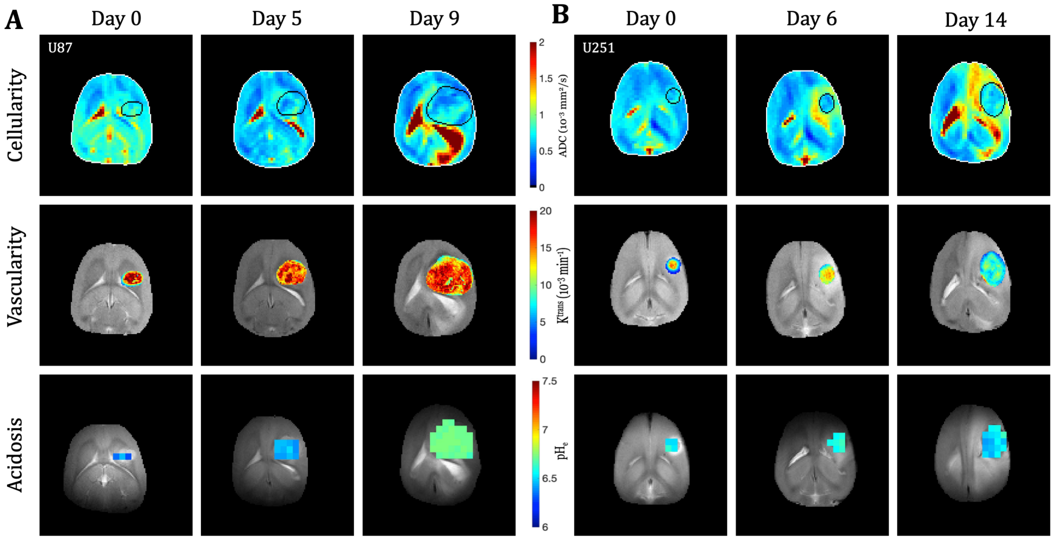

Figure 4.2. Longitudinal multi-modal imaging of U87 and U251 tumors. The apparent diffusion coefficient (ADC) maps reflect cellularity, the K^{trans} maps from DCE reflect vascularity, and the pH_e maps from BIRDS reflect acidosis. Imaging was performed at three different timepoints in the same U87 (A) and U251 (B) tumors. The tumor was masked using T_2-weighted and contrast-enhanced T_1-weighted imaging. Vascular parameters from DCE and pH_e from BIRDS were calculated in the masked tumors.

4.4.2 MRI Relaxation (T_1, T_2, and contrast-enhanced (CE) T_1)

Quantitative T_1 and T_2 relaxation maps were acquired across all time-points in addition to the advanced vascular and metabolic imaging methods. In both U87 (**Figure 4.3**) and U251 (**Figure 4.4**) tumors, T_1 and T_2 values were higher in the tumor compared to surrounding tissue. T_1 values between tumors were not significantly different at the final time point (p=0.22), but increased with tumor progression from the initial to final timepoint for both tumor types (U87: 2.24±0.13 s vs. 2.53±0.07 s, p<0.0001; U251: 2.19±0.09 s vs. 2.47±0.04 s, p=0.0009). For T_2 the values between tumors were moderately different at the final time point (p=0.026), but there was a trend in increasing T_2 with tumor progression for both tumors types (U87: 41.3±2.9 ms vs. 43.3±2.1 ms, p=0.16; U251: 38.5±2.5 ms vs. 41.0±1.5 ms, p=0.06).

Tumors displayed contrast enhancement (CE T_1) and significantly (p<0.001) reduced T_1 values within the tumor core after gadobutrol infusion on T_1-weighted images in U87 (**Figure 4.3**) and U251 (**Figure 4.4**) tumors. For CE T_1 values between tumors were not significantly different at the final time point (p=0.26). CE T_1 increased with tumor progression for U87 (1.12±0.10 s vs. 1.29±0.16 s, p<0.03) but not for U251 (1.27±0.20 s vs. 1.16±0.25 s, p=0.43). U87 tumors displayed homogenous signal enhancement that was confined by the tumor margins (**Figure 4.3**); however, U251 tumors exhibited much greater heterogeneity in enhancement patterns with contrast accumulating in central tumor regions as well as leaking into surrounding brain tissue, resulting in contrast enhancing regions changing based on time since contrast agent administration (**Figure 4.4**). These patterns were reflected in post-contrast quantitative T_1 mapping such that with tumor progression, U87 tumors had higher post-contrast T_1-values than U251tumors. This was somewhat expected given the same amount of contrast agent in a larger tumor volume resulting in decreased concentration and lesser T_1 shortening.

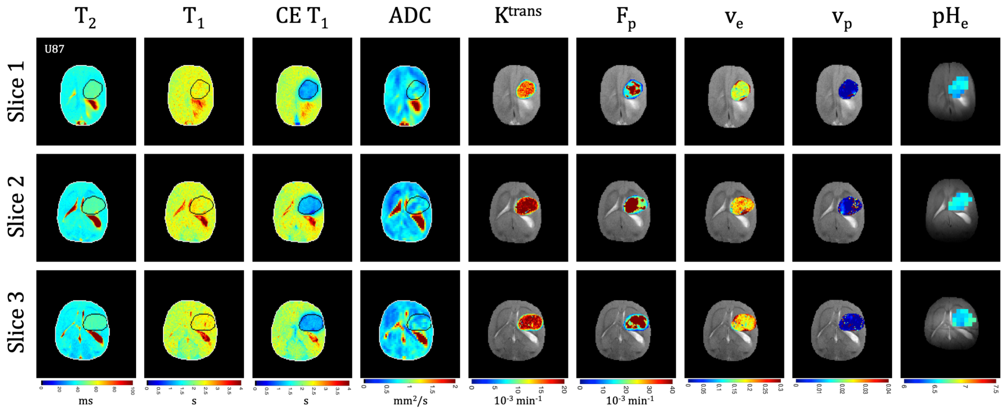

Figure 4.3. Multi-slice, multi-parametric imaging of U87 tumors. All data is from a single imaging session for a single animal. Cellularity (ADC), vascularity (F_p, K^{trans}, v_e, v_p with DCE) and metabolism (pH_e with BIRDS) as well as quantitative T_2 and pre/post-contrast T_1 mapping are included. Three imaging slices were used for all imaging contrasts, allowing for extensive 3D characterization of the tumor microenvironment. Multi-slice measurements were performed for all included time points.

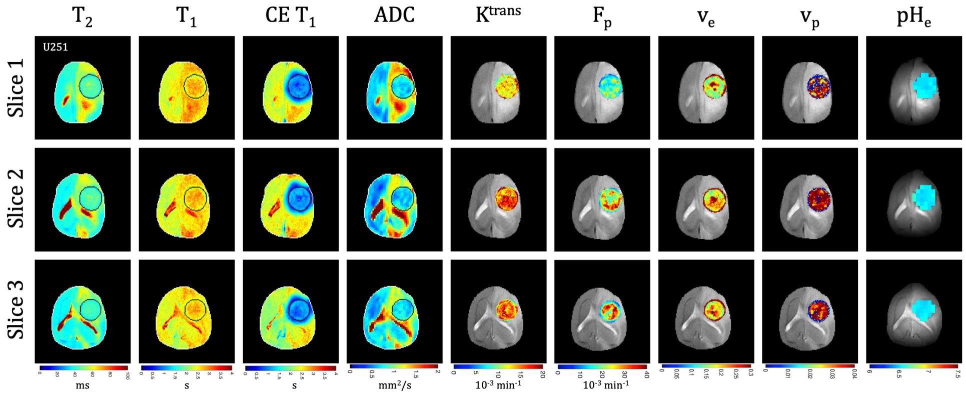

Figure 4.4. Multi-slice, multi-parametric imaging of U251 tumors. All data is from a single imaging session for a single animal. Cellularity (ADC), vascularity (F_p, K^{trans}, v_e, v_p from DCE) and metabolism (pH_e from BIRDS) as well as quantitative T_2 and pre/post-contrast T_1 mapping are included. Three imaging slices were used for all imaging contrasts, allowing for extensive 3D characterization of the tumor microenvironment. Multi-slice measurements were performed for all included time points.

4.4.3 ADC and DCE

Quantitative ADC maps were generated across 3 imaging slices at each timepoint from diffusion-weighted imaging at multiple b values. Since ADC has been shown to be correlated with tumor cellularity,[80] the ADC was used as an indication of the proliferative status of U87 (**Figure 4.3**) and U251 (**Figure 4.4**) tumors. ADC parameter distributions were homogeneous for both tumor types. ADC values between tumors were not significantly different at the final time point (p=0.26), nor did they change for either tumor between time points (p=0.72 for U87; p=0.75 for U251). With tumor progression and increasing tumor size, ADC trended towards lower values across both tumor types.

There was heterogeneous dynamic uptake of gadobutrol within the tumor core as measured with DCE and reflected in the vascular parameters. Further, tumor progression was associated with an increased heterogeneity in all vascular parameters. F_p and K^{trans} were lowest at the tumor margin in both U87 (**Figure 4.3**) and U251 (**Figure 4.4**) tumors. For all DCE parameters the values between tumors were not significantly different at the final timepoint compared to the initial timepoint for either U87 or U251 tumors (**Table 4.1**). However, the parameter values were highly heterogenous within each tumor which leads to the large standard deviations. At the final time point, there also was no difference between the tumor types for K^{trans} (p=0.33), v_e (p=0.30), and v_p (p=0.73); however, the perfusion (F_p) tended to be higher in U87 tumors although this did not reach significance (p=0.08).

	K^{trans} (10^{-3} min^{-1})	F_p (10^{-3} min^{-1})	v_e	v_p
		U87		
Time Point 1	12.43±1.34	22.14±11.17	0.21±0.07	0.028±0.016
Time Point 3	14.48± 5.90	50.74±40.27	0.20±0.06	0.038±0.043
p value	0.39	0.09	0.72	0.54
		U251		
Time Point 1	8.89±4.11	14.41±7.09	0.35±0.17	0.063±0.051
Time Point 3	12.20±2.61	23.19±8.96	0.25±0.10	0.045±0.031
p value	0.10	0.09	0.18	0.45

Table 4.1. Quantitative values and statistical comparisons for K^{trans}, F_p, v_e, and v_p vascular parameter values. Parameter values are quantified from DCE-MRI for U87 and U251 tumors between the initial and final time point. Parameter values were averaged across all 3 slices from all tumors and are reported as average ± standard deviation. Two tailed t tests are used to compare changes in the parameter values with tumor progression.

4.4.4 BIRDS

Signal enhancement after gadobutrol administration corresponded to regions of signal darkening after $TmDOTP^{5-}$ in T_2-weighted images providing multiple contrasts for measuring tumor size. Further, coinfusion of probenecid and $TmDOTP^{5-}$ allowed for successful repetitive pH_e mapping in the same tumor for the first time. At all timepoints, the intratumoral pH_e was lower (pH 6.1-6.8) than the pH_e of the brain parenchyma (~7.1) indicating that the intratumoral microenvironment becomes acidic early during tumor growth, once the tumor becomes detectable by imaging methods. However, longitudinal pH_e mapping using BIRDS revealed that as tumors become larger there is no clear corresponding change in pH_e. Acidosis developed early during tumor formation and remained acidic throughout tumor progression. Across all timepoints, the average pH was higher in U87 compared to U251 (6.54±0.08 vs. 6.47±0.14; p=0.046). In U87 tumors, larger tumors had the same pH_e as smaller tumors (6.56±0.05 vs. 6.56±0.09, p=0.94) while in U251 tumors, larger tumors were slightly more acidic although this was not found to be statistically significant (6.44±0.15 vs. 6.58±0.06, p=0.12). The pH_e remained relatively homogenous throughout the tumor with minimal spatial variation. The pH_e at the core of both tumors reached similar values in smaller tumors; however, in U87 tumors, the pH_e initially decreased with progression, but was then higher in the largest tumors.

4.4.5 Spatiotemporal patterns of tumorigenesis

All parameters were quantified with increasing distance from the tumor margin (spatial) and tumor volume (temporal) in both U87 (**Figure 5**) and U251 (**Figure 6**) tumors. Coefficients for the polynomial surface fits of each 3D spatiotemporal plot were calculated for both U87 and U251 tumors, where quadratic fits were significantly superior to linear fits to the 3D surface.

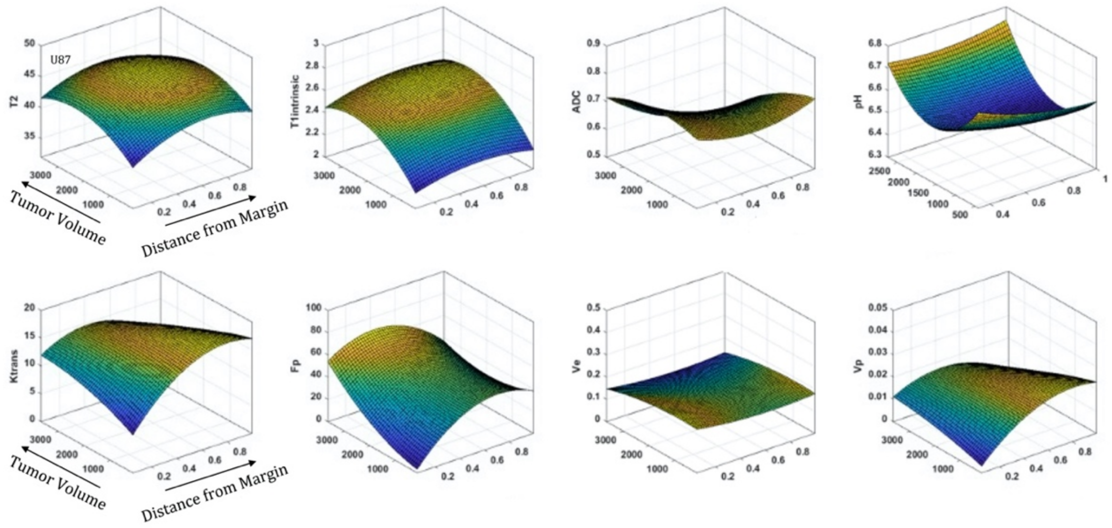

Figure 4.5. Spatial and temporal variation in parameter measurements throughout U87 tumor progression. With progression, tumor volume increases. The spatial distribution is determined by measuring the distance from the tumor margin (0 is tumor margin, 1 is center of tumor). Measurements include cellularity (ADC), vascularity (F_p, K^{trans}, v_e, v_p from DCE) and metabolism (pH_e from BIRDS) as well as quantitative T_2 and pre/post-contrast T_1 parameter values are included. All imaging voxels across all timepoints and all tumors were fit to a 2nd order polynomial to illustrate the variation of spatial parameter distributions with tumor progression.

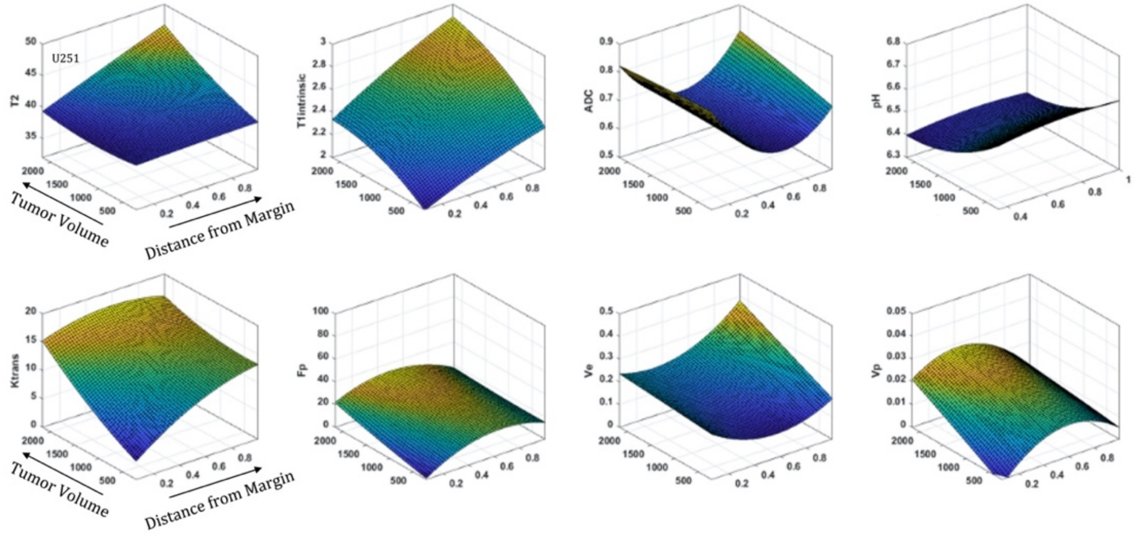

Figure 4.6. Spatial and temporal variation in parameter measurements throughout U251 tumor progression. With progression, tumor volume increases. The spatial distribution is determined by measuring the distance from the tumor margin (0 is tumor margin, 1 is center of tumor). Cellularity (ADC), vascularity (F_p, K^{trans}, v_e, v_p from DCE) and metabolism (pH_e from BIRDS) as well as quantitative T_2 and pre/post-contrast T_1 parameter values are included. All imaging voxels across all timepoints and all tumors were fit to a 2nd order polynomial to illustrate the variation of spatial parameter distributions with tumor progression.

With increased tumor progression (increasing volume), there was a significant increase in intrinsic T_1 in both U87 and U251 tumors. However, there was a homogenous distribution of the T_1 and T_2 relaxation measurements across U87 tumors independent of tumor size. U251 tumors exhibited significant increases in T_1 and T_2 in central regions of larger tumors that were not evident at initial tumor detection, possibly indicative of necrotic cores and which were not evident in U87 tumors as supported by H&E histological findings (**Figure 4.7A**), where necrotic regions are indicated by red arrows in U251 tumors and no necrotic regions were observed in U87. Additionally, the spatial distribution of ADC values was not uniform, with higher ADC values observed at the tumor margin and in the center of the tumor. These differences were more pronounced in U251 tumors. The highest values of ADC were observed in the central regions of large U251 tumors, the same regions that exhibited higher T_1 and T_2 relaxation rates. The spatiotemporal patterns of changes in ADC were similar in both U87 and U251 tumors as ADC was higher at the periphery regardless of tumor size, as supported by PCNA IHC data (**Figure 4.7A**) with increased PCNA staining at the tumor margins.

In U87 tumors, there was much greater homogeneity in the vascular parameter values. The interstitial and plasma volume fractions tended to decrease with tumor progression, indicating increased cellularity. Tumor progression also led to an increase in plasma flow, while vascular permeability (estimated by K^{trans}) remained constant. Although the average vascular permeability did not change over time, there was an increase in heterogeneity such that regions with higher vascular permeability also had higher plasma volume fraction and plasma flow. In terms of spatial distribution, the highest value in K^{trans},

F_p, and v_p were seen in intermediary regions of the tumor, compared to the tumor center and periphery.

In U251 tumors, there were notable differences in the interstitial volume fraction with tumor progression. With tumor progression, the interstitial volume fraction increased significantly in deeper regions of the tumor. This corresponded with a reduced plasma volume fraction and plasma flow in central regions of the tumor. In U251 tumors, the vascular permeability (estimated by K^{trans}) increased with tumor progression and the spatial heterogeneity actually decreased, reflective of higher K^{trans} values throughout the tumor and as supported by increased VEGF IHC staining throughout the tumor (**Figure 7B**).

At the time of initial tumor detection, when tumors were small, permeability and the v_e were comparable between U87 and U251 tumors and showed increasing values with tumor progression that was most pronounced at the growing edge of the tumor. In both U87 and U251 tumors, F_p exhibited similar increasing trends during tumor progression, but at all stages of tumor growth, perfusion tended to be higher in U87 tumors. Additionally, the plasma volume fraction increased at the periphery of both U87 and U251 tumors with tumor progression.

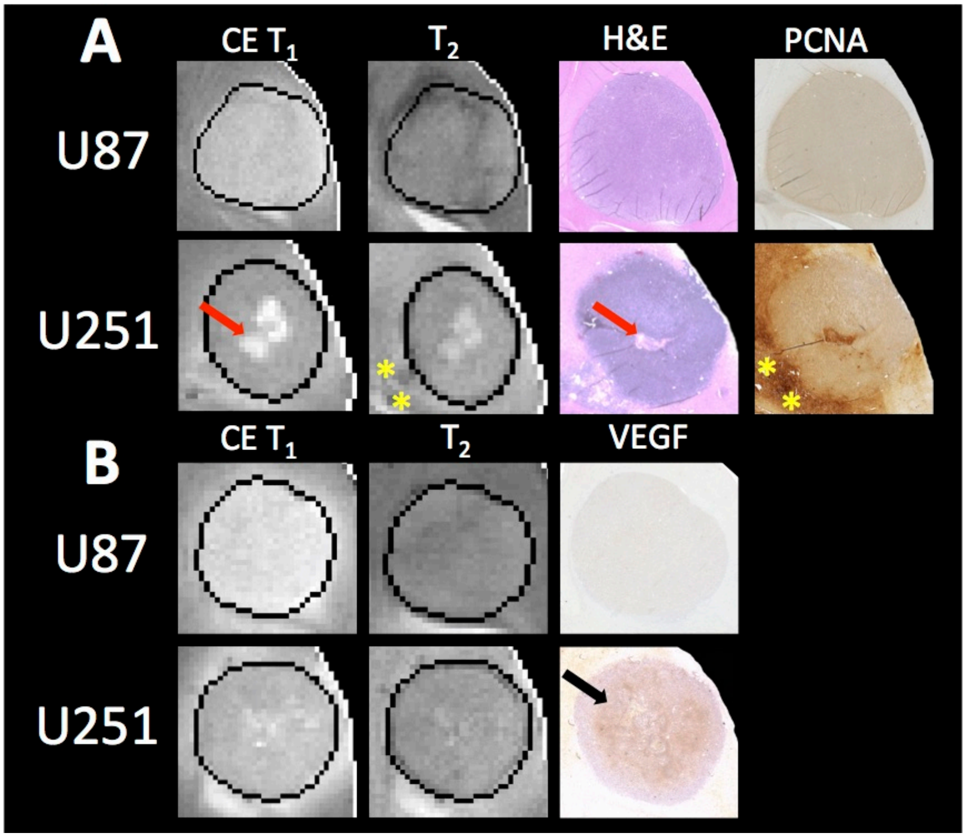

Figure 4.7. MRI and pathology comparisons for U87 and U251 tumors. (A) Contrast enhanced (CE) T_1-weighted and T_2 weighted MRI along with H&E staining and PCNA IHC are shown for example U87 and U251 tumors. Necrotic regions (red arrows) form in the central regions of U251 tumors as evident on H&E, which corresponds to regions of higher signal intensity on T_1-weighted images where contrast agent accumulates. Necrosis was not observable in U87 tumors. Regions of increased proliferation (yellow stars) are highest on the tumor margins and extend into surrounding tissue in U251 tumors. (B) MRI with corresponding VEGF IHC in U87 and U251 tumors. Increased VEGF was observed in mid-regions of U251 tumors.

4.5 Discussion

U87 and U251 tumors were characterized in terms of their cellularity, vascularity, and metabolism throughout tumor progression with multi-parametric MRI/MRSI methodology. Few longitudinal studies on preclinical glioma models have been performed and normally focus only on one additional imaging contrast.[186-188] The pH_e has been monitored longitudinally in C6 glioma models and results show only small changes in the pH_e with tumor progression.[189] In this prior study, pH_e was measured using hyperpolarized bicarbonate ^{13}C MRSI and the intracellular pH was measured using a ratiometric chemical exchange saturation transfer (CEST) approach termed AACID. Here we show that pH_e in both U87 and U251 tumors also remained relatively stable throughout tumor growth. The acidic microenvironment, with pH_e values ranging from 6.1 to 6.8, developed by the initial timepoint early during tumor progression and remained homogenous. However, U251 tumors were found to be slightly more acidic, suggesting that U87 tumors are metabolically less glycolytic.

During tumor progression, spatiotemporal patterns of parametric values were distinct for both U87 and U251 tumors, indicating differences in tumor architecture, vascularity, and metabolism. Unique tumor growth patterns were evident between U87 and U251 tumors, with U87 tumors growing to twice the tumor volumes of U251 tumors at the final time point. While F_p, K^{trans}, and v_p heterogeneity increased with tumor growth, these changes were more pronounced for U251 tumors. Although K^{trans} remained lowest at the tumor margin of both tumors, well-perfused regions developed in central tumor regions between the periphery and core with U87 tumors exhibiting higher F_p. Although there was no change in average values for v_e and ADC with progression, regions with reduced v_e

corresponded well with lower ADC (higher cellularity) in U87 tumors; for U251 tumors, regions with higher v_e and higher ADC were observed in the core suggesting development of necrosis.

Despite U87 and U251 tumors being extensively used in the literature, different growth patterns are evident in many reports.[24,26,190] Differences in time to tumor formation results from the difficulty of injecting large numbers of cells in small volumes. A larger number of cells ($5x10^5$ cells in 5 μL) are injected for the U251 model compared to U87 ($2x10^5$ cells in 5 μL) and the variation in time to tumor formation is much greater. Additionally, U251 tumors do not appear as a uniform mass early during tumor growth, making detection more difficult and therefore the first scan more variable. U251 tumors are also smaller than U87 tumors at the time of final scan due to development of neurological symptoms at smaller tumor volumes in U251 tumors.

The size of the tumor based on contrast enhancement depends on the time from contrast agent administration until measurement. Previous work comparing the tumor size from contrast-enhanced imaging revealed the difference in size based on the time from contrast administration with differences observed up to 30% greater at late time points.[191] Although late enhancement T_1-weighted images were acquired, the volume was calculated based on demarcation of the tumor margin on T_2-weighted images for consistent measurements between the tumor types. Additionally, the DCE was acquired in only three 1-mm slices, which in small tumors would cover the entirety of the tumor and could be used for volume measurement. However, in larger tumors, a greater number of slices was required for full 3D coverage of the tumor. For this reason, the 7 slices of the T_2-weighted images were used for tumor volume measurements.

The measurements from DCE-MRI reflect the extent of contrast agent extravasation and washout from the tumor and relate these changes to local perfusion and vascular permeability. Both U87 and U251 are well-vascularized tumors. Well-perfused regions (F_p) developed between the periphery and tumor core with U87 tumors exhibiting higher perfusion rates, but permeability (K^{trans}) remained lowest at the tumor margin for both tumors. A high interstitial volume fraction (v_e) in the central regions of U251 tumors reflected the development of necrosis. Additionally, this is correlated with increases in T_2 and ADC reflective of increased free water that would be present in necrosis. Interestingly tumor progression showed correlated changes between extracellular space (v_e) and tissue cellularity (ADC). For U87 tumors, regions with reduced v_e corresponded well with lower ADC (higher cellularity), whereas for U251 regions with higher v_e and higher ADC were seen in the core suggesting development of necrosis.

Histology was used to validate the presence of necrosis development in U251 tumors. Central regions of U251 tumors had reduced cellularity as reflected by decreased hematoxylin staining on H&E; however, U87 tumors showed no evidence of necrosis. Necrotic areas on H&E corresponded to regions of higher ADC and increased v_e also suggestive of reduced cellularity as expected with necrosis. While both U87 and U251 are positive for PCNA, as validated with IHC, U251 has much greater proliferation at the tumor margin. Further, PCNA is expressed at high levels in peritumoral tissue in U251 tumors indicative of proliferative cells outside of the demarcated tumor boundary.

VEGF IHC staining revealed increased angiogenesis in the mid-regions of U251 tumors that was not seen in U87 tumors. VEGF expression is regulated by hypoxia which promotes angiogenesis and an increase in vascular permeability.[37] U87 has higher perfusion throughout the tumor (increased F_p), which is supported by the lack of VEGF staining. Future studies should validate this hypothesis using pimonidazole to stain for hypoxia. U251 tumors have lower F_p and higher vascular permeability (K^{trans}) in mid-regions of the tumor (between the margin and center of the tumor) compared to U87 tumors, which is supported by increased VEGF staining.

The acidic microenvironment (pH_e 6.1-6.8) developed early during tumor progression and remained homogenous. U251 tumors were more acidic, suggesting higher glycolytic metabolism in U251 than U87 tumors. Although the pH_e remains stable or slightly increases at late time points in U87 tumors, the volume that is acidified is exponentially larger, indicating significant changes in metabolic output (possibly due to increasing number of cancer cells) despite the small variations in pH_e. Given that the pH_e remains acidic at the tumor margin, further characterization of the pH_e changes in the peritumoral regions may shed insights into parenchymal transformation as well as the role of surrounding stroma on tumor growth. U87 has a well demarcated tumor margin that remains well defined throughout tumor progression indicating minimal invasion into the surrounding tissue. In contrast, U251 tumors have a poorly defined tumor margin, contrast leaks into the surrounding tissue, and ADC and T_2 values are higher in the peritumoral region, making measuring spatial variations in pH_e at the tumor margin important for characterizing tumor invasion into surrounding tissue. However, pH_e distributions remain homogenous throughout tumor progression and a stable marker of tumor metabolic output.

Our surface fitting ignored which tumor was associated with which animal, and instead used tumor volume as a longitudinal progression proxy, rather than time of progression in each animal. This was significant for several reasons. Firstly, determine the starting point for each tumor was infeasible due to tumor variability. Additionally, again due to tumor heterogeneity, tumor progression did not occur at a same or predictable pace for each animal. And finally, combining data from different animals allowed for the elucidation of more universal and robust trends for the different tumor lines rather than a focus on animal to animal tumor variations.

Our surface fitting analysis is powerful as it is able to reveal simultaneous patterns and trends in both the temporal dimension (with tumor progression and increase in tumor volume) as well as the spatial dimension (distance to tumor boundary). However, the extraction of rich results (fitted surfaces in our case) from any given data comes at the potential tradeoff of overfitting, thus requiring optimal design choices. One of these was the degree of polynomial fitting. We chose to fit our surfaces to second degree (quadratic) surfaces. Our data showed consistent quadratic relationships across different animals and parameters, making a linear model inappropriate, and giving confidence in our choice of a quadratic model. The lack of any discernable higher order patterns made any higher order polynomials (cubic or higher) susceptible to overfitting and inappropriate for our analysis.

Our data is not a random sampling of voxels from across an inordinate number of tumors, but rather is a collection of many voxels from single tumors in multiple animals. While data from multiple tumors and animals were used, all the voxels from each tumor, being from the same tumor, would naturally show some correlation. We have more datapoints across a range of distances from tumor boundary that across a range of tumor progressions/time points/tumor volumes. The result of this is that trends along the "distance to tumor boundary" will be more robust that trends along the tumor progression/tumor volume axes, and it should also be noted that quadratic fitting could be skewed by an outsized impact from tumors that are both of unusually large size and that violate the normal tumor line trends. While this was a potential limitation, visual inspection of the data did not indicate this to be the case and showed good interpolation between tumor volumes, and argues for the merits of the analysis which has been possible here.

Given tumor heterogeneity, and the presence of small amounts of "outlier" tissues such as blood vessels, we used an automatic outlier removal (or more accurately, an outlier weighting) robust regression algorithm for our fitting. We chose the Bisquare algorithm as it is a standard algorithm. However, to check robustness to choice of outlier removal, we also analyzed our data with the Least absolute residuals (LAR) robust regression algorithm. Our trends did not change, giving confidence that our outlier algorithm did not introduce any processing artefacts into the results.

Several previous limitations of the BIRDS method for measuring pH_e were addressed in this study. For the first time, pH_e is reported at multiple depths within the tumor from the 3D dataset allowing for spatial pH_e characterization throughout a larger region of the tumor. Additionally, while we have previously shown that the use of probenecid did increase tissue concentrations of $TmDOTP^{5-}$,[135] this study presents the first application of longitudinal pH_e mapping using BIRDS. Although the ADC/DCE and BIRDS datasets were acquired with different RF coils, animal positioning was standardized to ensure that the same regions were imaged in both datasets and were acquired in the same imaging session. The slices used from the BIRDS dataset were acquired with the same thickness as for the ADC and DCE measurements such that they represent similar tumor regions. Although minor rotations in the animal positioning prevent the slices acquired from the two methods to exactly overlap, they represent the same tumor depths and spatial orientation. The tumor was masked independently in the DCE and BIRDS dataset to account for these small discrepancies in positioning. Future use of a RF coil design that simultaneously captures the DCE and BIRDS data would resolve these concerns. While probenecid is used clinically although not in this context, $TmDOTP^{5-}$ is not approved for clinical use. However, transition metal probes with similar pH sensitivities are being developed to increase translatability. Additionally, BIRDS can be used in preclinical models to validate other pH sensing methodologies. Further, BIRDS has recently been implemented on clinical 3T MRI scanners using a rabbit model of liver cancer[181,182] showing that the method is translatable to clinical MR scanners.

4.6 Conclusion

Vascular, cellular, and metabolic imaging provides rich information on the microenvironment during tumor progression in GBM. For example, although U87 tumors grew two times faster, U251 tumors were more aggressive as indicated by their prolonged and reduced perfusion and pH_e, a combination of which could be related to necrotic cores. In addition to changing morphologic architecture and cellularity, the tumor vascular microenvironment showed a reduction in extracellular volume, increased plasma flow, and greater heterogeneity throughout tumor progression. Using a combination of probenecid and $TmDOTP^{5-}$ allows for successful longitudinal BIRDS pH_e quantification. Interestingly, despite the morphologic and vascular remodeling, metabolic output remains stable and equivalently glycolytic as evident by constant pH_e, with the acidic microenvironment developing early in tumor growth and remaining acidic during tumor progression. This suggests the potential of pH_e as a biomarker of tumor metabolism that is independent of tumor size and may in future studies be used to monitor treatment response. The dynamic processes regulating transformation of the tumor microenvironment suggests tumor characteristics that must be considered for targeted therapies and where the homogeneity of pH_e during tumor progression may prove useful for evaluating therapeutic responses in the context of heterogeneous and changing relaxation, diffusion, and vascular parameters.

Chapter 5: Normalization of the Intratumoral Extracellular pH as a Biomarker of Therapeutic Response

5.1 Abstract

As seen in Chapter 4, gliomas maintain an acidic extracellular pH (pH_e), which promotes tumor growth and builds resistance to therapy. Given evidence that acidic pH_e beyond the tumor core indicates infiltration, we hypothesized that imaging the intratumoral pH_e in relation to the peritumoral pH_e can provide a novel readout of therapeutic influence on the tumor microenvironment. We used Biosensor Imaging of Redundant Deviation in Shifts (BIRDS) to generate pH_e maps in rat brains bearing either U251 or U87 tumors. Following $TmDOTP^{5-}$ infusion, the MRI delineated tumor boundary was identified and BIRDS was used to image the pH_e gradient between intratumoral and peritumoral regions (ΔpH_e) in both untreated and temozolomide treated (40 mg/kg) rats bearing U251 tumors. Treated rats had reduced tumor volume ($p<0.01$), reduced proliferation (Ki-67 staining; $p<0.03$) and apoptosis induction (cleaved Caspase-3 staining; $p<0.001$) when compared to untreated rats. The ΔpH_e was significantly higher in untreated compared to treated rats ($p<0.002$), suggesting that temozolomide, which induces apoptosis and hinders proliferation, also normalizes intratumoral pH_e. We also used BIRDS for longitudinal pH_e mapping in rats treated with sorafenib, a tyrosine kinase inhibitor. Treated U87 tumors displayed slower tumor growth and increased pH_e ($p=0.01$) within 4 days of starting therapy; however, sorafenib-treated tumors exhibited reduced agent extravasation. In summary, BIRDS can be used to map the ΔpH_e in gliomas and provide a physiological readout of the therapeutic

response on the tumor microenvironment. All temozolomide work in this chapter has been previously published and is used with permission.[142]

5.2 Introduction

Gliomas account for more than 80% of all malignant brain tumors with most patients progressing to highly malignant grade IV glioblastomas (GBMs). Patients with GBMs have a median survival of ~12 months with only 3–5% of patients surviving for more than 3 years.[1] Surgical resection and radiation therapy, together with adjuvant chemotherapy (e.g., temozolomide (TMZ)), is currently used to treat GBMs clinically with magnetic resonance imaging (MRI) playing a central role in initial diagnosis and treatment monitoring. Although TMZ prolongs survival, chemoresistance and recurrence are common.[18] Temozolomide is an alkylating agent that directly damages DNA and results in cell cycle arrest and apoptosis;[19] however resistance to temozolomide arises by the presence of O6-methylguanine DNA methyltransferase that is able to repair DNA methylation damage. Despite temozolomide being the only approved chemotherapeutic agent to show a survival benefit, anti-angiogenic agents including both the anti-VEGF monoclonal antibody bevacizumab and a variety of small molecule tyrosine kinase inhibitors (TKIs) have shown some promise. While bevacizumab has shown a benefit in progression-free survival, anti-angiogenic agents induce changes in tumor vasculature that alters appearance on MRI despite little change in tumor architecture leading to a pseudoresponse.[192]

Thus, having reliable markers and methods to assess therapeutic response is of extreme importance for seeking alternative treatment routes. In this context, imaging extracellular pH (pH_e) has gained importance. A shared trait among cancers is the metabolic shift from oxidative phosphorylation to glycolysis (Warburg effect), which leads to increased acidification of the extracellular milieu as tumor cells extrude H^+ and lactate, produced as a result of increased glycolysis.[193] Since TMZ induces apoptosis and given the cancer-induced metabolic shift, we posit decreased aerobic glycolysis of treated tumor cells can be reflected as increased intratumoral pH_e.

Biosensor Imaging of Redundant Deviation in Shifts (BIRDS) is a 3D chemical shift imaging (CSI) platform where paramagnetically-shifted non-exchangeable protons on (-DOTA) based macrocyclic complexes are directly detected. The proton shifts provide a readout of the physicochemical environment and the signal does not depend on diffusion or blood flow.[133,136,141] Here we use BIRDS, which is an attractive alternative MR method for molecular imaging, to evaluate therapeutic efficacy in U251 and U87 human-derived glioma models. First, we evaluate effects of TMZ in U251 gliomas by measuring pH_e inside and outside the tumor boundary after TMZ treatment. Second, we show the effects of a TKI (sorafenib) on the longitudinal progression of both tumor vasculature and pH_e (before and after treatment) in U87 tumors.

5.3 Materials and methods

Experiments were performed according to NIH guidelines. Yale University's animal care and use committee (IACUC) approved the protocol. U251 scans were conducted on an Agilent (Santa Clara, CA) 11.7T horizontal-bore spectrometer, using a ^1H surface radio-frequency (RF) coil (1.4 cm diameter). U87 scans were conducted on the same system but operating Bruker (Billerica, MA) software and using a transmit/receive coil in addition to the same surface coil. $TmDOTP^{5-}$ (1,4,7,10-tetraazacyclododecane-1,4,7,10-

tetrakis(methylene phosphonate) complexed with thulium) was purchased from Macrocyclics (Dallas, TX, USA), Gadobutrol was obtained from Bayer (Whippany, NJ, USA), TMZ was obtained from Sigma-Aldrich (St. Louis, MO, USA) and sorafenib was obtained from AK Scientific (Union City, CA). U87 and U251 cells were purchased from American Type Culture Collections (Manassas, VA, USA).

5.3.1 Preparation and treatment of rats bearing U251 or U87 tumors

U251 and U87 cells were grown and prepared as described in Chapters 3. In brief, cells were maintained in standard culture and harvested at high confluence. Adult, female athymic nude rats (200-250 g; n =19), maintained according to approved animal care protocols, were anesthetized with isoflurane (2-3%) and positioned in a stereotaxic instrument. Cells were washed and suspended in serum-free media and a 5 μL volume of the cell suspension (100,000 cells/μL for U251, 40,000 cells/μL for U87) was injected intrathalamically (U251, n=11; U87, n=8). For U251 tumors, starting at twelve to fourteen days post injection, TMZ (40 mg/kg) was orally administered daily in 5 rats, in 2 cycles of 4 days each with a gap of 2 days in between the cycles. In both treated (n = 5) and untreated (n = 6) U251 tumors, the glioma volume was measured by contrast-enhanced MRI. At the end of chemotherapy (22-24 days post injection), pH_e was measured using BIRDS. In U87 tumors, baseline imaging was performed 10 days after tumor cell inoculation. Animals were randomized into treated (n=4) or control (n=4) groups. Starting at day 11, sorafenib (100 mg/kg) was administered via oral gavage daily until terminal imaging. MR imaging was repeated at day 15 and day 19, providing for two additional timepoints after the start of therapy. At all time points, tumor volume was measured using T_2-weighted and contrast-enhanced T_1-weighted imaging and pH_e was measured using BIRDS. Since sorafenib targets tumor vascularity, additional imaging was performed to measure parameters of tumor vascularity using dynamic contrast enhanced (DCE) MRI.

5.3.2 U251 Tumor volume and acidity measurements by MRI

Tumor volume was measured with Gadobutrol and $TmDOTP^{5-}$ inducing longitudinal (T_1) and transverse (T_2) relaxation enhancements, respectively, by MRI. Spin-echo images with 128×128 in-plane resolution, 1 mm slice thickness and field of view (FOV) of 25×25 mm^2, recycle time (TR) of 4 s, and echo time (TE) of 7 ms. These parameters give an in-plane resolution of 0.195×0.195 mm^2 and voxel size of 0.038 mm^3, i.e., parameters which are sufficient for defining tumors of 1 mm^3. Although we used T_1 and T_2 agents (i.e., Gd^{3+} and Tm^{3+}, respectively) in our study to assess tumor sizes, previous work has shown that Gd^{3+} and Dy^{3+} extravasation in the same subject identify the same tumor boundary.[88] The tumor volume was calculated from the difference in the MR image intensity in all MR slices before and after contrast agent (either Gadobutrol or $TmDOTP^{5-}$) injection. The absolute intensity difference before and after contrast agent was divided by the image intensity before contrast agent injection to obtain a relative change in the intensity. The volume of the tumor was assumed to be equal to the volume of the region where the relative intensity change is larger than a threshold value, established by comparison with the relative intensity change measured in the contralateral (left) hemisphere.

At 12-14 days after tumor inoculation (~2 weeks), an infusion line was established in the lateral tail vein of the rat. A 30G needle was inserted into PE10 (Braintree Scientific, LLC) line and filled with heparinized saline. The needle was inserted into the lateral tail vein of the rat and checked for backflow to ensure correct placement within the vein, prior to being anchored to the tail with tape. Each rat underwent bolus injection of Gadobutrol (~0.4 mmol/kg) to estimate the tumor volume from increased MRI signal (T_1 contrast) due to Gadobutrol extravasation.

At 22-24 days after tumor inoculation (~3 weeks) each rat underwent infusion of $TmDOTP^{5-}$ (~0.4 mmol/kg) for pH_e imaging and the tumor volume was estimated from decreased MRI signal (T_2 contrast) due to $TmDOTP^{5-}$ extravasation.[141] The anesthetized rats were prepared as described earlier with renal ligation to maintain a high concentration of $TmDOTP^{5-}$ (slowly infused at 0.5-0.7 mL/hr using a syringe pump) during BIRDS experiments.[194,195] Ventilation was adjusted to maintain normal physiology. Body temperature was measured with a rectal probe and no further adjustments in the water-heated pad were made for the entire duration of the experiment (~2 hrs).

Tumor acidity was measured using the BIRDS technique described previously.[133,134,141] In short, chemical shift imaging (CSI) for BIRDS was performed to measure the chemical shifts of the pH_e-dependent proton resonances of $TmDOTP^{5-}$ to calculate pH_e within each voxel at an isotropic resolution of $1mm^3$. A 205 μs dual-banded Shinnar-Le Reux pulse with a bandwidth of 40kHz was used for excitation of the H2, H3, and H6 resonances of $TmDOTP^{5-}$. pH_e was calculated in each voxel using BIRDS as previously described.[141]

5.3.3 Histopathological study of effect of TMZ therapy

Post experiment, rats were perfuse-fixed with 4% paraformaldehyde and embedded in paraffin. Brain tissue sections (6 μm) were immunohistochemically stained for Ki-67 and cleaved Caspase-3 as previously described.[196] Primary antibody diluted in 1% BSA/PBS was applied overnight at 4 °C for Ki-67 (1:25, Abcam, ab66155) and Caspase-3 (1:25, Cell Signaling Technology, #9661). The sections were incubated with a goat anti-rabbit secondary antibody (1:500, Pierce, #31460) for 60 minutes followed by incubation with metal enhanced 3,3-diaminobenzidine (DAB; Life technologies, #34065) for 10 min. Expression of immunohistochemical markers was quantified by evaluating the presence of DAB staining and visually quantifying positive staining.

5.3.4 U87 Tumor volume, vascular, and acidity measurements by MRI

Quantitative T_2 mapping was performed by acquiring T_2-weighted images with 10 TE 10-100ms, TR of 6 s, slice thickness 1 mm, 25 × 25 mm FOV, 128 × 128 matrix. Diffusion-weighted imaging was performed using an EPI sequence with 6 b values (0-3000 s/mm^2) in a single direction and acquired with slice thickness 1 mm, 25 × 25 mm FOV, 64 × 64 matrix. Quantitative T_1 mapping consisted of T_1-weighted images acquired using a RARE sequence with TE 10ms, 5 TR (400-8000ms), slice thickness 0.7mm with 0.3mm gap, 25 × 25 mm FOV, 128 × 128 matrix. The T_1 sequence was then repeated after 0.25 mmol/kg gadoterate meglumine (Dotarem) administration to serve as a post-contrast image which was used, along with T_2 images, to delineate tumor boundaries. A contrast enhanced T_1-weighted 3D FLASH was also acquired with TE 5ms, TR 30ms, and 0.33mm isotropic resolution for high-resolution coverage of the entire tumor for coregistration.

DCE-MRI was acquired using a dual-echo spoiled gradient echo acquisition (TR/TE: 39ms/2.5-5ms) every 5 seconds over 22 min. At 2 min into the dynamic scan, a bolus IV injection of 0.25mmol/kg Dotarem, a clinically available macrocyclic gadolinium agent, was injected and then flushed with heparinized saline. Other imaging parameters included a flip angle of 15^o and one average for a temporal resolution of 5 s. Three central slices of the tumor were chosen with the exact same positioning, FOV (25 × 25 mm), and matrix (128 × 128) to be co-registered to the T_1 data. Measurements from pre-contrast T_1-weighted images were used to transform the signal time-intensity curves into time-concentration curves (TCCs). The arterial input function (AIF) was measured by collecting arterial blood samples at discrete time points post-injection in a representative animal. A hematocrit of 0.45 was assumed for deriving the contrast agent concentration in the blood. The raw AIF was fit to a bi-exponential curve and applied to the analysis for all datasets. A region of interest (ROI) was placed in the tumor, which was the area used for all analyses. To measure vascular parameters [K^{trans} (volume transfer coefficient, min^{-1}), F_p (plasma flow rate, min^{-1}), v_e (extracellular volume fraction, unitless), v_p (plasma volume fraction, unitless)], a two-compartment exchange model (2XCM) was used to fit the DCE data. The parameters were estimated by fitting each voxel using least squares regression using prior software.[185]

Prior to the start of pH mapping, the animal was removed from the magnet bore and transferred to a 1.5 cm single loop surface coil. For BIRDS pH_e measurements, 100 mg/kg probenecid was administered over 10 min and followed after 20 min by a coinfusion of 100 mg/kg probenecid and 1 mmol/kg $TmDOTP^{5-}$. Probenecid was used to increase the plasma concentration of the circulating contrast agent and reduce its rate of renal clearance. All infusions were performed using a syringe pump at a rate of 15 μL/min for a total infusion time of 100 min. Chemical shift imaging began 45 min after the start of the infusion. All acquisition parameters were the same as those used for U251 tumors. Quantitative T_2 mapping was performed for tumor localization as described earlier.

5.3.5 Statistics

T_1, T_2, and ADC parameters were generated by fitting voxel-level data to a monoexponential function in Matlab. All DCE vascular parameters and pH_e by BIRDS were quantified on a voxel by voxel basis and spatially plotted in Matlab overlaid on T_2-weigheted images. All parameters were averaged across the tumor ROI. All staining, tumor size and pH_e results were expressed as mean ± SD and comparisons between groups were assessed by Student's t-test with two tails where $p<0.05$ was considered significant.

5.4 Results

5.4.1 Effect of TMZ on tumor size, apoptosis, and proliferation

Tumor size was measured by MRI contrasts generated from water proton longitudinal (T_1) and transverse (T_2) relaxation enhancements. The effect of TMZ on U251 tumor growth was assessed by measuring the tumor volume at ~2 weeks (i.e., 12-14 days using T_1-enhanced contrast by Gadobutrol) and ~3 weeks (i.e., 22-24 days using T_2-enhanced contrast by $TmDOTP^{5-}$) post tumor inoculation (**Figure 5.1A**). In the treated group, the rats were imaged at 12.6±0.5 and 22.8±0.7 days, whereas in the untreated group the rats were imaged at 12.4±2.2 and 22.0±3.3 days. Recent experiments indicate that tumor volumes measured with a T_1 agent (e.g. Gadobutrol) are nearly identical with those measured using a T_2 agent (e.g. $TmDOTP^{5-}$) in the same rat.[88] Ambiguity exists in delineating tumors in clinical images with ill-defined tumor boundaries. However, U251 tumors in rodents have a tumor mass with fairly well-defined boundary. Thus, ambiguity in tumor boundaries has minimal effect on the tumor volume measurements compared to clinical scans. The volume of untreated tumors at 2 weeks post tumor inoculation was 5.9±2.7 μL, which increased to 25.3±13.9 μL at 3 weeks. Treated tumors had similar volumes at 2 weeks (5.2±1.2 μL) and 3 weeks (3.9±0.9 μL) (**Figures 5.1A** and **5.1B**). Thus, tumor sizes were significantly different in treated vs. untreated animals at later stages of tumor growth ($p<0.01$) and there was no further tumor growth with therapy.

Expression of Ki-67 and cleaved Caspase-3, shown in **Figure 5.1C-E**, was investigated in treated and untreated rats. Quantitative analysis revealed that the average Ki-67 labeling before TMZ treatment was 67.5%, which reduced to 10.5% following TMZ treatment ($p<0.03$) indicative of reduced proliferation. Cleaved Caspase-3 staining before TMZ treatment was 2.5%, which increased to 15.5% following TMZ treatment ($p<0.001$) suggesting apoptosis initiation. Expression of MCT-4 was analyzed in a representative sample of untreated and treated tumors and high MCT-4 expression was observed in untreated tumors (**Figure 5.1F**).

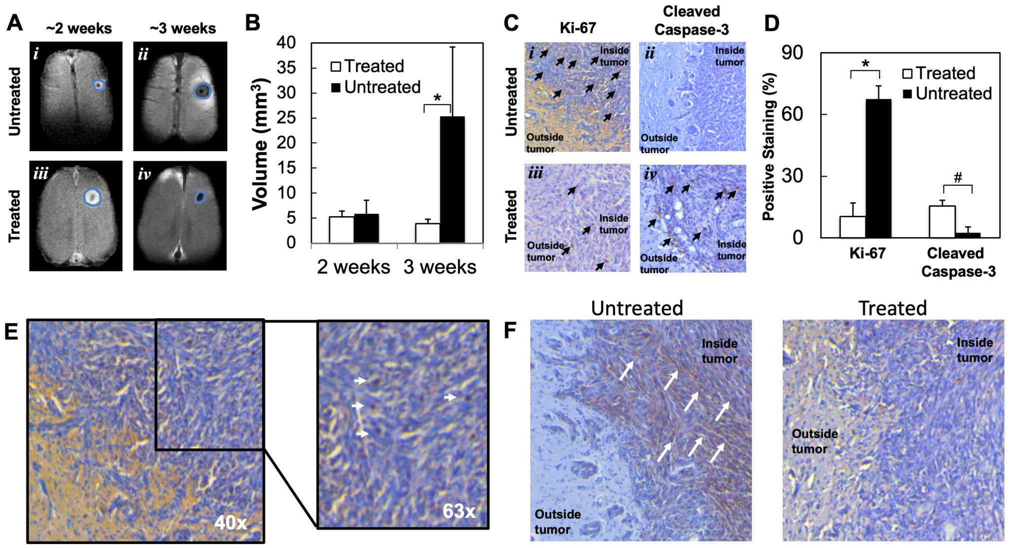

Figure 5.1. Effect of TMZ treatment on U251 tumor morphology, apoptosis, and proliferation. (A) T_1- and T_2-weighted MRI at ~2 and ~3 weeks post tumor implantation, respectively, depicting tumor sizes in untreated and TMZ treated U251 tumors. (B) Tumor volume in treated and untreated U251 bearing rats at ~2 and ~3 weeks post tumor implantation, where the difference between treated and untreated groups were significant at later stages (*, p=0.01). (C) Ki-67 and cleaved caspase-3 staining in untreated and TMZ treated U251 tumor bearing rats. Arrows point to brown colored positive DAB staining. (D) Percentage of cells showing positive staining for Ki-67 and Cleaved Caspase-3. In treated vs. untreated tumors, Ki-67 shows a significant decrease in proliferative index (*, p=0.025) and cleaved caspase-3 shows a significant increase in apoptotic index (#, p=0.001). (E) High magnification Ki-67 staining of untreated U251 tumors. The arrows point to positive DAB staining for Ki-67 where co-localization with hematoxylin (blue) is clearly visible. (F) MCT-4 staining of treated and untreated U251 tumors with arrow marks pointing to positive DAB staining for MCT-4.

5.4.2 Effect of TMZ on intratumoral and peritumoral acidity

Representative BIRDS data from untreated and treated rats are shown in **Figure 5.2**. The tumors were localized by T_2 contrast as a result of $TmDOTP^{5-}$ extravasation from immature tumor vasculature.[133,135] Treated tumors appeared smaller in size compared to untreated tumors (**Figures 5.2A (i)** and **5.2B (i)**; see also **Figures 5.1A** and **5.1B**). The proton resonances of $TmDOTP^{5-}$ in the corresponding imaging slice are shown in **Figures 5.2A(ii)** and **5.2B (ii)**. As the permeability and clearance rates of $TmDOTP^{5-}$ vary in different tissues, the peak intensities vary across the different regions in the image. As reported previously,[141] BIRDS can distinguish pH_e maps for tumors of different sizes, and both the intratumoral pH_e (inside tumor boundary) and peritumoral pH_e (outside tumor boundary) can be measured simultaneously. The intratumoral pH_e values for the untreated and treated tumors were ~6.8 and ~7.1, respectively (**Figures 5.2A (iii)** and **5.2B (iii)**). However, the peritumoral pH_e values quite distal from the tumor boundary for the untreated and treated tumors were approaching neutral values (i.e., ~7.2 and ~7.3, respectively in **Figures 5.2A (iii)** and **5.2B (iii)**). It should be noted, however, that acidic peritumoral pH_e values were observed immediately adjacent to the tumor boundary in untreated tumors. This is supported by greater Ki-67 expression in untreated rats when compared to treated rats (**Figures 5.1C** and **5.1D**). This trend of acidic peritumoral pH_e immediately adjacent to the tumor boundary has been observed for other aggressive gliomas.[135,141]

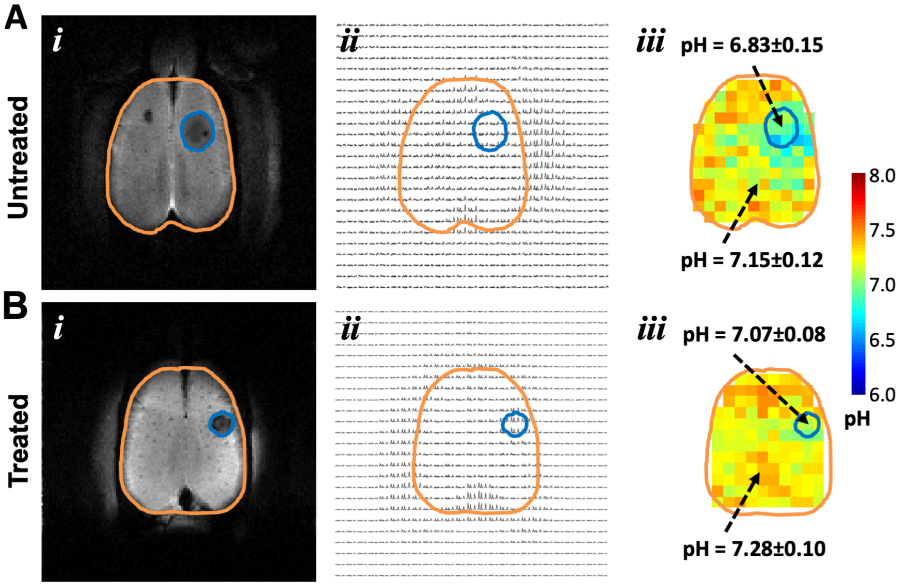

Figure 5.2. Representative pH_e maps from BIRDS in untreated and TMZ treated rats bearing U251 tumors. (i) The T_2-weighted images identify the tumor boundary (tumor = blue outline; brain = orange outline) in untreated (A) and temozolomide treated (B) U251 tumors. (ii) CSI data for corresponding slice in (i) shows varying $TmDOTP^{5-}$ levels throughout the brain. (iii) Quantitative pH_e maps were obtained using multiple $TmDOTP^{5-}$ peaks and the intratumoral and peritumoral pH_e average values and their standard deviations are indicated. In untreated rats, the tumor is larger, the intratumoral pH_e is acidic and spreads beyond the tumor boundary. In treated rats, the tumor is smaller, the intratumoral pH_e is near neutral with lower pH_e localized within the tumor boundary.

Because the spatial resolution of pH_e maps was lower than that of MR images, we took precautions to report the intratumoral and peritumoral pH_e values accurately. In small tumors, where many voxels intersect the tumor boundary defined by MRI, partial contribution from the non-tumor area can confound the results. Thus, voxels that contained more than 50% tumor tissue were considered tumor voxels resulting in at least 2 tumor voxels in the smallest tumors detected.

The intratumoral and peritumoral pH_e values for untreated and treated tumors are represented in histograms in **Figure 5.3A** and **5.3B**, respectively. The histograms were fitted to a Gaussian distribution to obtain the most probable pH_e and the full width at half maximum (FWHM) of these histograms. The most probable intratumoral pH_e values were higher in treated when compared to untreated tumors. The FWHM values of untreated tumors (~0.4) were higher than treated tumors (~0.3), indicating heterogeneous pH_e in untreated rats, which is normalized by TMZ in treated rats. **Figure 5.3C** shows the average values of intratumoral and peritumoral pH_e in treated and untreated rats. Average intratumoral pH_e was significantly ($p<0.01$) lower in untreated rats compared to treated rats, whereas in peritumoral regions no significant difference ($p>0.05$) was observed between the two groups.

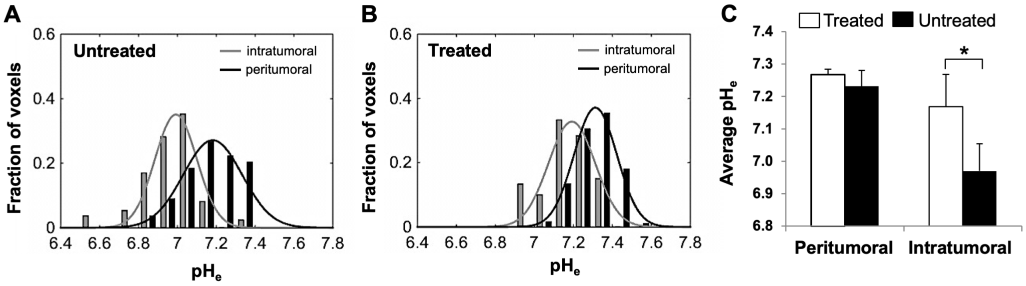

Figure 5.3. Distribution of pH_e values in untreated and temozolomide treated tumors. Intratumoral (gray bars) and peritumoral (black bars) regions are shown for untreated (A) and TMZ treated (B) U251 tumors. Average pH_e values (±SD) for intratumoral and peritumoral regions in untreated and TMZ treated U251 tumors (C) show that the average pH_e value for intratumoral voxels is significantly lower in untreated tumors compared to treated tumors (*, p=0.001).

To investigate how pH_e is affected in voxels positioned at different distances relative to the center of mass of the tumor, the brain was separated into regions of interest (ROIs) starting from the center of the tumor and progressing outwards in concentric 1 mm circles (**Figure 5.4A**). The boundaries between the intratumoral and the peritumoral regions (shown with white and black arrows for the treated and untreated groups, respectively, in **Figure 5.4B**) were calculated from the average tumor volume obtained from the anatomical MR images (**Figure 5.1B**), assuming a spherical tumor shape. Lower pH_e values were observed in the intratumoral regions (ROIs 1 and 2) in the untreated group (**Figure 5.4B**). In the treated group, the pH_e values in the intratumoral regions (ROI 1) were partially normalized by TMZ treatment. The lower pH_e value measured in ROI 3 in the untreated group (7.13 ± 0.10) reflects the increased acidity of the tissue surrounding the tumor, as can also be observed in **Figure 5.2**. The treated group, in comparison, has pH_e values of the tissue surrounding the tumor (ROI 2) closer to normal values (7.21 ± 0.04). However, the lower average pH_e value observed for the untreated group in regions surrounding the tumor (ROI 3) might be due to contributions from larger tumors (with lower pH_e). For regions distant from the tumor center (ROIs 4 to 10) the pH_e values are not significantly different between the treated and the untreated groups ($p>0.05$). In addition, heterogeneous pH_e distributions in the untreated rats were suggested by larger SDs in each ROI compared to treated rats, except ROI 1. The larger standard deviation for ROI 1 is most likely due to variations in the temozolomide effect on intratumoral pH_e across different animals. Note that most of the intratumoral regions for the treated group is restricted to ROI 1, based on the tumor boundary estimation described above. The SD for the rest of the ROIs (ROIs 2 to 10) is smaller in the treated group because those ROIs contain mostly normal brain tissue whose pH_e is minimally affected by the temozolomide treatment.

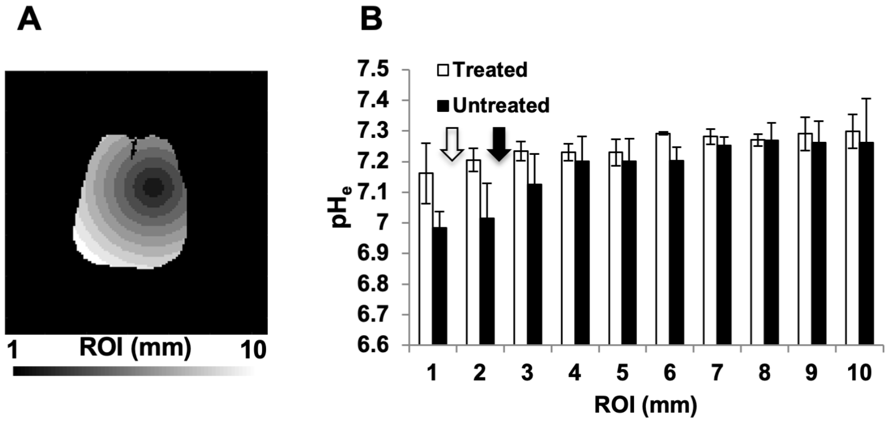

Figure 5.4. Average pH_e values across all animals in various ROIs positioned at increasing distance from the center of mass of the tumor. The T_2 map was used to mask the tumor and determine its center of mass. The brain was then segmented into ROIs (A) defined by the distance from the corresponding voxel to the center of mass of the tumor. Each ROI was defined as the area bounded by two circles of radius n-1 mm to n mm from the center of mass of the tumor (n=1 to 10). The average pH_e value for each animal was calculated from the pH_e values from all the voxels inside each ROI. Then, the average pH_e values and the corresponding standard deviations (indicated as the error bar) across animals were calculated for each ROI (B). The boundaries between the intratumoral and the peritumoral regions (shown with white and black arrows for the treated and untreated groups, respectively) were calculated from the average tumor volume obtained from the anatomical MR images (**Figure 5.1B**), assuming a spherical tumor shape.

5.4.3 Effect of sorafenib on U87 tumor size, MR relaxation, and diffusion

All U87 animals (n=8) had baseline imaging performed at Day 10 after tumor cell inoculation. Sorafenib (n=4) or DMSO control (n=4) was administered starting on Day 11. However, all animals did not complete the full imaging protocol as there were losses during scanning and fast tumor progression in control animals. Control (n=4) and treated (n=3) animals were imaged at a first follow-up (Day 15). Control (n=3) and treated (n=3) animals were imaged again at a second follow-up (Day 19); however, two control animals died at the beginning of imaging and only completed tumor volume measurements. Finally, two treated animals survived and were imaged at Day 26.

Tumor volume was measured by manually outlining tumor boundaries on T_2-weighted and contrast-enhanced T_1-weighted MRI across multiple slices allowing for complete coverage over the entire tumor volume. Representative T_2-weighted images are shown in **Figure 5.5A** before and at multiple time points after therapy in both sorafenib treated and control tumors. Quantitative tumor volumes were similar in treated and control tumors at baseline (15.1 ± 10.2 mm^3 vs. 17.2 ± 10.7 mm^3). However, tumor volumes were lower in treated tumors versus controls at day 15 (35.0 ± 20.8 mm^3 vs. 78.9 ± 66.7 mm^3) and day 19 (58.1 ± 40.1 mm^3 vs. 145.1 ± 91.7 mm^3). Since tumor volume was variable at baseline as seen by large standard deviations resulting in divergent tumor progression, tumor volumes were normalized to the tumor volume at day 10 and are shown in **Figure 5.5B**.

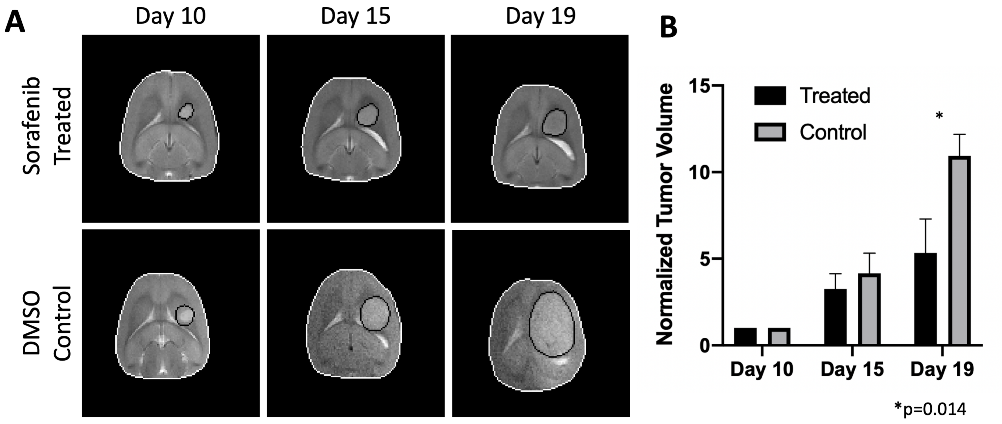

Figure 5.5. Effect of sorafenib treatment on U87 tumor volume and morphology. (A) T_2-weighted MRI at baseline (Day 10), 4 days after start of sorafenib therapy or DMSO control (Day 15), and 8 days after start of sorafenib therapy or DMSO control (Day 19). All timepoints were acquired longitudinally in the same animal and depicted the tumor size in untreated and sorafenib-treated U87 tumors. (B) Normalized tumor volume in treated and untreated U87 bearing rats at baseline and two time points after start of sorafenib therapy or DMSO control, where the difference between treated and untreated groups were significant at the final time point (*, p=0.014).

Quantitative T_1 mapping was performed before and after the administration of a gadolinium contrast agent (Dotarem). Representative T_1-weighted images and quantitative T_1 maps before and after contrast administration are shown in **Figure 5.6A** for both sorafenib and DMSO treated animals. For comparison purposes, only baseline (Day 10) and 4 days post-treatment (Day 15) data are shown in grouped analyses. The intrinsic T_1 was not different between the DMSO and sorafenib groups at baseline (2.33±0.13 s vs. 2.28±0.17 s) or four days after treatment (2.49±0.09 s vs. 2.48±0.13 s); however, the intrinsic T_1 did increase as the tumor grew larger in both groups (**Figure 5.6B**). After administration of the contrast agent, the T_1 decreased in both DMSO and sorafenib groups. At baseline, T_1 decreases were not different between DMSO vs. sorafenib animals (1.46±0.18 s vs. 1.35±0.19 s). However, after four days of treatment initiation, the post-contrast T_1 in DMSO animals was significantly lower (1.24±0.26 s) compared to sorafenib treated animals (1.63±0.06 s) ($p=0.05$) (**Figure 5.6C**). Additionally, the post contrast T_1 values in sorafenib animals continued to increase at later time points, reaching 1.55±0.17 s at eight days post-treatment and 2.02±0.04 s at fifteen days post-treatment; however, T_1 values for DMSO controls are not available for comparison at these later time points since control animals reached their survival endpoints earlier. The increase in T_1 in sorafenib treated rats reflects a decrease in delivery of the contrast agent to the tumor as illustrated by the reduction in contrast in T_1-weighted imaging (**Figure 5.6A**).

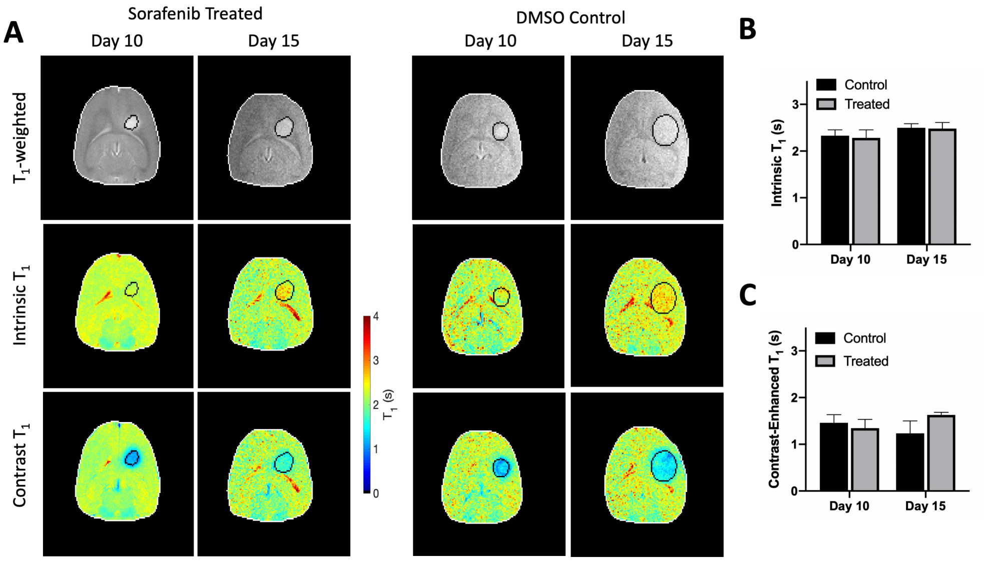

Figure 5.6. Sorafenib reduces the delivery of contrast agents to the tumor and effects T_1 relaxation. (A) Representative T_1-weighted images (TR/TE: 1000/10 ms) are shown at baseline (Day 10) and four days after sorafenib therapy or DMSO control (Day 15). Additionally, quantitative T_1 mapping for the same tumors are shown before (intrinsic) and after (contrast-enhanced) administration of 0.25 mmol/kg of a gadolinium-based contrast agent (Dotarem). In all images the brain is outlined in white and the tumor is outlined in black. (B) Average intrinsic T_1 values for each time point across all tumors. (C) Average contrast-enhanced T_1 values for each time point across all tumors. All values are shown as average ± standard deviation.

DCE-MRI was used to study the vascularity of sorafenib treated U87 tumors. The dynamic data was fit to a two-compartment exchange model that allowed for four vascular parameters to be quantified and spatially mapped across the tumor at multiple time points (**Figure 5.7A**). Due to the limited number of animals and the highly variable parameter values between tumors, no changes were found to reach statistical significance. The K^{trans} was not different between the DMSO and sorafenib groups at baseline (2.33±0.13 s vs. 2.28±0.17 s) or four days after treatment (10.2±2.2 10^{-3}/min vs. 13.8±7.4 10^{-3}/min) (**Figure 5.7B**). At baseline, F_p was more variable between tumors as shown by values for DMSO vs. sorafenib animals (34.8±18.5 10^{-3}/min vs. 53.3±47.5 10^{-3}/min). However, after four days of treatment the F_p in sorafenib animals decreased to 20.7±11.0 10^{-3}/min, whereas it slightly increased in DMSO animals to 57.9±6.3 10^{-3}/min (**Figure 5.7C**). Additionally, the K^{trans} and F_p continued to decrease at later time points; in the sorafenib group the K^{trans} was 3.92±2.43 $10^{-3}min^{-1}$ at eight days post-treatment and 1.60±0.44 $10^{-3}min^{-1}$ at fifteen days post-treatment and F_p was 4.06±2.47 $10^{-3}min^{-1}$ at eight days post-treatment and 2.00±0.42 $10^{-3}min^{-1}$ at fifteen days post-treatment. Similarly, in the sorafenib group the v_e and v_p were also heterogeneous and variable between tumors. There was little change in v_e between baseline and four days after sorafenib treatment (0.17±0.05 vs. 0.10±0.03) (**Figure 5.7D**), which was similarly seen in v_p (0.012±0.012 vs. 0.017±0.007) (**Figure 5.7E**). However, at later timepoints, v_e and v_p increased, respectively, to 0.35±0.10 and 0.045±0.008 at eight days post-treatment and continued to increase to 0.81±0.16 and 0.104±0.004 at fifteen days post-treatment. However, the parameter values based on the two-compartment exchange model are likely biased by the restricted extravasation of the contrast agent into the extracellular space as tumor appearance and architecture on imaging do not suggest a loss of cellularity that would support such a large increase in the extracellular volume fraction.

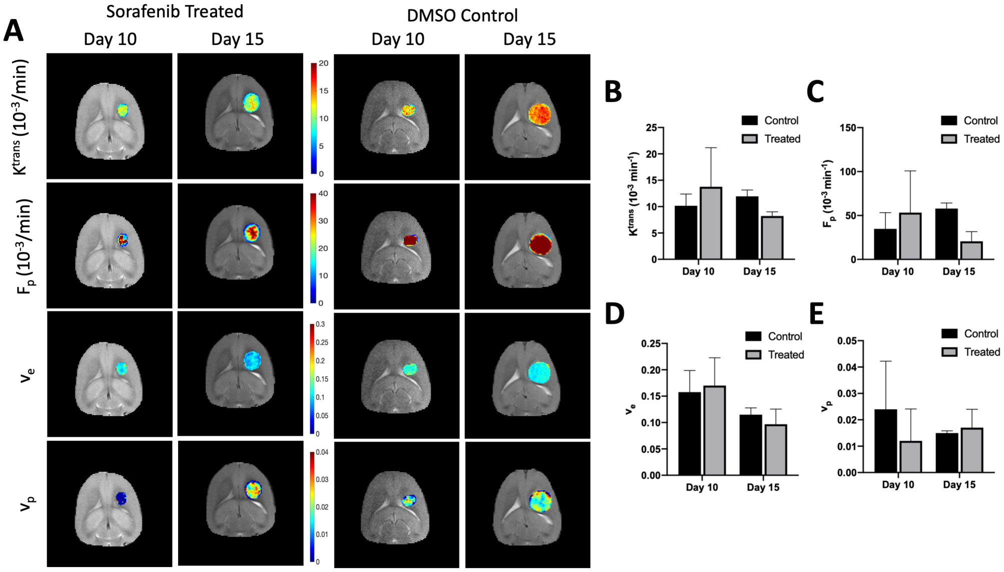

Figure 5.7. Sorafenib effects on tumor vascularity as measured using DCE-MRI. (A) Representative K^{trans}, F_p, v_e and v_p parametric maps are shown at baseline (Day 10) and four days after sorafenib therapy or DMSO control (Day 15). All parametric maps were quantified over the tumor ROI and overlaid on T_2-weighted images (TE/TR: 30/6000 ms) of the entire brain. The two time points were acquired in the same animal. Average K^{trans} (B), F_p (C), v_e (D) and v_p (E) for each time point across all tumors. All values are shown as average ± standard deviation.

Finally, pH_e was measured longitudinally using BIRDS after sorafenib therapy. BIRDS has been precluded from repeated measures of pH_e in the same tumor due to the need for surgical interventions to increase the circulating concentration of the contrast agent ($TmDOTP^{5-}$) as was performed for the TMZ studies in U251 tumors. However, using probenecid, an organic anion transporter inhibitor, sufficient agent is able to extravasate into the tumor to allow for quantitative pH_e mapping and demonstrating the first time that BIRDS has been used to monitor pH_e changes in a tumor in the context of a therapeutic study. Representative longitudinal pH_e maps in sorafenib treated and DMSO control animals are shown in **Figure 5.8A**. The pH_e was not different between DMSO and sorafenib groups at baseline (Day 10) (6.53±0.04 vs. 6.53±0.08, respectively). However, at four days post-treatment, the pH_e in sorafenib treated tumors increased to 6.77±0.05, while in DMSO control tumors the pH_e remained unchanged (6.58±0.06) (**Figure 5.8B**). The statistically significant ($p=0.01$) increase in pH_e represented a trend towards normalization of the intratumoral pH_e as normal brain pH_e is ~7.1-7.3. Notably, this increase in pH_e began within the first days of treatment, before the pronounced vascular changes expected with TKIs developed. However, due to the vascular effects of sorafenib, as reflected in the reduction in contrast enhancement on T_1-weighted imaging, $TmDOTP^{5-}$ was not delivered to the tumor in sufficient amounts to allow for pH_e mapping at later time points in treated tumors as can be seen in CSI datasets where sharp signals are seen from $TmDOTP^{5-}$ within the tumor at Day 10 (baseline) and Day 15 (4 days post-treatment), but are absent at later time points (**Figure 5.8C**).

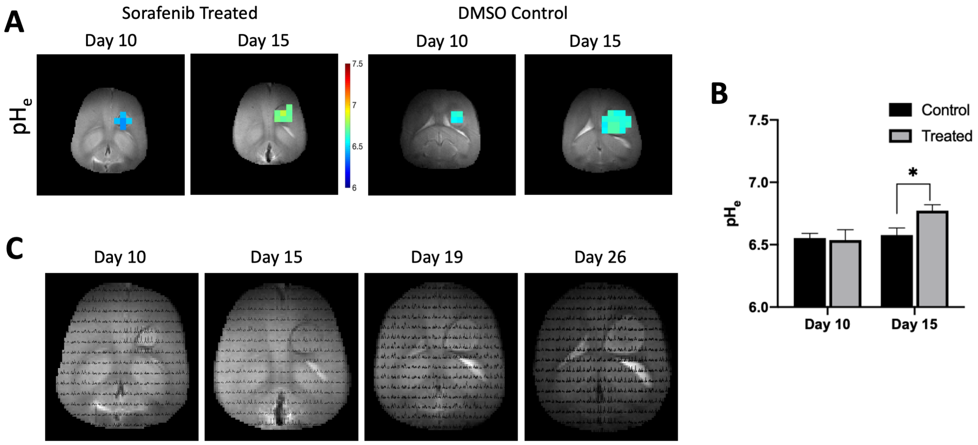

Figure 5.8. Effects of sorafenib on extracellular pH. (A) Representative pH_e maps are shown at baseline (Day 10) and four days after sorafenib therapy or DMSO control (Day 15). pH_e was quantified over the tumor ROI and overlaid on T_2-weighted images (TE/TR: 30/6000 ms) of the entire brain. The two time points were acquired in the same animal. (B) Average pH_e for each time point across all tumors. All values are shown as average ± standard deviation where $^*p=0.01$. (C) Representative CSI datasets for a sorafenib-treated tumor acquired at baseline (Day 10) as well as 4, 8, and 15 days after the start of sorafenib therapy. The contrast agent ($TmDOTP^{5-}$) is detectable at baseline as well as four days post-treatment; however, at later time points, the agent is not delivered to the tumor in sufficient amounts to make pH_e mapping possible.

5.5 Discussion

Assessment of therapeutic response in GBMs is usually achieved by T_1- and T_2-dependent MRI contrasts. However, these methods can be confounded by pseudoprogresson and pseudoresponse. Thus, alternative methods for monitoring therapeutic response are needed.

Various MRS and MRI techniques for pH_e mapping have been previously reported. Gallagher *et al*. imaged pH_e in mouse lymphoma using hyperpolarized ^{13}C bicarbonate measurements.[109] pH_e-sensitive contrast was measured in C6 glioma rats using GdDOTA-4Amp^{5-}, a pH sensitive T_1 agent.[88] MRI methods based on chemical exchange saturation transfer (CEST), using either diamagnetic or paramagnetic agents have been used to generate pH_e-sensitive maps such as CEST imaging of the amine protons on glutamine. Amide proton transfer (APT) and amine CEST have been used in both preclinical and clinical settings.[130,197]

BIRDS is a different technique, which has been used to image the intratumoral-peritumoral pH_e gradient in gliomas.[141,198] Because the molecular readout from the TmDOTP^{5-} protons is chemical shift-dependent, the method is independent of field strength and agent concentration. We reported previously that the error in pH determination depends on the error in chemical shift measurement, which in turn depends on the signal-to-noise ratio (SNR) for each proton resonance.[134] Typical *in vivo* SNR values for H2, H3 and H6 protons is in the range of 5 to 20, which corresponds to an error in pH measurement in the range of 0.01 to 0.03. While a limitation of BIRDS is the spatial resolution compared to conventional MRI, the pH_e readout even at a course spatial resolution provides valuable insights into the tumor microenvironment in relation to its neighboring tissue.

It was observed by Estrella et al. (2013) that regions of highest tumor invasion corresponded to regions of lowest pH_e.[5] So, it is hypothesized that acidic pH_e mediates local invasive growth and metastasis. Recently, we showed that extensive acidic pH_e in the periphery of the tumor is correlated with increased invasiveness. This is associated with increased presence of Ki-67 positive cells in the tumor boundary of invasive models.[141] Similarly, in untreated tumors we observed lower pH_e in the tumor boundary and increased presence of Ki-67 positive cells indicative of increased proliferation and invasive growth. TMZ treatment in U87 rat gliomas has shown alterations in the lactate to pyruvate ratio in comparison with untreated rats due to reduced pyruvate kinase M2 activity.[199,200] In addition, reduced metabolic output in response to reduced tumor burden suggests altered pH_e in intratumoral and peritumoral regions in response to TMZ. We observed an inhibition of tumor growth with TMZ treatment, similar to several previous reports.[200-203] Also in agreement with previous studies, we observed apoptosis induction and reduced proliferation with TMZ treatment.[199,203]

In a recent report by Huang et al., we present an alternative method for achieving a transient increase in the circulatory concentration of BIRDS agents ($TmDOTP^{5-}$) by using probenecid.[135] Probenecid is an organic anion transporter inhibitor that is used to decrease the renal excretion rate of antibiotics and certain other drugs and thus achieve increased drug concentration. Co-infusion of probenecid along with $TmDOTP^{5-}$ showed that intratumoral peritumoral pH_e gradient was unaffected by co-infusion. This allowed for longitudinal studies to be performed in a cohort of U87 tumors treated with sorafenib.

Here we demonstrate longitudinal pH_e mapping with BIRDS for the first time in the context of treatments (sorafenib). The pH_e increased significantly after four days of treatment with the TKI sorafenib. This suggests that although the morphologic appearance of the tumor is unchanged, the vascular and metabolic features of the tumor microenvironment are impacted early in the treatment course. While we did observe the reduction in contrast enhancement after administration of gadolinium contrast agents (Dotarem) expected with sorafenib therapy, these changes were very modest at the earliest time points after therapy. Additionally, DCE-MRI is frequently used to study the vascular features of the tumor microenvironment. However, in the setting of anti-angiogenic therapies such as sorafenib, where the extravasation of the contrast agent into the extracellular space is greatly reduced, the dynamic modeling can lead to results that are not in agreement with the morphology of the tumor. For example, although there are significant increases in the extracellular and plasma volume fractions quantified from DCE-MRI, there are no corresponding changes in the tumor appearance on imaging that would suggest that the tumor is becoming less cellular (decreased extracellular volume fraction, v_e). Additional support for this finding comes from measures of the apparent diffusion coefficient (ADC) that has been correlated with tumor cellularity, such that reductions in ADC represent more highly cellular tumors.[80] However, changes in tumor ADC in U87 tumors is not observed. Therefore, the reductions in pH_e early during the course of therapy can represent a novel way to differentiate a therapeutic response.

In conclusion, mapping pH_e in intratumoral and peritumoral regions using BIRDS could serve as a biomarker in evaluating therapeutic response in gliomas which in turn could be potentially applied in evaluating response to a wide range of therapies beyond temozolomide and sorafenib.

Chapter 6: Conclusion and Ongoing/Future Directions

6.1 Summary

In the work presented in this dissertation, we have used a variety of magnetic resonance imaging (MRI) and spectroscopic imaging (MRSI) methods to study the tumor microenvironment in human-derived preclinical models of glioblastoma. In particular, we have further developed Biosensor Imaging of Redundant Deviation in Shifts (BIRDS) as a quantitative tool for studying tumor metabolism as reflected by an acidic extracellular pH (pH_e). In prior work, BIRDS pH_e mapping has been used to measure the intratumoral–peritumoral pH_e gradient in 9L and RG2 rodent models of gliomas and to correlate the extensive acidic pH_e in regions surrounding the tumor with tumor cell invasion.[141] Here, we have expanded BIRDS to image the acidic pH_e in several human-derived models of glioblastoma (U87 and U251).

While prior work using BIRDS has relied on renal intervention to reduce contrast agent clearance, a BIRDS protocol was developed using pharmacologic inhibition of renal clearance that allowed for longitudinal, repeated pH_e mapping (Chapter 3). We then exploited the corresponding temperature readout from BIRDS in a hypothermia model to verify the quantitative ability of the method. The cerebral temperature was manipulated and the corresponding temperature changes were measured by BIRDS.[204] Due to the redundant nature of the measurement, BIRDS provides simultaneous quantitative measures of both pH and temperature that are calculated based on the same calibration.

Further, the longitudinal BIRDS protocol allowed for measuring the acidic microenvironment throughout tumor progression (Chapter 4). We combined BIRDS with other MRI techniques, including diffusion-weighted imaging and dynamic contrast enhanced imaging to provide imaging markers of tumor cellularity and vascularity, allowing for a thorough characterization of the vascular and metabolic features of the tumor microenvironment. We made simultaneous and longitudinal measurements of tumor perfusion (F_p), permeability (K^{trans}), and volume fractions of interstitial (v_e) and plasma (v_p) spaces from dynamic contrast enhanced (DCE) MRI, cellularity from apparent diffusion coefficient (ADC) MRI, and extracellular pH (pH_e) from BIRDS. Spatiotemporal patterns of these parameters during tumorigenesis were unique for each tumor and both U251 and U87 tumors became acidic (pH_e 6.1-6.8) early during tumor formation and remained acidic throughout tumor progression. While there was no correlation between tumor size and pH_e, U251 tumors were more acidic, suggesting lower aerobic glycolysis than in U87 tumors.

Finally, we provided further evidence supporting the role of pH_e as a potential biomarker of therapeutic response (Chapter 5). Rats bearing U251 gliomas treated with temozolomide (40 mg/kg) had a lower intratumoral–peritumoral pH_e gradient and a reduced tumor volume with increased proliferation and induction of apoptosis when compared to untreated rats.[142] Additionally, rats bearing U87 gliomas had an increased intratumoral pH_e with sorafenib (100 mg/kg) therapy. BIRDS was shown to be able to be used to map the pH_e in gliomas and provide a physiological readout of the therapeutic response on the tumor microenvironment.

Using imaging methods sensitive to the cellular, vascular and metabolic features of the tumor allows for a more comprehensive characterization of the tumor microenvironment that may shed insights into changes reflective of the treatment response. The development of pH_e mapping imaging may serve as a biomarker of disease progression and response to therapy. Based on these results, ongoing work as described in this chapter has expanded BIRDS beyond common glioma models. One critique of cell line models is that they are not representative of clinical disease. To address this concern, we sought to implement BIRDS-based pH_e mapping in a patient-derived xenograft model of metastatic melanoma. We also sought to expand the applicability of BIRDS by implementing the method on clinical MRI scanners and in tumors in different parts of the body. Finally, in the context of glioblastoma, we sought to gain further insight into the role of central necrosis and peritumoral edema through histological comparisons and their potential impact on anti-tumor immunity in glioblastoma. Taken together, this ongoing work provides the basis for future studies on applications for pH_e mapping in assessing different therapies in a multitude of different cancers, as well as technical improvements that can lead to improved imaging times and spatial resolution in BIRDS pH_e mapping.

6.2 Application of BIRDS to patient-derived xenograft models of metastatic melanoma

While glioblastoma is the most common primary malignant tumor in the brain, brain metastases are the most common malignancy in the CNS in adults with melanoma having a high propensity to spread to the brain.[205] Brain metastases, particularly from melanoma, present a challenge in diagnosis and therapeutic monitoring. The presentation of metastatic disease is highly heterogeneous based on location and number of tumors, as well as the tissue in which it grows being different from the tissue from which the tumor was derived.

Recent therapeutic advances have made significant progress in the treatment of metastatic melanoma to the brain using surgery, radiation, and novel immunotherapies, including the checkpoint inhibitors.[206] Particularly, perilesional edema indicates tissue involvement beyond anatomically-defined tumor boundaries and has been associated with a worse outcome in patients with metastatic melanoma. Vasogenic edema is extravasation of fluid and intravascular proteins into the cerebral parenchyma and is induced by tumor and immune secreted factors. Edema can provide a route for tumor spread and impacts therapeutic efficacy, with edema being a contradiction to immune therapies.[207] Additionally, an acidic pH_e has also been associated with increased migration and invasion in melanoma.[123,208,209] However, there are limited preclinical models available to reliably study this.

One limitation of standard rodent cell line models is that they are not reflective of clinical disease, where cell lines are chosen that exhibit some particular features of tumors. To overcome some of these limitations, patient-derived xenograft (PDX) models have been developed that involve harvesting tumor cells from a clinical tumor and then injecting those cells, either directly or after short term cell culture, into immunosuppressed rodents. In particular for imaging characterization, no PDX model of metastatic melanoma in rats has been reported previously. It has been shown that acidosis develops in melanoma;[210] however, the effect of maintaining an acidic extracellular pH (pH_e) and how it contributes to tumor invasiveness, proliferation, and inhibited therapeutic response in patient-derived tumors is unknown. The objective of this work was to use the multimodal MRI/MRSI protocol to characterize the acidic microenvironment and peritumoral edema in PDX models of metastatic melanoma.

In this work, two metastatic melanoma cell lines were used. A375BR is based on the commercially available cell line A375 which has undergone rounds of selection to promote the formation of brain metastases. YUMETRO is a PDX cell line created at Yale University by isolating tumor cells from a cerebellar metastatic melanoma lesion and growing the cells in short-term cell culture. Each cell line was labeled using a lentiviral reporter containing genes for tdTomato and luciferase (Addgene, plasmid #72486) to allow for fluorescence detection, as well as luminescence detection after administration of luciferin. Cells were infected with the reporter and then sorted for high expression of tdTomato by FACS.

Cells were maintained in culture and harvested at high confluence. After intracranial injection into the brain of athymic/nude rats (80,000 cells in 5 μL), tumors were allowed to grow and checked every 7 days for luminescence with an *in vivo* imaging system (Perkin Elmer) after intravenous administration of luciferin (150 mg/kg). Once tumors reached their growth endpoint, the MRI/MRS protocol for quantitative relaxation (T_1, T_2) and diffusion (ADC) measurements were used to characterize tumor size, structure and cellularity and quantitative pH_e measurements were made using BIRDS. All imaging data were acquired at 11.7T. Quantitative T_2 (TE/TR: 10-100/6000ms), T_1 (TE/TR: 10ms/0.4-5s, before and after 0.25 mmol/kg gadoterate meglumine) and apparent diffusion coefficient (ADC, b: 0-3000 s/mm^2) maps were acquired. For BIRDS pH_e measurements, a coinfusion of 100 mg/kg probenecid and 1 mmol/kg $TmDOTP^{5-}$ was administered and CSI was used to measure the chemical shifts of the pH_e-dependent proton resonances to calculate pH_e within each voxel at an isotropic resolution of $1mm^3$ as previously described.[6,7]

A PDX model of metastatic melanoma (YUMETRO) was successfully grown in the brain of athymic/nude rats (**Figure 6.1**). T_2 imaging at 11.7T showed peritumoral edema that extended into the grey matter of the ipsilateral hemisphere and contrast-enhanced T_1 weighted imaging showed heterogenous contrast enhancement within the tumor, features that were also exhibited in the clinical MRI prior to creation of the PDX model.

A benefit of using labeled cells was that tumor growth could be tracked using luminescence imaging, rather than MRI (**Figure 6.2**). The level of luminescence, while not perfect, is reflective of the size of the tumor. Once significant levels of luminescence were present, the tumor was then imaged using MRI. As with other tumor models, there was significant variability in the growth rates of individual tumors with YUMETRO tumors reaching their terminal sizes after 40-120 days.

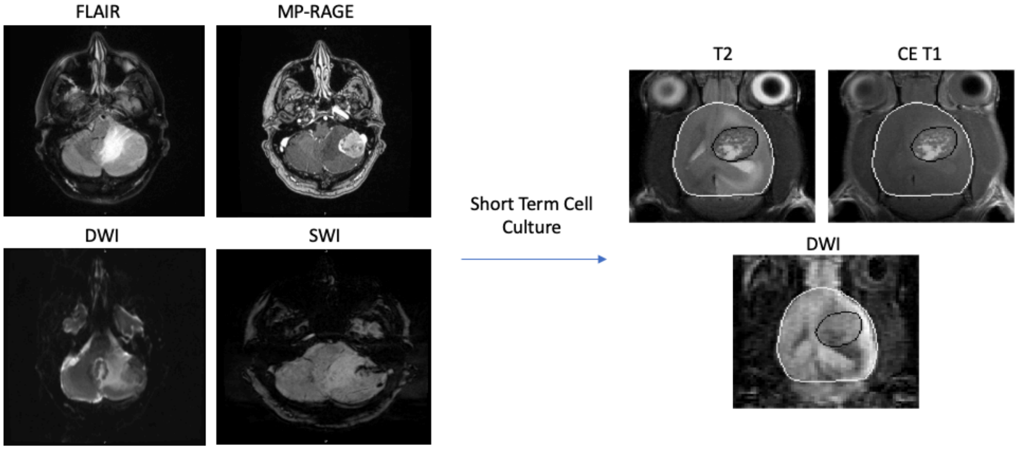

Figure 6.1. Creation of a patient-derived xenograft (PDX) model of metastatic melanoma. On the left are MRI of the patient tumor from which the YUMETRO cell line was derived, which was taken from a phase II clinical trial at Yale Cancer Center for the treatment of metastatic melanoma with pembrolizumab.[207,211,212] The clinical imaging protocol consisted of T_2 FLAIR, diffusion-weighted (DWI), susceptibility weighted (SWI) and contrast enhanced T_1-weighted (MP-RAGE) imaging. After isolating tumor cells and expanding in short term cell culture, the cells were intracranially injected into the brain of athymic rats and allowed to grow. Corresponding T_2, contrast enhanced T_1 and diffusion weighted imaging was performed and showed that peritumoral edema as well as many of the heterogenous features of the tumor were exhibited in the PDX model.

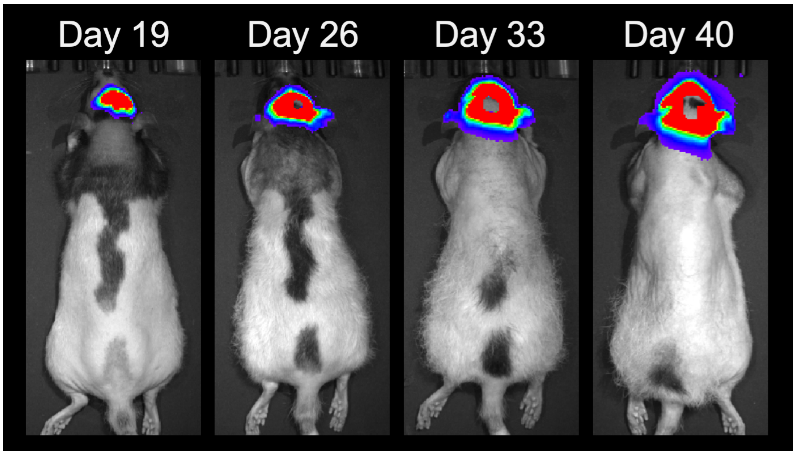

Figure 6.2. Luminescence imaging of tumor growth in YUMETRO PDX model of metastatic melanoma. Imaging was performed using an *in vivo* imaging system after intravenous administration of luciferin. All images are acquired from the same animal at different time points after intracranial injection of tumor cells. Luminescence increased with increasing tumor size.

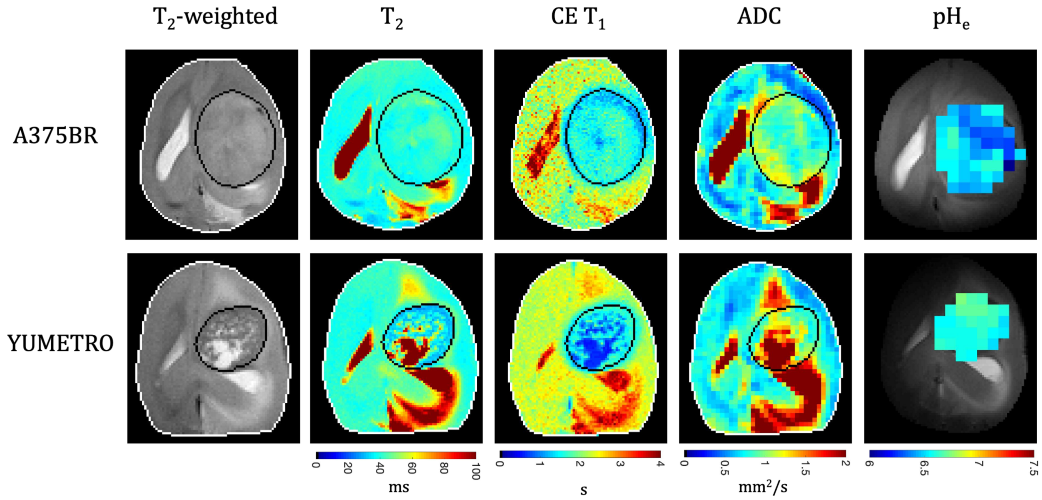

Figure 6.3. Comparison of A375BR and YUMETRO PDX models of metastatic melanoma. Anatomical T_2-weighted MRI is shown along with corresponding quantitative T_2 maps. Additionally, contrast-enhanced T_1, ADC and pH_e maps from BIRDS are also shown. All different contrasts are acquired from the same tumor. The tumor is outlined in black and the brain is outlined in white.

The YUMETRO PDX model was compared against the A375BR cell line, which is a commercially available melanoma model (**Figure 6.3**). MRI and MRSI was performed on both cell lines at 11.7T. A375BR tumors were much more homogenous in their growth, lacked peritumoral edema, and grew to much larger sizes at earlier times points in comparison to YUMETRO tumors. Both A375BR and YUMETRO tumors were acidic as measured by BIRDS with pH_e values of 6.3-6.7, although A375BR was slightly more acidic indicating higher rates of glycolytic metabolism. Regions of peritumoral edema in YUMETRO tumors exhibited higher T_2 and ADC values; however, no edema was evident in A375BR tumors. Finally, intratumoral regions of increased T_2 and ADC developed in YUMETRO tumors that were not evident in A375BR and may represent regions of necrosis.

PDX models of metastatic melanoma in rats provide a new platform for evaluating the development of acidosis in tumors. This preliminary work highlights the differences in structural appearance and edema formation in PDX models that are more reflective of clinical tumors. The peritumoral edema that forms is vasogenic in nature due to disruption of the blood-brain barrier and an increase in vascular permeability. In many respects, the growth pattern and appearance of A3675BR tumors were more similar to the U87 models of glioblastoma used previously, while the PDX models had more similarities to U251 tumors. Imaging of PDX tumors can be used in future work for evaluating the therapeutic response to a variety of different immunotherapies that are being tested in metastatic melanoma.

6.3 Applications of BIRDS to other tumor types

Although BIRDS has been utilized to measure the pH_e in rodent models of glioblastoma, all prior work was performed by imaging the brain on high-field preclinical scanners.[135,141,142,178] However, to expand the applicability and translatability of BIRDS, the development and implementation of BIRDS for pH_e mapping on a clinical MRI scanner using a large animal model is desirable. The VX2 tumor model is an orthotopic liver tumor in rabbits that exhibits growth patterns characteristic of hepatocellular carcinoma and has been previously used for translational studies involving intra-arterial therapies for liver cancer treatment.[213,214] To demonstrate the feasibility of BIRDS on a lower-field clinical scanner (3T), we used this rabbit model for liver cancer, where we measured the intratumoral–peritumoral pH_e differences in livers implanted with highly vascularized and hyper-glycolytic VX2 tumors.[213,215-218] All work presented has been recently published.[181]

All experiments were conducted under approved Animal Care and Use Committee protocols. Nine male New Zealand White rabbits (2.5-4 kg; Charles River Laboratories, MA, Boston) underwent implantation of VX2 tumors in the left lobe of the liver as previously described.[216,219,220] Tumors were allowed to grow for 14 days until a solitary tumor (1–2 cm in diameter) became visible on MRI.[221,222] All MR data was obtained on a 3T Prisma scanner (Siemens Healthcare, Erlangen, Germany) using a 15-channel radio frequency (RF) knee coil. T_1 VIBE images were obtained for localization purposes using a field-of-view (FOV) of 20x20cm^2, 384x384 matrix, 60 slices of 2.5mm thickness, TR/TE= 5.2/2.5ms.

In vivo BIRDS was performed using 15ml of $TmDOTP^{5-}$ infused at a rate of 0.5 ml/min for 30 min for a total dose of 0.5mmol/kg. Probenecid, a drug used with BIRDS to increase agent perfusion by temporarily blocking renal clearance, was not necessary in these experiments, as the contrast agent was easily able to perfuse the liver. Selective excitation of H2, H3 and H6 protons of $TmDOTP^{5-}$ was achieved using a dual-band 640μs Shinnar-Le Roux (SLR) RF pulse with 10.4kHz bandwidth and 18.9kHz separation with an offset of -4930Hz relative to the water frequency to ensure the full excitation of $TmDOTP^{5-}$ protons. Other parameters used for the 3D-CSI acquisition were a flip angle of 90^0 for the SLR pulse, a FOV of $20x20x25cm^3$, 20 averages, 13x13x13 rectangular encoding steps, and a total acquisition time of 6 minutes. The CSI dataset was reconstructed to 25x25x25 matrix, with a voxel size of $8x8x10mm^3$. The pH_e was calculated in each CSI voxel from the chemical shifts of H2, H3 and H6 $TmDOTP^{5-}$ protons, respectively, as described in Chapter 3 and in previous work.[134,194]

Tumor growth was successful in all animals (n=9). Examples of pH_e mapping using BIRDS with $TmDOTP^{5-}$ in a rabbit liver with VX2 tumors are shown in **Figure 6.4**. The VX2 tumors (red contour) were localized as a hypointensity in the T_1-weighted VIBE images (**Figure 6.4A**) within the whole liver (blue contour) and the rabbit abdomen (orange contour) for referencing and localization purposes. CSI slices (**Figure 6.4C** and **6.4D**) corresponding to the T_1-weighted images are shown. High SNR signals were visible for the H2, H3 and H6 $TmDOTP^{5-}$ protons inside the VX2 tumors but also in neighboring liver regions and in other well-perfused regions of the body (e.g. blood vessels, muscles) where $TmDOTP^{5-}$ diffused or accumulated during infusion. Examples of H2, H3 and H6 signals from two voxels, one localized inside the VX2 tumor and the other in the normal liver, are shown in **Figure 6.4E** and **Figure 6.4F**, respectively. The pH_e in these voxels were 6.80 and 7.23, respectively. For the two CSI slices shown in **Figure 6.4C** and **Figure 6.4D**, the corresponding pH_e maps were also generated (**Figure 6.4G** and **6.4H**). The average pH_e calculations indicate a lower

pH_e inside the VX2 tumor (6.77±0.03) and also in the tumor's adjacent regions (6.89±0.09), relative to the average pH_e value measured in the normal liver (7.22±0.04).

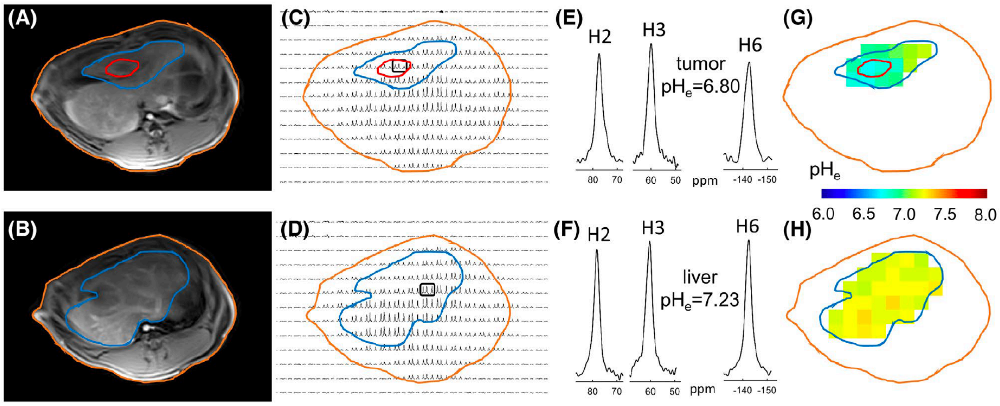

Figure 6.4. In vivo pH_e mapping using BIRDS in VX2 tumors in rabbit liver at 3T. T_1 VIBE MR images (A and B) were used to localize the VX2 tumor (red outline) within the liver (blue outline) and the abdomen (orange outline). Two different CSI slices from the same animal were used to show the H2, H3 and H6 MR signals of $TmDOTP^{5-}$ in each voxel (C and D). ^1H NMR spectra from a voxel containing tumor (E) and normal liver (F) indicate a high SNR in these voxels (>10), allowing accurate pH_e determination. The pH_e maps corresponding to the two CSI slices (C and D) are shown (G and H, respectively). The measurements indicate lower average pH_e values inside the tumor (6.77±0.03) and in the immediate vicinity of the tumor (6.89±0.09), compared to those for the normal liver (7.22±0.04). Reproduced with permission.[181]

A similar trend was observed in all rabbits investigated. The lowest pH_e was measured inside the VX2 tumors, a slightly higher pH_e in the regions adjacent to the tumors, and the highest pH_e in the liver regions further removed from the tumor (**Figure 6.5**). To better understand and compare the pH_e distributions in these three liver regions, a pH_e voxel fraction was calculated for each of these regions by counting the number of voxels with pH_e values within every 0.02 pH interval from 6 to 8, relative to the total number of voxels (**Figure 6.5A**). A fit of the pH_e voxel fraction to a Gaussian distribution provided the mean and standard deviation of the pH_e distribution. The pH_e values inside the tumor, at tumor edge, and in normal liver were 6.79±0.08, 6.88±0.09, and 7.19±0.04, respectively (**Figure 6.5B**). The pH_e values inside the tumor and at tumor's edge were significantly lower ($p<10^{-9}$ for tumor, $p<10^{-7}$ for tumor's edge) than in normal liver. Moreover, the pH_e value inside the tumor was also significantly lower than that at tumor's edge, although the calculated p-value of 0.045 is only moderately significant.

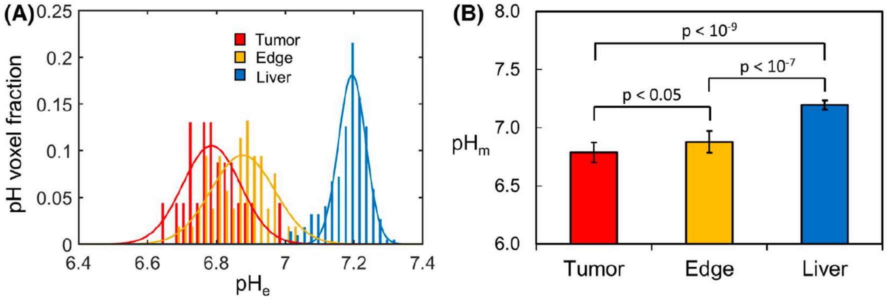

Figure 6.5. pH$_e$ value distributions in VX2 tumors in the rabbit liver. Intervals of 0.02 pH$_e$ values were used to display the voxel fractions corresponding to each pH$_e$ range (A). Intratumoral regions of VX2 tumors (red), the tumor margin (orange) and normal liver (blue) are shown. From these distributions, the mean pH$_e$ and standard deviation were calculated (B). Significantly lower pH$_e$ values were measured inside the tumor (6.79±0.08; $p<10^{-9}$) and at tumor edge (6.88±0.09; $p<10^{-7}$), compared to the pH$_e$ values measured in the normal liver (7.19±0.04). The pH$_e$ values inside the tumor are also significantly lower than those in the immediate vicinity of the tumor ($p<0.05$). Reproduced with permission.[181]

In this work, we report the mapping of pH_e with BIRDS in an orthotopic tumor model for liver cancer on clinical MRI scanners. Implementation of BIRDS on a clinical scanner (Siemens) at lower magnetic field (3T) opens up the possibility of conducting a multitude of novel MRI/MRS experiments with direct clinical relevance.

High signal-to-noise ratios (SNR) values were measured in most liver areas, including the tumor, due to excellent blood perfusion in the liver. The linewidths of the $TmDOTP^{5-}$ resonances *in vivo* suggest a heterogeneity in the pH_e distribution inside each voxel. However, a limitation of this work is the relatively large voxel size ($8x8x10mm^3$). Thus, the tumor CSI voxels are not entirely defined within the anatomically-defined tumor boundaries and there is volume averaging in voxels located near the tumor margin. Although there is variability in the size and appearance of individual tumors, the standard deviation of average tumor pH_e values is very small (0.08) underscoring the reproducibility of the pH_e measurements with BIRDS.

The significantly lower pH_e ($p<10^{-9}$) in VX2 tumors (6.79±0.08) compared to normal liver (7.19±0.04) is consistent with pH_e measurements in rat glioblastoma tumor models.[141] There was also a reduced pH_e (6.88±0.09; $p<10^{-7}$) in voxels adjacent to the tumor margin, suggesting that acidosis may spread into surrounding tissue. A similar result has been observed in rat glioblastoma models where aggressive RG2 tumors have acidic spread beyond the anatomically defined tumor margins than less aggressive 9L tumors.[141] VX2 are also aggressive tumors and the areas of low pH_e observed outside the margins of the tumor is consistent with tumor infiltration. Further, there is evidence that the anti-tumor immune response in the peritumoral region is affected by the acidic pH.[223,224] Thus, a more thorough investigation of these regions is necessary, which involves the development of CSI methodologies that will allow pH mapping at even higher spatial resolution.

In conclusion, BIRDS was further developed as a non-invasive CSI method for pH_e mapping on clinical scanners (Siemens). BIRDS was implemented to scan a location outside of the brain by using a rabbit model of liver cancer and was able to successfully compare pH_e measurements from tumor regions with those from normal liver. pH_e measurements with BIRDS may serve as a functional biomarker of metabolic activity that can reflect response to therapy and allow for further tumor characterization.

6.4 Multiparametric MRI to assess necrosis and peritumoral edema in glioblastoma

Glioblastoma exhibits a highly heterogenous tumor microenvironment characterized by central necrosis and peritumoral edema. Necrosis forms where regions of hypoxia develop, leading to tumor cell migration and a pseudopalisading pattern.[225] *In vitro* work has shown that necrotic cells can promote tumor infiltration.[226] Further, the presence of edema is associated with a poor clinical outcome.[227] The presence of edema involves additional clinical management with corticosteroids (such as dexamethasone) that also may contribute to worse outcomes. There has been increased interest in understanding the role of edema in both tumor infiltration as well as its contribution to the immunosuppressive state of glioblastomas. While immune responses are present in the brain, the immune-environment is unique due to its presence behind the protective blood-brain barrier, which prevents the accumulation of many immune cell subtypes. Given the promise of immunotherapies in other cancer types, clinical trials have not yet shown a survival benefit in glioblastoma; however, a variety of different immunotherapy strategies have been attempted.[228] However, the microenvironment is immunosuppressive which limits the ability of standard anti-programmed cell death protein-1 (anti-PD1) immunotherapy. Recent evidence suggests tumor-associated macrophages drive the production of edema in glioblastoma.[229] The infiltrative pattern may also be related to tumor vascularity as regions of reduced perfusion may have greater tumor cell infiltration.[230]

Multiparametric MRI coupled with comparisons to histological features provides an opportunity to study these patterns in glioblastoma. Volumetric analysis using MRI has shown hyperintensity on T_2-weighted FLAIR images in the peritumoral region corresponding to edema, as well as a contrast enhancing rim surrounding a non-contrast enhancing core corresponding with necrosis.[231,232] Although edema can be identified on standard T_2-weighted MRI, edema can also be detected as an increase in the apparent diffusion coefficient (ADC) in diffusion weighted imaging due to a reduction in diffusion restriction with the increase in free water. Further, dynamic contrast enhanced (DCE) MRI has been used to study the vascular parameters where regions of reduced perfusion can lead to hypoxic regions and the development of necrosis. On contrast-enhanced imaging, this can either lead to no enhancement or accumulation of contrast agent that does not clear from the tumor.

Using a subset of U87 and U251 tumors analyzed for longitudinal studies (Chapter 4), we looked to further assess necrosis and peritumoral edema that develops at later stages of tumor growth. Imaging data were acquired using an 11.7 T Bruker horizontal-bore spectrometer. All imaging was performed once the animals reached their terminal endpoint so that histological comparisons could be made with corresponding MRI. The imaging protocol included T_2-weighted, diffusion-weighted, and contrast-enhanced T_1-weighted imaging along with DCE-MRI for vascular measurements and BIRDS for pH_e mapping using the same imaging acquisition parameters as described previously. At the end of the imaging experiment, animals were perfused and the brain was extracted and fixed in 4% paraformaldehyde prior to slicing into 3 mm coronal slabs. The tissue was paraffin embedded and sectioned into 10 μm slices. Tissue sections underwent immunohistochemistry (IHC) for proliferating cell nuclear antigen (PCNA) and cluster of differentiation 68 (CD68) with hematoxylin as a counterstain. In brief, sections were deparaffinized and rehydrated prior to antigen retrieval and peroxidase blocking. Sections were incubated with primary antibodies (PCNA, CD68) followed by incubation with a biotinylated secondary antibody and 3,3-diaminobenzidine (DAB). All stained sections were mounted on glass slides and microscopy was performed (4x, 10x) for digitization and visualization using an automated high-resolution microscope with stitching capabilities (Keyence).

Peritumoral edema was much more evident in U251 tumors with most U87 tumors displaying little to no peritumoral edema (**Figure 6.6**). Edema appeared as a brighter signal on T_2-weighted images in U251 tumors, which was reflected as higher T_2 values in edematous regions (47.2±6.6 ms) compared to contralateral normal grey matter (40.8±1.7 ms). Additionally, the ADC was higher in edematous regions (1.03±0.26 mm^2/s) compared to normal tissue (0.73±0.06 mm^2/s) in the same regions of interest (ROIs) in U251 tumors. Taken together, an increased T_2 and ADC can be used to identify edematous regions.

Using an ROI analysis, different regions of the tumor could be identified including an intratumoral region as well as regions of necrosis, peritumoral edema and a contrast-enhancing rim (**Figure 6.6**). Contrast agent accumulation and clearance is evident in dynamic signal enhancement curves from DCE-MRI, where the increase in the signal intensity is due to a contrast-induced reduction in T_1 values. Similar dynamics and amount of contrast agent uptake were seen in the intratumoral region of both U87 and U251 tumors suggestive of viable tumor tissue. However, necrotic regions in U251 tumors had a faster and much greater accumulation of contrast agent, represented as a higher signal intensity. U87 tumors did not exhibit this characteristic enhancement pattern. The contrast-enhancing rim is more pronounced in U251 tumors with a slower dynamic uptake of contrast agent compared to intratumoral regions. Edematous regions are initially non-contrast enhancing and are much more pronounced in U251 tumors; however, at later times during the dynamic acquisition, edematous regions did exhibit slight increases in signal that may allow differentiation of edematous regions from normal appearing brain. Based on patterns of contrast uptake, these tumor regions can be uniquely identified with contrast-enhanced T_1-weighted imaging and the dynamics of contrast uptake provide additional metrics of characterizing vascular features.

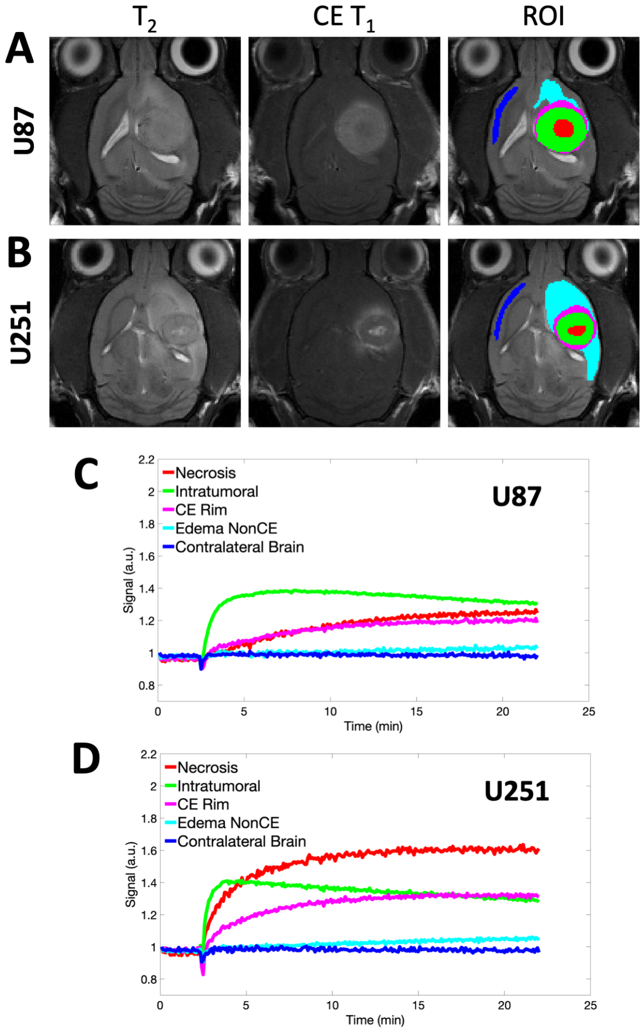

Figure 6.6. Region of interest (ROI) analysis for U87 and U251 tumors. T_2-weighted and contrast-enhanced T_1-weighted imaging are shown for U87 (A) and U251 (B) tumors. ROIs were defined for the intratumoral region (green), contrast enhancing rim (yellow), necrosis (red), edema (light blue) and contralateral hemisphere (dark blue). Dynamic signal enhancement during contrast agent administration from DCE-MRI are shown for each identified tumor region in U87 (C) and U251 (D) tumors showing distinct contrast agent uptake patterns.

To further evaluate the changes occurring in regions of peritumoral edema, immunohistochemistry was performed for proliferating cell nuclear antigen (PCNA) and cluster of differentiation 68 (CD68). PCNA is a proliferation marker that is upregulated in dividing cells. CD68 is a universal marker for macrophages that also tends to stain glial cells. We found increased immunohistochemical staining for both CD68 and PCNA in regions that corresponded to peritumoral edema identified by T_2-weighted MRI (**Figure 6.7**).

These data provide evidence that edematous regions are not just regions of increased water content, but that there are fundamental changes to the cellular components that make up this tissue. CD68 is a non-specific marker, but tends to stain both resident glial cells as well as tumor-associated macrophages which appear to be present to a much greater extent in edematous regions. Future work will seek to further characterize the edematous region in terms of acidic pH_e and immune responses which are likely modulated by the presence of infiltrating tumor cells in edematous regions.

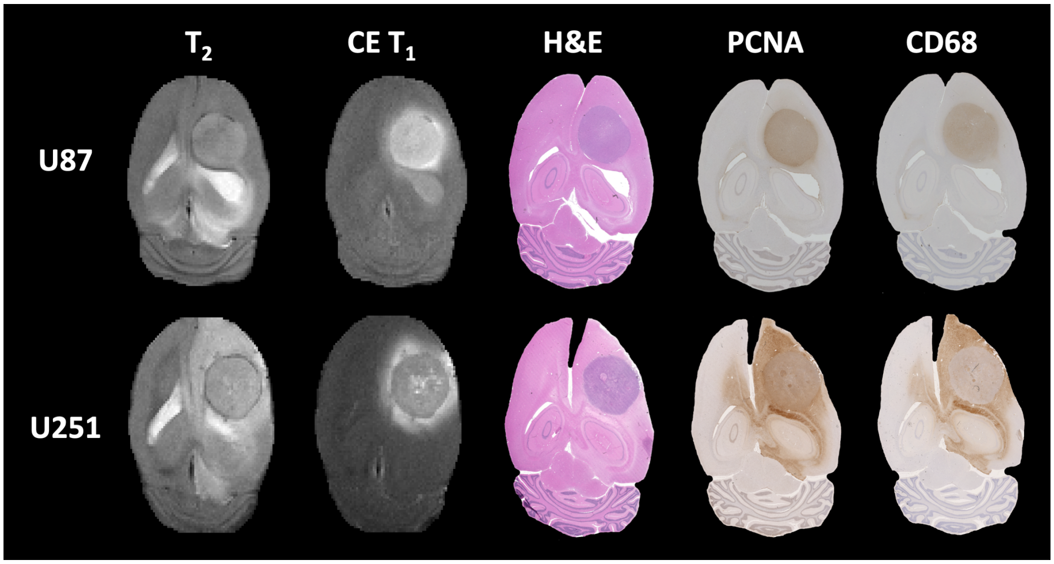

Figure 6.7. MRI and immunohistochemical evaluation of peritumoral edema in U87 and U251 tumors. T_2-weighted and contrast-enhanced (CE) T_1-weighted imaging for U87 (top row) and U251 (bottom row) tumors are used to highlight peritumoral edema and central necrosis in U251 tumors, respectively. Hematoxylin and eosin (H&E) staining provided histological comparisons of tumor architecture. Immunohistochemistry for proliferating cell nuclear antigen (PCNA) and cluster of differentiation 68 (CD68) showed regions of enhanced glial cell and macrophage proliferation in edematous regions of U251 tumors.

6.5 Conclusion

The tumor microenvironment in glioblastoma is unique due to the distinctive features of brain tissue in which these tumors form. This environment creates a favorable space for tumor cells to survive and thrive. Further, the environment is adaptable with immature and permeable vasculature and significant acidosis that develops early during tumor progression and promotes tumor infiltration into surrounding tissue. Given these changes, there is significant benefit to developing imaging methods that allow for characterizing more than just the morphological appearance of the tumor. Vascular and metabolic readouts have been studied using molecular imaging technologies with the goal of providing quantifiable biomarkers that can be used for predicting prognosis or assessing therapy efficacy and deciding whether treatment course should be changed.

In glioblastoma, a challenge is the early identification of tumor response to therapy as progression is defined entirely by radiological means (primarily MRI) that can be unclear leading to the phenomenon of pseudoprogression and pseudoresponse. Further, glioblastoma is difficult to biopsy and while tumor tissue is available at time of tumor resection for molecular analysis, multiple surgeries or subsequent biopsy are not always performed. Advanced MRI/MRS methods could be added to already existing imaging protocols to provide additional information about the state of the tumor (metabolic, vascular, immune, etc.). Vascular and metabolic characteristics could be readily identified on imaging and their changes studied with tumor progression and during therapeutic response. These changes become especially important when studying therapies that directly alter the vasculature or immune response. Metabolism, while not directly targeted by many therapies, provides an indirect readout and may be decreased with a reduction in the cellular burden of the tumor.

The goal of this work was to demonstrate methods available for quantifying metabolic and vascular features of the tumor microenvironment to complement the morphologic features that are currently in use for clinical diagnosis. Hopefully, advancements in imaging protocols and tumor characterization will lead to improvements in clinical diagnosis, monitoring tumor progression, and assessing the therapeutic response.

References

1 Ohgaki, H. & Kleihues, P. Epidemiology and etiology of gliomas. *Acta Neuropathol* **109**, 93-108, doi:10.1007/s00401-005-0991-y (2005).

2 Hanahan, D. & Weinberg, R. A. Hallmarks of cancer: the next generation. *Cell* **144**, 646-674, doi:10.1016/j.cell.2011.02.013 (2011).

3 Chen, X., Qian, Y. & Wu, S. The Warburg effect: evolving interpretations of an established concept. *Free Radic Biol Med* **79**, 253-263, doi:10.1016/j.freeradbiomed.2014.08.027 (2015).

4 Grillon, E. *et al.* The spatial organization of proton and lactate transport in a rat brain tumor. *PLoS One* **6**, e17416, doi:10.1371/journal.pone.0017416 (2011).

5 Estrella, V. *et al.* Acidity generated by the tumor microenvironment drives local invasion. *Cancer Res* **73**, 1524-1535, doi:10.1158/0008-5472.CAN-12-2796 (2013).

6 Gatenby, R. A., Gawlinski, E. T., Gmitro, A. F., Kaylor, B. & Gillies, R. J. Acid-mediated tumor invasion: a multidisciplinary study. *Cancer Res* **66**, 5216-5223, doi:10.1158/0008-5472.CAN-05-4193 (2006).

7 Corbet, C. & Feron, O. Tumour acidosis: from the passenger to the driver's seat. *Nat Rev Cancer* **17**, 577-593, doi:10.1038/nrc.2017.77 (2017).

8 Pillai, S. R. *et al.* Causes, consequences, and therapy of tumors acidosis. *Cancer Metastasis Rev* **38**, 205-222, doi:10.1007/s10555-019-09792-7 (2019).

9 Hyder, F. & Rothman, D. L. Advances in Imaging Brain Metabolism. *Annu Rev Biomed Eng* **19**, 485-515, doi:10.1146/annurev-bioeng-071516-044450 (2017).

10 Woehrer, A., Bauchet, L. & Barnholtz-Sloan, J. S. Glioblastoma survival: has it improved? Evidence from population-based studies. *Curr Opin Neurol* **27**, 666-674, doi:10.1097/WCO.0000000000000144 (2014).

11 Urbańska, K., Sokołowska, J., Szmidt, M. & Sysa, P. Glioblastoma multiforme - an overview. *Contemp Oncol (Pozn)* **18**, 307-312, doi:10.5114/wo.2014.40559 (2014).

12 Hanif, F., Muzaffar, K., Perveen, K., Malhi, S. M. & Simjee, S. U. Glioblastoma Multiforme: A Review of its Epidemiology and Pathogenesis through Clinical Presentation and Treatment. *Asian Pac J Cancer Prev* **18**, 3-9, doi:10.22034/APJCP.2017.18.1.3 (2017).

13 Bonm, A. V., Ritterbusch, R., Throckmorton, P. & Graber, J. J. Clinical Imaging for Diagnostic Challenges in the Management of Gliomas: A Review. *J Neuroimaging* **30**, 139-145, doi:10.1111/jon.12687 (2020).

14 Ragel, B. T. *et al.* The role of biopsy in the management of patients with presumed diffuse low grade glioma: A systematic review and evidence-based clinical practice guideline. *J Neurooncol* **125**, 481-501, doi:10.1007/s11060-015-1866-2 (2015).

15 Aghi, M. K. *et al.* The role of surgery in the management of patients with diffuse low grade glioma: A systematic review and evidence-based clinical practice guideline. *J Neurooncol* **125**, 503-530, doi:10.1007/s11060-015-1867-1 (2015).

16 Hanna, J. M. *et al.* Prognosticating brain tumor patient survival after laser thermotherapy: Comparison between neuroradiological reading and semi-quantitative analysis of MRI data. *Magn Reson Imaging* **65**, 45-54, doi:10.1016/j.mri.2019.09.011 (2020).

17 Ryu, S. *et al.* The role of radiotherapy in the management of progressive glioblastoma : a systematic review and evidence-based clinical practice guideline. *J Neurooncol* **118**, 489-499, doi:10.1007/s11060-013-1337-6 (2014).

18 Friedman, H. S., Kerby, T. & Calvert, H. Temozolomide and treatment of malignant glioma. *Clin Cancer Res* **6**, 2585-2597 (2000).

19 Shen, W., Hu, J. A. & Zheng, J. S. Mechanism of temozolomide-induced antitumour effects on glioma cells. *J Int Med Res* **42**, 164-172, doi:10.1177/0300060513501753 (2014).

20 Barth, R. F. & Kaur, B. Rat brain tumor models in experimental neuro-oncology: The C6, 9L, T9, RG2, F98, BT4C, RT-2 and CNS-1 gliomas. *Journal of Neuro-Oncology* **94**, 299-312, doi:10.1007/s11060-009-9875-7 (2009).

21 Aas, A. T., Brun, A., Blennow, C., Strömblad, S. & Salford, L. G. The RG2 rat glioma model. *J Neurooncol* **23**, 175-183, doi:10.1007/BF01059948 (1995).

22 Barth, R. F. & Kaur, B. Rat brain tumor models in experimental neuro-oncology: the C6, 9L, T9, RG2, F98, BT4C, RT-2 and CNS-1 gliomas. *J Neurooncol* **94**, 299-312, doi:10.1007/s11060-009-9875-7 (2009).

23 Hosono, J., Morikawa, S., Ezaki, T., Kawamata, T. & Okada, Y. Pericytes promote abnormal tumor angiogenesis in a rat RG2 glioma model. *Brain Tumor Pathol* **34**, 120-129, doi:10.1007/s10014-017-0291-y (2017).

24 Li, H. *et al.* Differences in Protein Expression between the U251 and U87 Cell Lines. *Turk Neurosurg* **27**, 894-903, doi:10.5137/1019-5149.JTN.17746-16.1 (2017).

25 Candolfi, M. *et al.* Intracranial glioblastoma models in preclinical neuro-oncology: neuropathological characterization and tumor progression. *J Neurooncol* **85**, 133-148, doi:10.1007/s11060-007-9400-9 (2007).

26 Radaelli, E. *et al.* Immunohistopathological and neuroimaging characterization of murine orthotopic xenograft models of glioblastoma multiforme recapitulating the most salient features of human disease. *Histol Histopathol* **24**, 879-891, doi:10.14670/HH-24.879 (2009).

27 Quail, D. F. & Joyce, J. A. The Microenvironmental Landscape of Brain Tumors. *Cancer Cell* **31**, 326-341, doi:10.1016/j.ccell.2017.02.009 (2017).

28 Whiteside, T. L. The tumor microenvironment and its role in promoting tumor growth. *Oncogene* **27**, 5904-5912, doi:10.1038/onc.2008.271 (2008).

29 Alfarouk, K. O. Tumor metabolism, cancer cell transporters, and microenvironmental resistance. *J Enzyme Inhib Med Chem* **31**, 859-866, doi:10.3109/14756366.2016.1140753 (2016).

30 Klemm, F. *et al.* Interrogation of the Microenvironmental Landscape in Brain Tumors Reveals Disease-Specific Alterations of Immune Cells. *Cell* **181**, 1643-1660.e1617, doi:10.1016/j.cell.2020.05.007 (2020).

31 Reinhard, J., Brosicke, N., Theocharidis, U. & Faissner, A. The extracellular matrix niche microenvironment of neural and cancer stem cells in the brain. *Int J Biochem Cell Biol*, doi:10.1016/j.biocel.2016.05.002 (2016).

32 Manini, I. *et al.* Role of Microenvironment in Glioma Invasion: What We Learned from In Vitro Models. *Int J Mol Sci* **19**, doi:10.3390/ijms19010147 (2018).

33 Ma, Q. *et al.* Cancer Stem Cells and Immunosuppressive Microenvironment in Glioma. *Front Immunol* **9**, 2924, doi:10.3389/fimmu.2018.02924 (2018).

34 Li, G. *et al.* Tumor Microenvironment in Treatment of Glioma. *Open Med (Wars)* **12**, 247-251, doi:10.1515/med-2017-0035 (2017).

35 LeBleu, V. S. Imaging the Tumor Microenvironment. *Cancer J* **21**, 174-178, doi:10.1097/PPO.0000000000000118 (2015).

36 McDonald, D. M. & Baluk, P. Significance of blood vessel leakiness in cancer. *Cancer Res* **62**, 5381-5385 (2002).

37 Krock, B. L., Skuli, N. & Simon, M. C. Hypoxia-induced angiogenesis: good and evil. *Genes Cancer* **2**, 1117-1133, doi:10.1177/1947601911423654 (2011).

38 Louveau, A. *et al.* Structural and functional features of central nervous system lymphatic vessels. *Nature* **523**, 337-341, doi:10.1038/nature14432 (2015).

39 Jain, R. K. Normalizing tumor vasculature with anti-angiogenic therapy: a new paradigm for combination therapy. *Nat Med* **7**, 987-989, doi:10.1038/nm0901-987 (2001).

40 Kaur, B. *et al.* Hypoxia and the hypoxia-inducible-factor pathway in glioma growth and angiogenesis. *Neuro Oncol* **7**, 134-153, doi:10.1215/S1152851704001115 (2005).

41 Gatenby, R. A. & Gillies, R. J. Why do cancers have high aerobic glycolysis? *Nat Rev Cancer* **4**, 891-899, doi:10.1038/nrc1478 (2004).

42 Justus, C. R., Sanderlin, E. J. & Yang, L. V. Molecular Connections between Cancer Cell Metabolism and the Tumor Microenvironment. *Int J Mol Sci* **16**, 11055-11086, doi:10.3390/ijms160511055 (2015).

43 Wachsberger, P., Burd, R. & Dicker, A. P. Tumor response to ionizing radiation combined with antiangiogenesis or vascular targeting agents: Exploring mechanisms of interaction. *Clinical Cancer Research* **9**, 1957-1971 (2003).

44 Gatenby, R. A. & Gillies, R. J. Why do cancers have high aerobic glycolysis? *Nature Reviews Cancer* **4**, 891-899, doi:10.1038/nrc1478 (2004).

45 Asgari, Y., Zabihinpour, Z., Salehzadeh-Yazdi, A., Schreiber, F. & Masoudi-Nejad, A. Alterations in cancer cell metabolism: the Warburg effect and metabolic adaptation. *Genomics* **105**, 275-281, doi:10.1016/j.ygeno.2015.03.001 (2015).

46 Fajas, L. Re-thinking cell cycle regulators: the cross-talk with metabolism. *Front Oncol* **3**, 4, doi:10.3389/fonc.2013.00004 (2013).

47 Wu, M. *et al.* Multiparameter metabolic analysis reveals a close link between attenuated mitochondrial bioenergetic function and enhanced glycolysis dependency in human tumor cells. *Am J Physiol Cell Physiol* **292**, C125-136, doi:10.1152/ajpcell.00247.2006 (2007).

48 Oliva, C. R., Moellering, D. R., Gillespie, G. Y. & Griguer, C. E. Acquisition of chemoresistance in gliomas is associated with increased mitochondrial coupling and decreased ROS production. *PLoS One* **6**, e24665, doi:10.1371/journal.pone.0024665 (2011).

49 Hirschhaeuser, F., Sattler, U. G. & Mueller-Klieser, W. Lactate: a metabolic key player in cancer. *Cancer Res* **71**, 6921-6925, doi:10.1158/0008-5472.CAN-11-1457 (2011).

50 Pereira-Nunes, A., Afonso, J., Granja, S. & Baltazar, F. Lactate and Lactate Transporters as Key Players in the Maintenance of the Warburg Effect. *Adv Exp Med Biol* **1219**, 51-74, doi:10.1007/978-3-030-34025-4_3 (2020).

51 Strambi, A. & De Milito, A. Contribution of pH Alterations to the Tumor Microenvironment. *Tumor Cell Metabolism*, 173-196, doi:10.1007/978-3-7091-1824-5_9 (2015).

52 Li, X. *et al.* Relationship of MR-derived lactate, mobile lipids, and relative blood volume for gliomas in vivo. *AJNR Am J Neuroradiol* **26**, 760-769 (2005).

53 Cassim, S. & Pouyssegur, J. Tumor Microenvironment: A Metabolic Player that Shapes the Immune Response. *Int J Mol Sci* **21**, doi:10.3390/ijms21010157 (2019).

54 Ashby, B. S. pH studies in human malignant tumours. *Lancet* **2**, 312-315, doi:10.1016/s0140-6736(66)92598-0 (1966).

55 Webb, B. A., Chimenti, M., Jacobson, M. P. & Barber, D. L. Dysregulated pH: A perfect storm for cancer progression. *Nature Reviews Cancer* **11**, 671-677, doi:10.1038/nrc3110 (2011).

56 Raghunand, N., Gatenby, R. A. & Gillies, R. J. Microenvironmental and cellular consequences of altered blood flow in tumours. *British Journal of Radiology* **76**, S11-S22, doi:10.1259/bjr/12913493 (2003).

57 Estrella, V. *et al.* Acidity generated by the tumor microenvironment drives local invasion. *Cancer Research* **73**, 1524-1535, doi:10.1158/0008-5472.CAN-12-2796 (2013).

58 Cardone, R. A., Casavola, V. & Reshkin, S. J. The role of disturbed pH dynamics and the Na+/H+ exchanger in metastasis. *Nat Rev Cancer* **5**, 786-795, doi:10.1038/nrc1713 (2005).

59 Gerweck, L. E. The pH difference between tumor and normal tissue offers a tumor specific target for the treatment of cancer. *Drug Resistance Updates* **3**, 49-50, doi:10.1054/drup.2000.0122 (2000).

60 Robey, I. F. *et al.* Bicarbonate increases tumor pH and inhibits spontaneous metastases. *Cancer Research* **69**, 2260-2268, doi:10.1158/0008-5472.CAN-07-5575 (2009).

61 Pilon-Thomas, S. *et al.* Neutralization of Tumor Acidity Improves Antitumor Responses to Immunotherapy. *Cancer Res* **76**, 1381-1390, doi:10.1158/0008-5472.CAN-15-1743 (2016).

62 Song, C. W., Griffin, R. & Park, H. J. Influence of tumor pH on therapeutic response. *Cancer Drug Resistance*, 21-42 (2006).

63 Wojtkowiak, J. W., Verduzco, D., Schramm, K. J. & Gillies, R. J. Drug resistance and cellular adaptation to tumor acidic pH microenvironment. *Mol Pharm* **8**, 2032-2038, doi:10.1021/mp200292c (2011).

64 Uthaman, S., Huh, K. M. & Park, I. K. Tumor microenvironment-responsive nanoparticles for cancer theragnostic applications. *Biomater Res* **22**, 22, doi:10.1186/s40824-018-0132-z (2018).

65 Liu, W. *et al.* Tumor-targeted pH-low insertion peptide delivery of theranostic gadolinium nanoparticles for image-guided nanoparticle-enhanced radiation therapy. *Transl Oncol* **13**, 100839, doi:10.1016/j.tranon.2020.100839 (2020).

66 Hjelmeland, A. B. *et al.* Acidic stress promotes a glioma stem cell phenotype. *Cell Death Differ* **18**, 829-840, doi:10.1038/cdd.2010.150 (2011).

67 Lardner, A. The effects of extracellular pH on immune function. *Journal of Leukocyte Biology* **69**, 522-530 (2001).

68 Chang, C. H. *et al.* Metabolic Competition in the Tumor Microenvironment Is a Driver of Cancer Progression. *Cell* **162**, 1229-1241, doi:10.1016/j.cell.2015.08.016 (2015).

69 Razavi, S. M. *et al.* Immune Evasion Strategies of Glioblastoma. *Front Surg* **3**, 11, doi:10.3389/fsurg.2016.00011 (2016).

70 Wilmotte, R. *et al.* B7-homolog 1 expression by human glioma: a new mechanism of immune evasion. *Neuroreport* **16**, 1081-1085 (2005).

71 Weiss, T., Weller, M. & Roth, P. Immunotherapy for glioblastoma: concepts and challenges. *Curr Opin Neurol* **28**, 639-646, doi:10.1097/WCO.0000000000000249 (2015).

72 Razavi, S.-M. *et al.* Immune Evasion Strategies of Glioblastoma. *Frontiers in Surgery* **3** (2016).

73 García-Martín, M. L. *et al.* Mapping extracellular pH in rat brain gliomas in vivo by 1H magnetic resonance spectroscopic imaging: comparison with maps of metabolites. *Cancer Res* **61**, 6524-6531 (2001).

74 Bhujwalla, Z. M., McCoy, C. L., Glickson, J. D., Gillies, R. J. & Stubbs, M. Estimations of intra- and extracellular volume and pH by 31P magnetic resonance spectroscopy: effect of therapy on RIF-1 tumours. *Br J Cancer* **78**, 606-611, doi:10.1038/bjc.1998.548 (1998).

75 Gillies, R. J., Liu, Z. & Bhujwalla, Z. 31P-MRS measurements of extracellular pH of tumors using 3-aminopropylphosphonate. *Am J Physiol* **267**, C195-203, doi:10.1152/ajpcell.1994.267.1.C195 (1994).

76 Coman, D. *et al.* Imaging the intratumoral-peritumoral extracellular pH gradient of gliomas. *NMR in Biomedicine* **29**, 309-319, doi:10.1002/nbm.3466 (2016).

77 Damadian, R. Tumor detection by nuclear magnetic resonance. *Science* **171**, 1151-1153, doi:10.1126/science.171.3976.1151 (1971).

78 Zhou, Z. & Lu, Z. R. Gadolinium-based contrast agents for magnetic resonance cancer imaging. *Wiley Interdiscip Rev Nanomed Nanobiotechnol* **5**, 1-18, doi:10.1002/wnan.1198 (2013).

79 Hagmann, P. *et al.* Understanding diffusion MR imaging techniques: from scalar diffusion-weighted imaging to diffusion tensor imaging and beyond. *Radiographics* **26 Suppl 1**, S205-223, doi:10.1148/rg.26si065510 (2006).

80 Chen, L. *et al.* The correlation between apparent diffusion coefficient and tumor cellularity in patients: a meta-analysis. *PLoS One* **8**, e79008, doi:10.1371/journal.pone.0079008 (2013).

81 Sourbron, S. P. & Buckley, D. L. Classic models for dynamic contrast-enhanced MRI. *NMR Biomed* **26**, 1004-1027, doi:10.1002/nbm.2940 (2013).

82 Khalifa, F. *et al.* Models and methods for analyzing DCE-MRI: a review. *Med Phys* **41**, 124301, doi:10.1118/1.4898202 (2014).

83 Tofts, P. S. *et al.* Estimating kinetic parameters from dynamic contrast-enhanced T(1)-weighted MRI of a diffusable tracer: standardized quantities and symbols. *J Magn Reson Imaging* **10**, 223-232, doi:10.1002/(sici)1522-2586(199909)10:3<223::aid-jmri2>3.0.co;2-s (1999).

84 Hashim, A. I., Zhang, X., Wojtkowiak, J. W., Martinez, G. V. & Gillies, R. J. Imaging pH and metastasis. *NMR in Biomedicine* **24**, 582-591, doi:10.1002/nbm.1644 (2011).

85 Chen, L. Q. & Pagel, M. D. Evaluating pH in the Extracellular Tumor Microenvironment Using CEST MRI and Other Imaging Methods. *Adv Radiol* **2015**, doi:10.1155/2015/206405 (2015).

86 Anemone, A., Consolino, L., Arena, F., Capozza, M. & Longo, D. L. Imaging tumor acidosis: a survey of the available techniques for mapping in vivo tumor pH. *Cancer Metastasis Rev* **38**, 25-49, doi:10.1007/s10555-019-09782-9 (2019).

87 Garcia-Martin, M. L. *et al.* High resolution pH(e) imaging of rat glioma using pH-dependent relaxivity. *Magn Reson Med* **55**, 309-315, doi:10.1002/mrm.20773 (2006).

88 Martinez, G. V. *et al.* Imaging the extracellular pH of tumors by MRI after injection of a single cocktail of T1 and T2 contrast agents. *NMR Biomed* **24**, 1380-1391, doi:10.1002/nbm.1701 (2011).

89 Aime, S., Fedeli, F., Sanino, A. & Terreno, E. A R2/R1 ratiometric procedure for a concentration-independent, pH-responsive, Gd(III)-based MRI agent. *J Am Chem Soc* **128**, 11326-11327, doi:10.1021/ja062387x (2006).

90 Frullano, L., Catana, C., Benner, T., Sherry, A. D. & Caravan, P. Bimodal MR-PET agent for quantitative pH imaging. *Angew Chem Int Ed Engl* **49**, 2382-2384, doi:10.1002/anie.201000075 (2010).

91 Sun, P. Z., Xiao, G., Zhou, I. Y., Guo, Y. & Wu, R. A method for accurate pH mapping with chemical exchange saturation transfer (CEST) MRI. *Contrast Media Mol Imaging* **11**, 195-202, doi:10.1002/cmmi.1680 (2016).

92 Moon, B. F. *et al.* A comparison of iopromide and iopamidol, two acidoCEST MRI contrast media that measure tumor extracellular pH. *Contrast Media Mol Imaging* **10**, 446-455, doi:10.1002/cmmi.1647 (2015).

93 Hancu, I. *et al.* CEST and PARACEST MR contrast agents. *Acta Radiol* **51**, 910-923, doi:10.3109/02841851.2010.502126 (2010).

94 Sheth, V. R., Liu, G., Li, Y. & Pagel, M. D. Improved pH measurements with a single PARACEST MRI contrast agent. *Contrast Media Mol Imaging* **7**, 26-34, doi:10.1002/cmmi.460 (2012).

95 Zhang, S., Merritt, M., Woessner, D. E., Lenkinski, R. E. & Sherry, A. D. PARACEST agents: modulating MRI contrast via water proton exchange. *Acc Chem Res* **36**, 783-790, doi:10.1021/ar020228m (2003).

96 Albatany, M., Li, A., Meakin, S. & Bartha, R. Dichloroacetate induced intracellular acidification in glioblastoma: in vivo detection using AACID-CEST MRI at 9.4 Tesla. *J Neurooncol* **136**, 255-262, doi:10.1007/s11060-017-2664-9 (2018).

97 Chen, L. Q. *et al.* Evaluations of extracellular PH within in vivo tumors using acidocest MRI. *Magnetic Resonance in Medicine* **72**, 1408-1417, doi:10.1002/mrm.25053 (2014).

98 Harris, R. J. *et al.* PH-weighted molecular imaging of gliomas using amine chemical exchange saturation transfer MRI. *Neuro-Oncology* **17**, 1514-1524, doi:10.1093/neuonc/nov106 (2015).

99 Sagiyama, K. *et al.* In vivo chemical exchange saturation transfer imaging allows early detection of a therapeutic response in glioblastoma. *Proceedings of the*

National Academy of Sciences of the United States of America **111**, 4542-4547, doi:10.1073/pnas.1323855111 (2014).

100 Park, J. E. *et al.* Pre- and Posttreatment Glioma: Comparison of Amide Proton Transfer Imaging with MR Spectroscopy for Biomarkers of Tumor Proliferation. *Radiology* **278**, 514-523, doi:10.1148/radiol.2015142979 (2016).

101 Gillies, R. J., Raghunand, N., Garcia-Martin, M. L. & Gatenby, R. A. pH imaging. A review of pH measurement methods and applications in cancers. *IEEE Eng Med Biol Mag* **23**, 57-64, doi:10.1109/memb.2004.1360409 (2004).

102 Mason, R. P. Transmembrane pH gradients in vivo: measurements using fluorinated vitamin B6 derivatives. *Curr Med Chem* **6**, 481-499 (1999).

103 Mehta, V. D. *et al.* 6-Fluoropyridoxol: a novel probe of cellular pH using 19F NMR spectroscopy. *FEBS Lett* **349**, 234-238, doi:10.1016/0014-5793(94)00675-x (1994).

104 Vermathen, P., Capizzano, A. A. & Maudsley, A. A. Administration and (1)H MRS detection of histidine in human brain: application to in vivo pH measurement. *Magn Reson Med* **43**, 665-675, doi:10.1002/(sici)1522-2594(200005)43:5<665::aid-mrm8>3.0.co;2-3 (2000).

105 García-Martín, M. L. *et al.* Mapping extracellular pH in rat brain gliomas in Vivo by 1H magnetic resonance spectroscopic imaging: Comparison with maps of metabolites. *Cancer Research* **61**, 6524-6531 (2001).

106 Provent, P. *et al.* Serial in vivo spectroscopic nuclear magnetic resonance imaging of lactate and extracellular pH in rat gliomas shows redistribution of protons away from sites of glycolysis. *Cancer Res* **67**, 7638-7645, doi:10.1158/0008-5472.CAN-06-3459 (2007).

107 Korenchan, D. E. *et al.* Dicarboxylic acids as pH sensors for hyperpolarized ^{13}C magnetic resonance spectroscopic imaging. *Analyst* **142**, 1429-1433, doi:10.1039/c7an00076f (2017).

108 Düwel, S. *et al.* Imaging of pH in vivo using hyperpolarized ^{13}C-labelled zymonic acid. *Nat Commun* **8**, 15126, doi:10.1038/ncomms15126 (2017).

109 Gallagher, F. A. *et al.* Magnetic resonance imaging of pH in vivo using hyperpolarized 13C-labelled bicarbonate. *Nature* **453**, 940-943, doi:10.1038/nature07017 (2008).

110 Coman, D., Trubel, H. K., Rycyna, R. E. & Hyder, F. Brain temperature and pH measured by 1H chemical shift imaging of a thulium agent. *NMR in Biomedicine* **22**, 229-239, doi:10.1002/nbm.1312 (2009).

111 Huang, Y., Coman, D., Ali, M. M. & Hyder, F. Lanthanide ion (III) complexes of 1,4,7,10-tetraazacyclododecane-1,4,7,10-tetraaminophosphonate for dual biosensing of pH with chemical exchange saturation transfer (CEST) and biosensor imaging of redundant deviation in shifts (BIRDS). *Contrast Media and Molecular Imaging* **10**, 51-58, doi:10.1002/cmmi.1604 (2015).

112 Coman, D., Kiefer, G. E., Rothman, D. L., Sherry, A. D. & Hyder, F. A lanthanide complex with dual biosensing properties: CEST (chemical exchange saturation transfer) and BIRDS (biosensor imaging of redundant deviation in shifts) with europium DOTA-tetraglycinate. *NMR in Biomedicine* **24**, 1216-1225, doi:10.1002/nbm.1677 (2011).

113 Andreev, O. A., Engelman, D. M. & Reshetnyak, Y. K. pH-sensitive membrane peptides (pHLIPs) as a novel class of delivery agents. *Mol Membr Biol* **27**, 341-352, doi:10.3109/09687688.2010.509285 (2010).

114 Demoin, D. W. *et al.* PET Imaging of Extracellular pH in Tumors with (64)Cu- and (18)F-Labeled pHLIP Peptides: A Structure-Activity Optimization Study. *Bioconjug Chem* **27**, 2014-2023, doi:10.1021/acs.bioconjchem.6b00306 (2016).

115 Farwell, M. D., Pryma, D. A. & Mankoff, D. A. PET/CT imaging in cancer: current applications and future directions. *Cancer* **120**, 3433-3445, doi:10.1002/cncr.28860 (2014).

116 Zhu, A., Lee, D. & Shim, H. Metabolic positron emission tomography imaging in cancer detection and therapy response. *Semin Oncol* **38**, 55-69, doi:10.1053/j.seminoncol.2010.11.012 (2011).

117 Rottenberg, D. A. *et al.* In vivo measurement of brain tumor pH using [11C]DMO and positron emission tomography. *Ann Neurol* **17**, 70-79, doi:10.1002/ana.410170116 (1985).

118 Wyatt, L. C. *et al.* Peptides of pHLIP family for targeted intracellular and extracellular delivery of cargo molecules to tumors. *Proc Natl Acad Sci U S A* **115**, E2811-E2818, doi:10.1073/pnas.1715350115 (2018).

119 Viola-Villegas, N. T. *et al.* Understanding the pharmacological properties of a metabolic PET tracer in prostate cancer. *Proc Natl Acad Sci U S A* **111**, 7254-7259, doi:10.1073/pnas.1405240111 (2014).

120 Flavell, R. R. *et al.* Caged [(18)F]FDG Glycosylamines for Imaging Acidic Tumor Microenvironments Using Positron Emission Tomography. *Bioconjug Chem* **27**, 170-178, doi:10.1021/acs.bioconjchem.5b00584 (2016).

121 Walsh, J. J. *et al.* Dynamic Thermal Mapping of Localized Therapeutic Hypothermia in the Brain. *J Neurotrauma* **37**, 55-65, doi:10.1089/neu.2019.6485 (2020).

122 Webb, B. A., Chimenti, M., Jacobson, M. P. & Barber, D. L. Dysregulated pH: a perfect storm for cancer progression. *Nat Rev Cancer* **11**, 671-677, doi:10.1038/nrc3110 (2011).

123 Stock, C. *et al.* Migration of human melanoma cells depends on extracellular pH and Na+/H+ exchange. *J Physiol* **567**, 225-238, doi:10.1113/jphysiol.2005.088344 (2005).

124 Justus, C. R., Dong, L. & Yang, L. V. Acidic tumor microenvironment and pH-sensing G protein-coupled receptors. *Front Physiol* **4**, 354, doi:10.3389/fphys.2013.00354 (2013).

125 Huber, V. *et al.* Cancer acidity: An ultimate frontier of tumor immune escape and a novel target of immunomodulation. *Semin Cancer Biol* **43**, 74-89, doi:10.1016/j.semcancer.2017.03.001 (2017).

126 Hashim, A. I., Zhang, X., Wojtkowiak, J. W., Martinez, G. V. & Gillies, R. J. Imaging pH and metastasis. *NMR Biomed* **24**, 582-591, doi:10.1002/nbm.1644 (2011).

127 Robey, I. F. *et al.* Bicarbonate increases tumor pH and inhibits spontaneous metastases. *Cancer Res* **69**, 2260-2268, doi:10.1158/0008-5472.CAN-07-5575 (2009).

128 Gillies, R. J., Ogino, T., Shulman, R. G. & Ward, D. C. 31P nuclear magnetic resonance evidence for the regulation of intracellular pH by Ehrlich ascites tumor cells. *J Cell Biol* **95**, 24-28, doi:10.1083/jcb.95.1.24 (1982).

129 Chen, M. *et al.* Extracellular pH is a biomarker enabling detection of breast cancer and liver cancer using CEST MRI. *Oncotarget* **8**, 45759-45767, doi:10.18632/oncotarget.17404 (2017).

130 Harris, R. J. *et al.* pH-weighted molecular imaging of gliomas using amine chemical exchange saturation transfer MRI. *Neuro Oncol* **17**, 1514-1524, doi:10.1093/neuonc/nov106 (2015).

131 Chen, L. Q. *et al.* Evaluations of extracellular pH within in vivo tumors using acidoCEST MRI. *Magn Reson Med* **72**, 1408-1417, doi:10.1002/mrm.25053 (2014).

132 Huang, Y., Coman, D., Ali, M. M. & Hyder, F. Lanthanide ion (III) complexes of 1,4,7,10-tetraazacyclododecane-1,4,7,10-tetraaminophosphonate for dual biosensing of pH with chemical exchange saturation transfer (CEST) and biosensor imaging of redundant deviation in shifts (BIRDS). *Contrast Media Mol Imaging* **10**, 51-58, doi:10.1002/cmmi.1604 (2015).

133 Coman, D., de Graaf, R. A., Rothman, D. L. & Hyder, F. In vivo three-dimensional molecular imaging with Biosensor Imaging of Redundant Deviation in Shifts (BIRDS) at high spatiotemporal resolution. *NMR Biomed* **26**, 1589-1595, doi:10.1002/nbm.2995 (2013).

134 Coman, D., Trubel, H. K., Rycyna, R. E. & Hyder, F. Brain temperature and pH measured by (1)H chemical shift imaging of a thulium agent. *NMR Biomed* **22**, 229-239, doi:10.1002/nbm.1312 (2009).

135 Huang, Y. *et al.* Towards longitudinal mapping of extracellular pH in gliomas. *NMR Biomed* **29**, 1364-1372, doi:10.1002/nbm.3578 (2016).

136 Coman, D., Trubel, H. K. & Hyder, F. Brain temperature by Biosensor Imaging of Redundant Deviation in Shifts (BIRDS): comparison between TmDOTP5- and TmDOTMA-. *NMR Biomed* **23**, 277-285, doi:10.1002/nbm.1461 (2010).

137 Engin, K. *et al.* Extracellular pH distribution in human tumours. *Int J Hyperthermia* **11**, 211-216, doi:10.3109/02656739509022457 (1995).

138 Donovan, M. D., O'Brien, F. E., Boylan, G. B., Cryan, J. F. & Griffin, B. T. The effect of organic anion transporter 3 inhibitor probenecid on bumetanide levels in the brain: an integrated in vivo microdialysis study in the rat. *J Pharm Pharmacol* **67**, 501-510, doi:10.1111/jphp.12341 (2015).

139 Hedaya, M. A., Elmquist, W. F. & Sawchuk, R. J. Probenecid inhibits the metabolic and renal clearances of zidovudine (AZT) in human volunteers. *Pharm Res* **7**, 411-417, doi:10.1023/a:1015835826114 (1990).

140 Overbosch, D., Van Gulpen, C., Hermans, J. & Mattie, H. The effect of probenecid on the renal tubular excretion of benzylpenicillin. *Br J Clin Pharmacol* **25**, 51-58, doi:10.1111/j.1365-2125.1988.tb03281.x (1988).

141 Coman, D. *et al.* Imaging the intratumoral-peritumoral extracellular pH gradient of gliomas. *NMR Biomed* **29**, 309-319, doi:10.1002/nbm.3466 (2016).

142 Rao, J. U. *et al.* Temozolomide arrests glioma growth and normalizes intratumoral extracellular pH. *Sci Rep* **7**, 7865, doi:10.1038/s41598-017-07609-7 (2017).

143 Cooper, D. J. *et al.* Effect of Early Sustained Prophylactic Hypothermia on Neurologic Outcomes Among Patients With Severe Traumatic Brain Injury: The POLAR Randomized Clinical Trial. *JAMA* **320**, 2211-2220, doi:10.1001/jama.2018.17075 (2018).

144 Cooper, D. J., Nichol, A. & Presneill, J. Hypothermia for Intracranial Hypertension after Traumatic Brain Injury. *N Engl J Med* **374**, 1384, doi:10.1056/NEJMc1600339 (2016).

145 Mrozek, S., Vardon, F. & Geeraerts, T. Brain temperature: physiology and pathophysiology after brain injury. *Anesthesiol Res Pract* **2012**, 989487, doi:10.1155/2012/989487 (2012).

146 Blennow, K. *et al.* Traumatic brain injuries. *Nat Rev Dis Primers* **2**, 16084, doi:10.1038/nrdp.2016.84 (2016).

147 Dietrich, W. D. & Bramlett, H. M. The evidence for hypothermia as a neuroprotectant in traumatic brain injury. *Neurotherapeutics* **7**, 43-50, doi:10.1016/j.nurt.2009.10.015 (2010).

148 Childs, C. & Lunn, K. W. Clinical review: Brain-body temperature differences in adults with severe traumatic brain injury. *Crit Care* **17**, 222, doi:10.1186/cc11892 (2013).

149 Erickson, K. M. & Lanier, W. L. Anesthetic technique influences brain temperature, independently of core temperature, during craniotomy in cats. *Anesth Analg* **96**, 1460-1466, table of contents, doi:10.1213/01.ane.0000061221.23197.ce (2003).

150 Wass, C. T., Cable, D. G., Schaff, H. V. & Lanier, W. L. Anesthetic technique influences brain temperature during cardiopulmonary bypass in dogs. *Ann Thorac Surg* **65**, 454-460, doi:10.1016/s0003-4975(97)01235-6 (1998).

151 Karaszewski, B. *et al.* Measurement of brain temperature with magnetic resonance spectroscopy in acute ischemic stroke. *Ann Neurol* **60**, 438-446, doi:10.1002/ana.20957 (2006).

152 Michenfelder, J. D. & Milde, J. H. The relationship among canine brain temperature, metabolism, and function during hypothermia. *Anesthesiology* **75**, 130-136, doi:10.1097/00000542-199107000-00021 (1991).

153 Soleimanpour, H., Rahmani, F., Golzari, S. E. & Safari, S. Main complications of mild induced hypothermia after cardiac arrest: a review article. *J Cardiovasc Thorac Res* **6**, 1-8, doi:10.5681/jcvtr.2014.001 (2014).

154 Christian, E., Zada, G., Sung, G. & Giannotta, S. L. A review of selective hypothermia in the management of traumatic brain injury. *Neurosurg Focus* **25**, E9, doi:10.3171/FOC.2008.25.10.E9 (2008).

155 Straus, D., Prasad, V. & Munoz, L. Selective therapeutic hypothermia: a review of invasive and noninvasive techniques. *Arq Neuropsiquiatr* **69**, 981-987, doi:10.1590/s0004-282x2011000700025 (2011).

156 Sedlacik, J. *et al.* Feasibility Study of a Novel High-Flow Cold Air Cooling Protocol of the Porcine Brain Using MRI Temperature Mapping. *Ther Hypothermia Temp Manag* **8**, 45-52, doi:10.1089/ther.2017.0031 (2018).

157 Takeda, Y. *et al.* Effects of pharyngeal cooling on brain temperature in primates and humans: a study for proof of principle. *Anesthesiology* **117**, 117-125, doi:10.1097/ALN.0b013e3182580536 (2012).

158 Wu, C. *et al.* Safety, feasibility, and potential efficacy of intraarterial selective cooling infusion for stroke patients treated with mechanical thrombectomy. *J Cereb Blood Flow Metab* **38**, 2251-2260, doi:10.1177/0271678X18790139 (2018).

159 Moomiaie, R. M. *et al.* Novel intracranial brain cooling catheter to mitigate brain injuries. *J Neurointerv Surg* **4**, 130-133, doi:10.1136/jnis.2010.004432 (2012).

160 De Milito, A. *et al.* pH-dependent antitumor activity of proton pump inhibitors against human melanoma is mediated by inhibition of tumor acidity. *Int J Cancer* **127**, 207-219, doi:10.1002/ijc.25009 (2010).

161 Ella, A., Delgadillo, J. A., Chemineau, P. & Keller, M. Computation of a high-resolution MRI 3D stereotaxic atlas of the sheep brain. *J Comp Neurol* **525**, 676-692, doi:10.1002/cne.24079 (2017).

162 Curran, E. J., Wolfson, D. L., Watts, R. & Freeman, K. Cold Blooded: Evaluating Brain Temperature by MRI During Surface Cooling of Human Subjects. *Neurocrit Care* **27**, 214-219, doi:10.1007/s12028-017-0389-4 (2017).

163 Hawthorne, C. & Piper, I. Monitoring of intracranial pressure in patients with traumatic brain injury. *Front Neurol* **5**, 121, doi:10.3389/fneur.2014.00121 (2014).

164 Wang, H. *et al.* Brain temperature and its fundamental properties: a review for clinical neuroscientists. *Front Neurosci* **8**, 307, doi:10.3389/fnins.2014.00307 (2014).

165 Blowers, S. *et al.* How does blood regulate cerebral temperatures during hypothermia? *Sci Rep* **8**, 7877, doi:10.1038/s41598-018-26063-7 (2018).

166 Hayward, J. N. & Baker, M. A. Role of cerebral arterial blood in the regulation of brain temperature in the monkey. *Am J Physiol* **215**, 389-403, doi:10.1152/ajplegacy.1968.215.2.389 (1968).

167 Hemingway, A., Robinson, R., Hemingway, C. & Wall, J. Cutaneous and brain temperatures related to respiratory metabolism of the sheep. *J Appl Physiol* **21**, 1223-1227, doi:10.1152/jappl.1966.21.4.1223 (1966).

168 Bertolizio, G., Mason, L. & Bissonnette, B. Brain temperature: heat production, elimination and clinical relevance. *Paediatr Anaesth* **21**, 347-358, doi:10.1111/j.1460-9592.2011.03542.x (2011).

169 Coman, D., Sanganahalli, B. G., Jiang, L., Hyder, F. & Behar, K. L. Distribution of temperature changes and neurovascular coupling in rat brain following 3,4-methylenedioxymethamphetamine (MDMA, "ecstasy") exposure. *NMR Biomed* **28**, 1257-1266, doi:10.1002/nbm.3375 (2015).

170 Saad, H. & Aladawy, M. Temperature management in cardiac surgery. *Glob Cardiol Sci Pract* **2013**, 44-62, doi:10.5339/gcsp.2013.7 (2013).

171 Wu, T. C. & Grotta, J. C. Hypothermia for acute ischaemic stroke. *Lancet Neurol* **12**, 275-284, doi:10.1016/S1474-4422(13)70013-9 (2013).

172 Ahmed, R., Oborski, M. J., Hwang, M., Lieberman, F. S. & Mountz, J. M. Malignant gliomas: current perspectives in diagnosis, treatment, and early response assessment using advanced quantitative imaging methods. *Cancer Manag Res* **6**, 149-170, doi:10.2147/CMAR.S54726 (2014).

173 Delgado-López, P. D. & Corrales-García, E. M. Survival in glioblastoma: a review on the impact of treatment modalities. *Clin Transl Oncol* **18**, 1062-1071, doi:10.1007/s12094-016-1497-x (2016).

174 Pope, W. B. & Brandal, G. Conventional and advanced magnetic resonance imaging in patients with high-grade glioma. *Q J Nucl Med Mol Imaging* **62**, 239-253, doi:10.23736/s1824-4785.18.03086-8 (2018).

175 Colonnese, C. & Romanelli, P. Advanced neuroimaging techniques in the management of glioblastoma multiforme. *Curr Radiopharm* **5**, 300-307, doi:10.2174/1874471011205040300 (2012).

176 Jackson, A., O'Connor, J. P., Parker, G. J. & Jayson, G. C. Imaging tumor vascular heterogeneity and angiogenesis using dynamic contrast-enhanced magnetic

resonance imaging. *Clin Cancer Res* **13**, 3449-3459, doi:10.1158/1078-0432.CCR-07-0238 (2007).

177 Carmona-Fontaine, C. *et al.* Emergence of spatial structure in the tumor microenvironment due to the Warburg effect. *Proc Natl Acad Sci U S A* **110**, 19402-19407, doi:10.1073/pnas.1311939110 (2013).

178 Maritim, S. *et al.* Mapping Extracellular pH of Gliomas in Presence of Superparamagnetic Nanoparticles: Towards Imaging the Distribution of Drug-Containing Nanoparticles and Their Curative Effect on the Tumor Microenvironment. *Contrast Media Mol Imaging* **2017**, 3849373, doi:10.1155/2017/3849373 (2017).

179 Huang, Y., Coman, D., Hyder, F. & Ali, M. M. Dendrimer-Based Responsive MRI Contrast Agents (G1-G4) for Biosensor Imaging of Redundant Deviation in Shifts (BIRDS). *Bioconjug Chem* **26**, 2315-2323, doi:10.1021/acs.bioconjchem.5b00568 (2015).

180 Maritim, S., Huang, Y., Coman, D. & Hyder, F. Characterization of a lanthanide complex encapsulated with MRI contrast agents into liposomes for biosensor imaging of redundant deviation in shifts (BIRDS). *J Biol Inorg Chem* **19**, 1385-1398, doi:10.1007/s00775-014-1200-z (2014).

181 Coman, D. *et al.* Extracellular pH mapping of liver cancer on a clinical 3T MRI scanner. *Magn Reson Med* **83**, 1553-1564, doi:10.1002/mrm.28035 (2020).

182 Savic, L. J. *et al.* Molecular Imaging of Extracellular Tumor pH to Reveal Effects of Locoregional Therapy on Liver Cancer Microenvironment. *Clin Cancer Res* **26**, 428-438, doi:10.1158/1078-0432.CCR-19-1702 (2020).

183 Aryal, M. P. *et al.* Dynamic contrast enhanced MRI parameters and tumor cellularity in a rat model of cerebral glioma at 7 T. *Magn Reson Med* **71**, 2206-2214, doi:10.1002/mrm.24873 (2014).

184 Ewing, J. R. *et al.* Peritumoral tissue compression is predictive of exudate flux in a rat model of cerebral tumor: an MRI study in an embedded tumor. *NMR Biomed* **28**, 1557-1569, doi:10.1002/nbm.3418 (2015).

185 Barnes, S. R. *et al.* ROCKETSHIP: a flexible and modular software tool for the planning, processing and analysis of dynamic MRI studies. *BMC Med Imaging* **15**, 19, doi:10.1186/s12880-015-0062-3 (2015).

186 Doblas, S. *et al.* In vivo characterization of several rodent glioma models by 1H MRS. *NMR Biomed* **25**, 685-694, doi:10.1002/nbm.1785 (2012).

187 Claes, A. *et al.* Magnetic resonance imaging-based detection of glial brain tumors in mice after antiangiogenic treatment. *Int J Cancer* **122**, 1981-1986, doi:10.1002/ijc.23306 (2008).

188 Flament, J. *et al.* In vivo CEST MR imaging of U87 mice brain tumor angiogenesis using targeted LipoCEST contrast agent at 7 T. *Magn Reson Med* **69**, 179-187, doi:10.1002/mrm.24217 (2013).

189 Lim, H., Albatany, M., Martínez-Santiesteban, F., Bartha, R. & Scholl, T. J. Longitudinal Measurements of Intra- and Extracellular pH Gradient in a Rat Model of Glioma. *Tomography* **4**, 46-54, doi:10.18383/j.tom.2018.00001 (2018).

190 Torsvik, A. *et al.* U-251 revisited: genetic drift and phenotypic consequences of long-term cultures of glioblastoma cells. *Cancer Med* **3**, 812-824, doi:10.1002/cam4.219 (2014).

191 Farace, P. *et al.* Early versus late GD-DTPA MRI enhancement in experimental glioblastomas. *J Magn Reson Imaging* **33**, 550-556, doi:10.1002/jmri.22472 (2011).

192 Field, K. M. *et al.* The role of early magnetic resonance imaging in predicting survival on bevacizumab for recurrent glioblastoma: Results from a prospective clinical trial (CABARET). *Cancer* **123**, 3576-3582, doi:10.1002/cncr.30838 (2017).

193 Honasoge, A. & Sontheimer, H. Involvement of tumor acidification in brain cancer pathophysiology. *Front Physiol* **4**, 316, doi:10.3389/fphys.2013.00316 (2013).

194 Coman, D., Trubel, H. K. & Hyder, F. Brain temperature by Biosensor Imaging of Redundant Deviation in Shifts (BIRDS): comparison between TmDOTP5- and TmDOTMA. *NMR in biomedicine* **23**, 277-285, doi:10.1002/nbm.1461 (2010).

195 Trübel, H. K., Maciejewski, P. K., Farber, J. H. & Hyder, F. Brain temperature measured by 1H-NMR in conjunction with a lanthanide complex. *J Appl Physiol (1985)* **94**, 1641-1649, doi:10.1152/japplphysiol.00841.2002 (2003).

196 van Berkel, A. *et al.* Correlation between in vivo 18F-FDG PET and immunohistochemical markers of glucose uptake and metabolism in pheochromocytoma and paraganglioma. *J Nucl Med* **55**, 1253-1259, doi:10.2967/jnumed.114.137034 (2014).

197 Haris, M. *et al.* Molecular magnetic resonance imaging in cancer. *J Transl Med* **13**, 313, doi:10.1186/s12967-015-0659-x (2015).

198 Huang, Y. *et al.* Towards longitudinal mapping of extracellular pH in gliomas. *NMR Biomed* **in Press** (2016).

199 Park, I. *et al.* Hyperpolarized 13C magnetic resonance metabolic imaging: application to brain tumors. *Neuro Oncol* **12**, 133-144, doi:10.1093/neuonc/nop043 (2010).

200 Park, I. *et al.* Changes in pyruvate metabolism detected by magnetic resonance imaging are linked to DNA damage and serve as a sensor of temozolomide response in glioblastoma cells. *Cancer Res* **74**, 7115-7124, doi:10.1158/0008-5472.CAN-14-0849 (2014).

201 Corroyer-Dulmont, A. *et al.* Detection of glioblastoma response to temozolomide combined with bevacizumab based on muMRI and muPET imaging reveals [18F]-fluoro-L-thymidine as an early and robust predictive marker for treatment efficacy. *Neuro Oncol* **15**, 41-56, doi:10.1093/neuonc/nos260 (2013).

202 Delgado-Goñi, T., Julià-Sapé, M., Candiota, A. P., Pumarola, M. & Arús, C. Molecular imaging coupled to pattern recognition distinguishes response to temozolomide in preclinical glioblastoma. *NMR Biomed* **27**, 1333-1345, doi:10.1002/nbm.3194 (2014).

203 Sagiyama, K. *et al.* In vivo chemical exchange saturation transfer imaging allows early detection of a therapeutic response in glioblastoma. *Proc Natl Acad Sci U S A* **111**, 4542-4547, doi:10.1073/pnas.1323855111 (2014).

204 Walsh, J. J. *et al.* Dynamic Thermal Mapping of Localized Therapeutic Hypothermia in the Brain. *J Neurotrauma* **Under review** (2019).

205 Nayak, L., Lee, E. Q. & Wen, P. Y. Epidemiology of brain metastases. *Curr Oncol Rep* **14**, 48-54, doi:10.1007/s11912-011-0203-y (2012).

206 Glitza Oliva, I., Tawbi, H. & Davies, M. A. Melanoma Brain Metastases: Current Areas of Investigation and Future Directions. *Cancer J* **23**, 68-74, doi:10.1097/PPO.0000000000000237 (2017).

207 Tran, T. T. *et al.* Perilesional edema in brain metastases: potential causes and implications for treatment with immune therapy. *J Immunother Cancer* **7**, 200, doi:10.1186/s40425-019-0684-z (2019).

208 Martínez-Zaguilán, R. *et al.* Acidic pH enhances the invasive behavior of human melanoma cells. *Clin Exp Metastasis* **14**, 176-186, doi:10.1007/BF00121214 (1996).

209 Stüwe, L. *et al.* pH dependence of melanoma cell migration: protons extruded by NHE1 dominate protons of the bulk solution. *J Physiol* **585**, 351-360, doi:10.1113/jphysiol.2007.145185 (2007).

210 Böhme, I. & Bosserhoff, A. K. Acidic tumor microenvironment in human melanoma. *Pigment Cell Melanoma Res* **29**, 508-523, doi:10.1111/pcmr.12495 (2016).

211 Goldberg, S. B. *et al.* Pembrolizumab for patients with melanoma or non-small-cell lung cancer and untreated brain metastases: early analysis of a non-randomised, open-label, phase 2 trial. *Lancet Oncol* **17**, 976-983, doi:10.1016/S1470-2045(16)30053-5 (2016).

212 Kluger, H. M. *et al.* Long-Term Survival of Patients With Melanoma With Active Brain Metastases Treated With Pembrolizumab on a Phase II Trial. *J Clin Oncol* **37**, 52-60, doi:10.1200/JCO.18.00204 (2019).

213 Liapi, E. *et al.* Assessment of tumoricidal efficacy and response to treatment with 18F-FDG PET/CT after intraarterial infusion with the antiglycolytic agent 3-bromopyruvate in the VX2 model of liver tumor. *Journal of nuclear medicine : official*

publication, Society of Nuclear Medicine **52**, 225-230, doi:10.2967/jnumed.110.083162 (2011).

214 Duran, R. *et al.* Preclinical Benefit of Hypoxia-Activated Intra-arterial Therapy with Evofosfamide in Liver Cancer. *Clinical cancer research : an official journal of the American Association for Cancer Research* **23**, 536-548, doi:10.1158/1078-0432.ccr-16-0725 (2017).

215 Vali, M. *et al.* Targeting of VX2 rabbit liver tumor by selective delivery of 3-bromopyruvate: a biodistribution and survival study. *The Journal of pharmacology and experimental therapeutics* **327**, 32-37, doi:10.1124/jpet.108.141093 (2008).

216 Buijs, M. *et al.* Quantitative proton MR spectroscopy as a biomarker of tumor necrosis in the rabbit VX2 liver tumor. *Journal of vascular and interventional radiology : JVIR* **22**, 1175-1180, doi:10.1016/j.jvir.2011.03.016 (2011).

217 Ko, Y. H., Pedersen, P. L. & Geschwind, J. F. Glucose catabolism in the rabbit VX2 tumor model for liver cancer: characterization and targeting hexokinase. *Cancer letters* **173**, 83-91 (2001).

218 Park, H. S. *et al.* FDG-PET for evaluating the antitumor effect of intraarterial 3-bromopyruvate administration in a rabbit VX2 liver tumor model. *Korean journal of radiology* **8**, 216-224, doi:10.3348/kjr.2007.8.3.216 (2007).

219 Chen, J. H. *et al.* Induction of VX2 carcinoma in rabbit liver: comparison of two inoculation methods. *Laboratory animals* **38**, 79-84, doi:10.1258/00236770460734434 (2004).

220 Lee, K. H. *et al.* Distribution of iron oxide-containing Embosphere particles after transcatheter arterial embolization in an animal model of liver cancer: evaluation

with MR imaging and implication for therapy. *Journal of vascular and interventional radiology : JVIR* **19**, 1490-1496, doi:10.1016/j.jvir.2008.06.008 (2008).

221 Yamamoto, A. *et al.* Evaluation of tris-acryl gelatin microsphere embolization with monochromatic X Rays: comparison with polyvinyl alcohol particles. *Journal of vascular and interventional radiology : JVIR* **17**, 1797-1802, doi:10.1097/01.RVI.0000243614.87529.b0 (2006).

222 Hong, K., Kobeiter, H., Georgiades, C. S., Torbenson, M. S. & Geschwind, J. F. Effects of the type of embolization particles on carboplatin concentration in liver tumors after transcatheter arterial chemoembolization in a rabbit model of liver cancer. *Journal of vascular and interventional radiology : JVIR* **16**, 1711-1717, doi:10.1097/01.rvi.0000184535.26360.5a (2005).

223 Buck, M. D., Sowell, R. T., Kaech, S. M. & Pearce, E. L. Metabolic Instruction of Immunity. *Cell* **169**, 570-586, doi:10.1016/j.cell.2017.04.004 (2017).

224 Goetze, K., Walenta, S., Ksiazkiewicz, M., Kunz-Schughart, L. A. & Mueller-Klieser, W. Lactate enhances motility of tumor cells and inhibits monocyte migration and cytokine release. *International journal of oncology* **39**, 453-463, doi:10.3892/ijo.2011.1055 (2011).

225 Rong, Y., Durden, D. L., Van Meir, E. G. & Brat, D. J. 'Pseudopalisading' necrosis in glioblastoma: a familiar morphologic feature that links vascular pathology, hypoxia, and angiogenesis. *J Neuropathol Exp Neurol* **65**, 529-539, doi:10.1097/00005072-200606000-00001 (2006).

226 Ahn, S. H. *et al.* Necrotic cells influence migration and invasion of glioblastoma via NF-κB/AP-1-mediated IL-8 regulation. *Sci Rep* **6**, 24552, doi:10.1038/srep24552 (2016).

227 Wu, C. X. *et al.* Peritumoral edema shown by MRI predicts poor clinical outcome in glioblastoma. *World J Surg Oncol* **13**, 97, doi:10.1186/s12957-015-0496-7 (2015).

228 Lim, M., Xia, Y., Bettegowda, C. & Weller, M. Current state of immunotherapy for glioblastoma. *Nat Rev Clin Oncol* **15**, 422-442, doi:10.1038/s41571-018-0003-5 (2018).

229 Herting, C. J. *et al.* Tumour-associated macrophage-derived interleukin-1 mediates glioblastoma-associated cerebral oedema. *Brain* **142**, 3834-3851, doi:10.1093/brain/awz331 (2019).

230 Vallatos, A. *et al.* Quantitative histopathologic assessment of perfusion MRI as a marker of glioblastoma cell infiltration in and beyond the peritumoral edema region. *J Magn Reson Imaging* **50**, 529-540, doi:10.1002/jmri.26580 (2019).

231 Henker, C. *et al.* Volumetric assessment of glioblastoma and its predictive value for survival. *Acta Neurochir (Wien)* **161**, 1723-1732, doi:10.1007/s00701-019-03966-6 (2019).

232 Grossman, R. *et al.* Dynamics of FLAIR Volume Changes in Glioblastoma and Prediction of Survival. *Ann Surg Oncol* **24**, 794-800, doi:10.1245/s10434-016-5635-z (2017).

ProQuest LLC
789 East Eisenhower Parkway
P.O. Box 1346
Ann Arbor, MI 48106 - 1346 USA